# Experimental Analysis of a Turbulent Liquid Metal Flow in a Heated Vertical Confined Backward Facing Step

Zur Erlangung des akademischen Grades eines
**DOKTORS DER INGENIEURWISSENSCHAFTEN (Dr.-Ing.)**

von der KIT-Fakultät für Maschinenbau des
Karlsruher Instituts für Technologie (KIT)
angenommene

**DISSERTATION**

von

Dipl.-Ing. Thomas Andreas Schaub Hahn

Tag der mündlichen Prüfung: 26.09.2022

Hauptreferent: Prof. Dr.-Ing. Robert Stieglitz
Korreferent: Prof. i.R. Dr.-Ing. Cameron Tropea

# Foreword

Three comments.

First, this dissertation is not only intended to put into paper my work done in the past years, but also serve as a starting point to future doctoral students and/or researchers carrying on with this research topic. I personally had a hard time finding books or articles that would take you from a neophyte level into becoming someone that - at least - somehow understands the open questions in the field. And this, by digging deep into the physics showing how things *really* are (i.e. without making confusing simplifications), and in parallel, taking into consideration how these ideas can be expressed mathematically. The gap between undergraduate fluid mechanics textbooks and specialized turbulence monographs is not negligible. This document *does not* pretend to fill any gap regarding this issue (I am very far from being qualified for this), but at least, to reference to the literature where a specific questions is answered or an explanation is given.

Second, a few weeks after publishing Schaub *et al.* (2022), I noticed an unfortunate notation mistake regarding turbulent heat fluxes $\langle u_i' T' \rangle$. I somehow forgot to include the ensemble averaging $\langle \cdot \rangle$ angled brackets around $u_i' T'$ in the final paper version. Sorry for that.

Third, in international textbooks, it is common to denote the heat transfer coefficient with $h$ and the molecular thermal diffusivity with $\alpha$. In German literature, however, they tend to use $\alpha$ for the heat transfer coefficient and to use $a$ for the molecular thermal diffusivity. I would have preferred to follow the international notation, but I also wanted to be consequent to the previous literature on *backward facing step* research, which uses $h$ for the step height. Hence, I decided to take the German nomenclature for the heat transfer coefficient $\alpha$ and the molecular diffusivity $a$ and used $h$ for the backward facing step step height.

# Acknowledgments

First, I thank Prof. Dr.-Ing. Robert Stieglitz for giving me the chance to pursue this doctoral thesis, for his meticulous proof-readings and - of course - for his tips and for sharing his know-how and experience with me during the project. I thank Prof. i.R. Dr.-Ing. Cameron Tropea to be willing to help and contribute to the project from its beginning, as well as for his very helpful proof-reading. I also thank Prof. Dr. mont. Christoph Kirchlechner, the exam chairman.

I thank Dr.-Ing. Wolfgang Hering for taking a shot on me and picking me out from who knows how many applicants for this job. He continuously supported the project and has always been open to discuss new, wild and even exotic ideas.

At this point I want to thank the technical team at KIT for their support, commitment, initiative and patience without whom this project would literally not have been possible: Joachim Konrad, Kevin Krauth, Daniel Kuntz and Paul Wagner-Nagy from the central workshop at KIT; Oliver Albrecht and Rupert Schmidt from the workshop at INR and Hans-Jörg Brinkmann from the MEKKA-Team.

I thank Sascha Wüstling and Michael Tasler for their invaluable time, patience, help and guidance in the measurement chain development.

I want to thank the research staff at INR and ITES for their patience to answer all my questions on whatever topic: Dr.-Ing. Frederik Arbeiter, Georg Schlindwein, Dr.-Ing. Sebastian Ruck, Dr.-Ing. Günther Grötzbach, Prof. Dr.-Ing. Leo Bühler, Dr.-Ing. Cyril Courtessole, Markus Daubner, Frank Fellmoser and Dr.-Ing. Julio Pacio (now at SCK-CEN).

I want to thank the students and apprentices I had the pleasure to assist during their theses and/or mid-term projects and/or final project work: Christine Steiner, Lukas Lödige, Philipp Janzer, Fabian Beck, Joshua Kohpeiß, Veronika Gretz and Svenja Meyer. The tutoring would not have been possible either without the help of Martin Lux and Prof. Dr.-Ing. Thomas Wetzel.

I thank my day-to-day colleagues for helping me to get past the daily routine in a better way: Birgit Zagolla, Petra Klug, Ingeborg Schartz, Dr.-Ing. Sara Pérez

Martín, Dr.-Ing. Verónica Jauregui Chávez, Dr.-Ing. Nerea Rocío Diez de los Ríos Ramos, Dr.-Ing. Regina Krüssmann, Dr.-Ing. Manuel García, Dr.-Ing. Diego Ferraro, Javier Etcheto, Dr. Juan Blanco, Dr.-Ing. José Ángel González Vargas, Dr.-Ing. Ignacio Gómez-García-Toraño, Dr.-Ing. Yousef Alzaben, Abdullah Abalkhail, Jorge Yáñez Escaciano, Dr.-Ing. Uwe Imke, Dr.-Ing. Víctor Hugo Sánchez Espinoza, Werner Pfrang.

I want to thank my parents, my Chilean and German family for their patience and support.

And last, but definitely not least, I must - of course - thank *her*. Danke, Andrea!

# Abstract

Experiments and complementary numerical calculations have been conducted for a non-isothermal vertical confined backward facing step with low Prandtl number fluid, namely, the eutectic alloy gallium-indium-tin. The experimental facility and so-called permanent magnet probes for the local measurement of temperature and velocity of the liquid metal flow have been developed, designed and manufactured from the ground up. The probes have been adapted and optimized to meet the technical requirements for the present case regarding their design, the calibration procedure and the temperature correction method. The experiments have been run for different Reynolds and Richardson numbers covering both forced and mixed convection regimes. Time-averaged velocity profiles of the flow have been measured at six streamwise positions along the centerline of the test section. The local Nusselt number along the backward facing step heated plate has been measured in both streamwise and spanwise directions as well.

The calibration results of the permanent magnet probes show good agreement with theoretical predictions regarding their linearity and sensitivity. The measured velocity profiles show the expected behavior for the forced and mixed convection regimes. The onset to mixed convection is not observed in the measured local Nusselt number distribution along the heated plate. This is explained by the way the Nusselt number is defined for the present case, as shown by the results of the performed numerical simulations. The local Nusselt number along the heated plate spanwise direction shows an asymmetry hardly distinguishable from experimental uncertainty due to the influence of the used thermocouples. An order of magnitude analysis is performed to estimate the onset for the transition of forced to mixed convection and shows good agreement with the experimental data. The numerical simulations also show non-intuitive heat flux paths within the heated plate besides of the important influence of secondary flow of the second kind on the heat transfer characteristics.

The measured velocity and Nusselt number profile data can be used for further

validation of low Prandtl fluid heat flux models. The experience and knowhow gained during the development and operation of permanent magnet probes can be transferred to other liquid metal technical applications and experiments. With minor optimizations to the current experimental setup, the local measurement local mean temperatures, fluctuating velocity and temperature quantities is possible, as well as time-dependent spectral analyses.

# Kurzfassung

Ein “backward facing step”-Experiment und ergänzende numerische Berechnungen wurde für eine nicht-isotherme, vertikale, von Seitenwänden beeinflusste bzw. begrenzte Strömung mit einem Fluid niedriger Prandtl-Zahl durchgeführt, nämlich die eutektische Legierung Gallium-Indium-Zinn. Die Versuchsanlage und die für die lokale Messung von Temperatur und Geschwindigkeit der Flüssigmetallströmung nötigen Permanentmagnetsonden wurden von Grund auf entwickelt, konstruiert und gefertigt. Die Sonden wurden hinsichtlich ihres Aufbaus, des Kalibrierverfahrens und der Temperaturkorrekturmethode an die technischen Anforderungen des vorliegenden Falles angepasst und optimiert. Die Experimente wurden für verschiedene Reynolds- und Richardson-Zahlen durchgeführt. Diese decken sowohl erzwungene als auch Mischkonvektion ab. Die zeitlich gemittelten Geschwindigkeitsprofile der Strömung wurden an sechs Positionen in Strömungsrichtung entlang der Mittellinie des Versuchsstands anhand Permanentmagnetsonden gemessen. Die lokale Nusselt-Zahl entlang der Heizplatte wurde sowohl in Hauptströmungs- wie auch in Querrichtung zur Hauptströmung gemessen.

Die Kalibrierungsergebnisse der Permanentmagnetsonden zeigen eine gute Übereinstimmung mit den theoretischen Vorhersagen hinsichtlich der Linearität und Empfindlichkeit des Nutzsignals. Die gemessenen Geschwindigkeitsprofile zeigen das erwartete Verhalten sowohl für den Fall bei erzwungener Konvektion, wie auch bei Mischkonvektion. Andererseits wird der Umschlag der Mischkonvektion in der gemessenen lokalen Nusselt-Zahl-Verteilung entlang der Heizplatte nicht beobachtet. Dies ist auf die Art und Weise zurückzuführen, wie die Nusselt-Zahl definiert worden ist. Die lokale Nusselt-Zahl entlang der Heizplatte in Querrichtung zeigt eine leichte Asymmetrie, wobei diese aufgrund des Einflusses der verwendeten Thermoelemente kaum von der experimentellen Unsicherheit zu unterscheiden ist. Eine Größenordnungsanalyse für die Bestimmung des Umschlag von erzwungener zu Mischkonvektion wird hergeleitet. Die Ergebnisse zeigen eine gute Übereinstimmung mit den experimentellen Daten. Die numerischen Simulationen zeigen nicht

intuitive Wärmestrompfade innerhalb der beheizten Platte neben dem wichtigen Einfluss von Sekundärströmung zweiter Art auf die Wärmeübertragungseigenschaften.

Die Messdaten zu den gemessenen Geschwindigkeits- und Nusseltzahlprofilen können zur weiteren Validierung und Entwicklung von Wärmestrommodellen für Fluide niedriger Prandtl-Zahl verwendet werden. Die gesammelten Erfahrungen und das erarbeite Know-How, welches bei der Entwicklung und während des Betriebs der Permanentmagnetsonden gewonnen worden sind, kann auf weitere flüssigmetalltechnische Anwendungen und Experimente übertragen werden. Anhand Optimierungen am aktuellen Versuchsaufbau, welche jedoch keinen größeren Zeitaufwand bzw. Geldinvestitionen bedürfen, ist die lokale Messung von Mitteltemperaturen, schwankender Geschwindigkeits- und Temperaturgrößen sowie zeitabhängiger Spektralanalysen möglich.

# Publications related to this thesis

**Peer reviewed journals**

- Schaub T., Arbeiter F., Hering W. & Stieglitz R. (2022). *Forced and mixed convection experiments in a confined vertical backward facing step at low-Prandtl number*. Experiments in Fluids 63(19). https://doi.org/10.1007/s00348-021-03363-9

- Schaub T., Wüstling S., Konrad J. & Tasler M. (2021). *Design and calibration of permanent magnet probes for the local measurement of velocity and temperature in a liquid metal backward facing step flow*. Experiments in Fluids 62(210). https://doi.org/10.1007/s00348-021-03293-6

- Hering W., Fuchs J., Onea A., Perez-Martin S., Schaub T. (2021). Experiment and Codes to Support Safety Assessments for Sodium Fast Reactors (KASOLA, SOLTEC and KARIFA). ASME Journal of Nuclear Engineering and Radiation Science NERS-21-1031. https://doi.org/10.1115/1.4052642

- Oder J., Tiselj I., Jäger W., Schaub T., Hering W., Otic I. & Shams A (2020). *Thermal fluctuations in low Prandtl number fluid flows over a backward facing step*. Nuclear Engineering and Design, 359, 110460. https://doi.org/10.1016/j.nucengdes.2019.110460

- Shams A., Roelofs F., Tiselj I., Oder J., Bartosiewicz Y., Duponcheel M., Niceno B., Guo W., Stalio E., Angeli D., Fregni A., Buckingham S., Koloszar L.K.,Villa Ortiz A., Planquart P., Narayanan C., Lakehal D., van Tichelen K, Jäger W. & Schaub T. (2020). *A collaborative effort towards the accurate prediction of turbulent flow and heat transfer in low Prandtl number fluids*. Nuclear Engineering and Design, 366, 110750. https://doi.org/10.1016/j.nucengdes.2020.110750

**Conference contributions**

- Onea A., Hering W., Fuchs J., Schaub T., Weisenburger A., Stieglitz R. (2022). *Facilities to investigate sodium and materials behavior up sodium boiling*. International Meeting on Nuclear Reactor Thermal Hydraulics (NURETH-19), 3-11 March 2022, Brussels, Belgium.

- González F., Barraza R., Schaub T., Estay D., Guzmán L. (2020). *Analysis of thermal stresses in square ducts of solar receivers operated with liquid sodium*. Proceedings of the ISES Solar World Congress 2019 and IEA SHC International Conference on Solar heated and Cooling for Buildings and Industry 2019.

- Schaub T., Krauth K., Konrad J. (2019). *Design process of a vertical backward facing step experiment for forced and mixedconvection for low Prandtl number flows*. 17th European Turbulence Conference, 3-6 September 2019, Torino, Italy.

- Jäger W., Schaub T., Hering W., Otic I., Shams A., Oder J., Tiselj I. (2017). *Design and Pre-Evaluation of a Backward Facing Step Experiment with Liquid Metal Coolant*. International Meeting on Nuclear Reactor Thermal Hydraulics (NURETH-17), Sept. 3–8, 2017, Xi'an, China.

# Nomenclature

### Abbreviations

| | |
|---|---|
| AR | Aspect Ratio |
| BFS | Backward Facing Step |
| CFD | Computational Fluid Dynamics |
| CFM | Coriolis Flow Meter |
| DNS | Direct Numerical Simulation |
| ER | Expansion Ratio |
| GUM | Guide to the Expression of Uncertainty in Measurement |
| IFM | Inductive Flow Meter |
| JCGM | Joint Committee for Guides in Metrology |
| LES | Large Eddy Simulation |
| MHD | Magnetohydrodynamics |
| PEEK | Polyether Ether Ketone |
| PEEK | Polyetheretherketone |
| PMP | Permanent Magnet Probe |
| RANS | Reynolds Averaged Navier-Stokes |
| SS | Stainless Steel |
| TFM | Turbine Flow Meter |

# Contents

# 1

# Introduction

## 1.1 Motivation for a low Prandtl number vertical backward facing step experiment (BFS)

Liquid metals are attractive working fluid candidates for high temperature thermal-hydraulics and thermo-chemical applications, such as concentrated solar power plants, nuclear and fusion reactors (and related technologies), direct thermo-electrical converters, hydrogen production, among others. A review on the applications of liquid metals in science and technology is given by Heinzel *et al.* (2017).

The use of liquid metals in flow systems imposes numerous technical, experimental and theoretical challenges, which motivate both basic and applied multidisciplinary research. Specifically, in the field of thermal-hydraulics, efforts have been invested into the development of numeric calculation tools. These aim to reduce the need for prototype development and experiments to a minimum. The development and engineering time and costs of the aforementioned power plants can be then optimized making them more attractive to investors.

The calculation and prediction of thermal-hydraulic behavior of flows with computers is referred to as computational fluid dynamics (CFD). The fundamental analytical partial differential equations of thermal-hydraulics are discretized using numerical schemes, then rewritten into a large system of algebraic equations and finally solved by means of numerical algorithms. Since for practical engineering applications an exact numerical solution of the governing equations of thermal-hydraulics is not realizable, physical models that simplify, yet accurately predict the underlying physics, are needed.

One of the most important physical phenomena that requires very careful model-

ing is the flow turbulence and its associated heat transfer mechanism, i.e. convective heat transfer. This holds for every kind of fluid, although the convective heat transfer calculations for common fluids like air and water can be considerably simplified by assuming the so-called REYNOLDS analogy (see section B.3). It draws a scale and time similarity between the viscous and thermal boundary layers, as illustrated in Fig.1.1. This assumption is not valid for liquid metal flows, due to their very high thermal conductivity. In simpler terms, this refers to the notion that heat from a heated wall is carried away from the wall by fluid eddies alone, i.e. thermal conduction is neglected all over the fluid, except for at a very thin layer immediately adjacent to the heated wall. In Fig. 1.1, the upper contour plot shows the velocity contours of a turbulent flow (from left to right) between two parallel flat plates of infinite dimension, whereby both plates are heated. The velocity magnitude is depicted in color, where dark red refers to high velocity and dark blue refers to low velocity. The two lower contour plots show the respective temperature contours - on the left for a regular fluid like air or water, and on the right for a liquid metal, where dark red refers to a high temperature and dark blue to a low temperature. When comparing the velocity and temperature contour plots for water and air, one can observe that the velocity and temperature fields present a *similar* general structure, i.e. it may be intuitive to extrapolate information from the velocity field to calculate the temperature field, without the need of any further major assumptions. This relationship between both fields works and holds true under certain heat transfer circumstances for common fluids, since heat is transported away from the wall towards the flow core only by the motion of turbulent eddies. For the liquid metal case however, the relationship or the *similarity* between both fields is not observed. Temperature contours in this case are much smoother and no fine structures can be observed, as for the regular fluid case. Additionally, the high temperature penetrates deeps into the flow core, indicating the important role played by the fluid high thermal conductivity. It is then no longer obvious how to extrapolate information from the velocity field to calculate the temperature field. Thus, the theory behind convective heat transfer models for liquid metal needs to be adapted to account for the observed effect of *scale separation* between the velocity and temperature fields.

To test the hypothesis behind convective heat transfer and turbulence models, so called *benchmark experiment*s are needed. They provide reference experimental data under laboratory conditions, that is, under controlled and reproducible conditions. Modeling hypotheses can then be tested and compared with this experimental data.

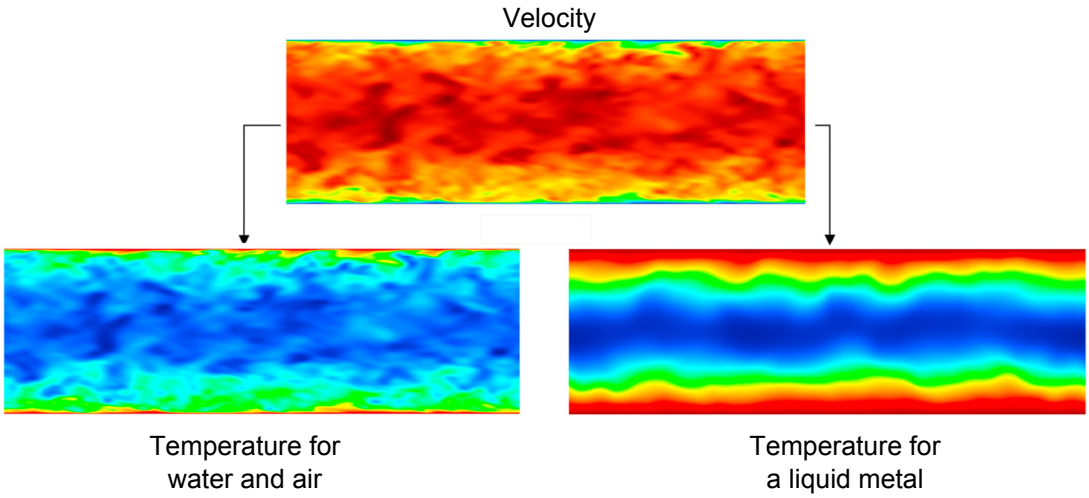


Figure 1.1: Snapshot of velocity and temperature fields of a Direct Numerical Simulation (DNS) of a flow between two parallel, infinite and heated plates for regular fluids (left) and a typical liquid metal (right). For a same velocity field two very different temperature fields are observed depending on the fluid thermal diffusivity (water and air versus a liquid metal). Figure adapted from Roelofs *et al.* (2015)

An example of a benchmark experiment is the backward facing step (BFS). Its geometry is shown in Fig. 1.2. The flow enters the BFS geometry through the *inlet* and flows towards the sudden duct cross-section expansion, forming a "dead water" or recirculation region after the *step*. When installing the BFS geometry in a vertical orientation, i.e. the fluid flowing upwards (as shown in Fig. 1.2), buoyancy driven flows can be induced if a wall segment is heated (in this case, the wall behind the step). Furthermore, if a square duct is used, secondary motions of the second kind (as defined by Prandtl *et al.* (1969)) are induced, i.e. even more flow physics phenomena is included.

A BFS-experiment, depending on the chosen geometry and working fluid, offers a wide variety of several thermal-hydraulic physical phenomena. As a consequence, the realization of a vertical backward facing step experiment, having a liquid metal as a working fluid, poses an interesting and challenging benchmark experiment case for the validation of turbulence and convective heat transfer models. Once these models are validated for such thermal-hydraulic conditions, one may say that these models will predict with reasonable accuracy flow phenomena found in industrial applications, for instance, heat exchangers.

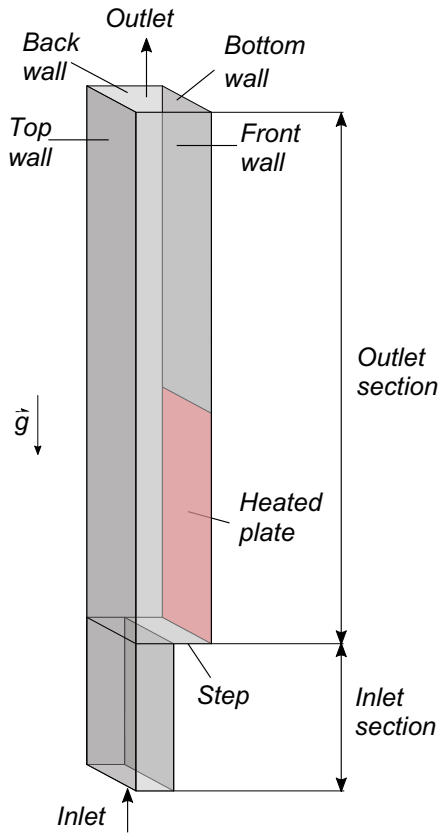


Figure 1.2: Sketch of a heated backward facing step (BFS) geometry

## 1.2 Objectives and structure of this dissertation

The objectives of this thesis are:

i. To conduct the *first* non-isothermal BFS experiment with a liquid metal in the open literature. This, under user-friendly conditions as a first step to a similar but much more complex experiment in a large sodium facility.

ii. To develop the required instrumentation, its measurement chain and calibration methodology to measure locally and simultaneously velocity and temperature profiles in the BFS flow.

iii. To provide experimental data to contribute to the further development and validation of convective turbulent heat transfer models for liquid metal flows.

iv. To identify the transition onset from forced to mixed convection in terms of an order of magnitude analysis.

This dissertation is structured as follows:

i. Chapter 2 describes the theoretical aspects of liquid metal thermal-hydraulics, the general BFS flow phenomena, important geometrical definitions and a literature review of the available numerical work done in the past years on liquid metal BFS flows.

ii. Chapter 3 introduces the designed facility, its BFS test section, the in-house developed instrumentation and the required calibration strategy for the local measurement of time averaged velocity in a liquid metal flow.

iii. Chapter 4 shows the experiment and numerical simulations results. Measured time averaged velocity profiles and local Nusselt number $Nu$ distributions are presented, analyzed and interpreted and related to the obtained numerical simulations results.

iv. Chapter 5 summarizes the most important conclusions.

v. Chapter 6 proposes further work to be done to extend and deepen the analysis presented in this study.

This manuscript is a self-contained version of two published papers related to this project Schaub *et al.* (2021) and Schaub *et al.* (2022), which extend and deepen some technical aspects and the analysis presented here. New numerical simulations postprocessing results are presented here compared to those shown in the mentioned publications.

# 2

# Theory on liquid metal thermal hydraulics

This chapter introduces the theoretical aspects of the study of thermal hydraulics with a focus on single-phase convective turbulent liquid metal flows applied to the confined BFS experiment and its constraints. The general backward facing step (BFS) flow features and geometrical definitions and how these account for the flow characteristics are introduced as well. Finally, a literature review on the available literature on liquid metal flows is presented.

## 2.1 Convective heat transfer of liquid metal flows

### 2.1.1 General governing equations: conservation laws

The mathematical treatment of fluid mechanics and heat transfer is built upon the continuum hypothesis, which assumes that matter can be treated as a infinitely dividable continuum media and not as a collection of discrete molecules or atoms interacting with each other. The continuum theory allows us to treat matter mathematically in terms of continuous fields, which may be scalar fields (e.g. temperature, density), vector fields (e.g. velocity, temperature gradients) or tensor fields (e.g. stresses, velocity gradients). The cornerstones of the mathematical treatment of continuum mechanics are the conservation laws (mass, momentum, energy, etc.) and some constitutive equations in order to define relationships between the state of matter and continuous fields.

In this study, SI units and a Cartesian coordinate system are used, where the

$+x$ direction is defined as the streamwise direction. Equations are written using index notation making use of Einstein´s summation convention. The difference and relationship between Eulerian and Lagrangian description of fluid motion is assumed as known, for a review, see Lumley (1969).

### Conservation of mass for a fluid particle

**General continuity equation** First, a fluid particle with volume $\delta\forall$ needs to be defined. As defined by Kundu *et al.* (2016): "A fluid particle is a small deforming volume carried by the flow that: 1.) always contains the same fluid molecules, 2.) is large enough so that its thermodynamic properties are well defined when it is at equilibrium, but 3.) small enough so that its relaxation time is short compared to the time scales of fluid-motion-induced thermodynamic changes". The conservation of mass states that, in the absence of mass sources or sinks, the rate of change of density of a fluid particle is proportional to spatial volume changes of it. Mathematically this is expressed as

$$\frac{D\rho}{Dt} + \rho \frac{\partial u_i}{dx_i} = 0, \tag{2.1}$$

where $\rho$ is the fluid particle density and may vary with time and position, $t$ time, $x_i$ the $i$-th component of the position vector $x_i = [x,y,z]^T$, $u_i$ the $i$-th component of the velocity vector $[u,v,w]^T$ and $\frac{\partial(...)}{\partial t} + u_j \frac{\partial(...)}{dx_j} \equiv \frac{D(...)}{Dt}$. This equation is also called *continuity equation*. It may be recalled that $\frac{D\rho}{Dt} + \rho \frac{\partial u_i}{dx_i} \iff \frac{\partial \rho}{\partial t} + \frac{\partial(\rho u_i)}{\partial x_i}$ without the need of any assumption.

**Continuity equation for incompressible flows** A liquid metal flows can be considered as incompressible[1], so that Eq. (2.1) is rewritten as

$$\frac{\partial u_i}{dx_i} \approx 0. \tag{2.2}$$

The procedure to deduce this equation and some other important aspects on how these mathematical equations express physical phenomena can be found in Batchelor (1967) and George (2009).

[1] To be distinguished from incompressible fluids!

**Conservation of linear momentum for a fluid particle**

**Newton´s second law for a fluid particle** Newton´s second law of dynamics applied to a fluid particle, also called Cauchy´s equation of motion, reads in Lagrangian form as:

$$\rho \frac{Du_i}{Dt} = \rho f_i + P_i, \tag{2.3}$$

where the term to the left represents the fluid particle acceleration due to sum of $f_i$, the $i$-th component of the body forces per unit mass and $P_i$, the $i$-th component of the surface forces per unit volume. The fact that the density is outside of the material derivative of Eq. (2.3) is a consequence of the REYNOLDS *Transport Theorem* and not due to a restriction on the flow (incompressible flow) nor the density (incompressible fluid) (George (2009)), i.e. that $\rho \frac{Du_i}{Dt} \iff \frac{\partial(\rho u_i)}{\partial t} + \frac{\partial\left(\rho u_i u_j\right)}{\partial x_j}$ without the need for any further assumptions.

**Navier-Stokes equations** Relating the surface forces term of Eq. (2.3) to field variables by means of *constitutive relations* and assuming an incompressible flow, one obtains the Navier-Stokes equations for incompressible flows, which read

$$\rho \frac{Du_i}{Dt} = \rho f_i - \frac{\partial p_{mech}}{\partial x_i} + \frac{\partial}{\partial x_j} \mu \left( \frac{\partial u_i}{\partial x_j} + \frac{\partial u_j}{\partial x_i} \right), \tag{2.4}$$

where $p_{mech} \equiv \frac{1}{3}\sigma_{ii}$ is the *mechanical pressure*, defined as the trace of the isotropic component of the stress tensor $\sigma_{ji} = -p_{mech}\delta_{ji} + \tau_{ji}$, with $\tau_{ji} = 2\mu \left(S_{ji} - \frac{1}{3}S_{kk}\delta_{ji}\right)$; $S_{ji} \equiv \frac{1}{2}\left(\frac{\partial u_j}{\partial x_i} + \frac{\partial u_i}{\partial x_j}\right)$ and $\mu$ the fluid dynamic viscosity. The anti-symmetric part of $\frac{\partial u_j}{\partial x_i}$ is not taken into account for the stress specification since it only contributes to the fluid particle rotation and not to the deformation (Kundu *et al.* (2016) and Landau & Lifshitz (1987)). As it is known from continuum mechanics, a surface force contributes to the acceleration of a fluid particle only if the stress tensor $\sigma_{ji}$ varies with position in the fluid, hence only when $P_i = \frac{\partial \sigma_{ij}}{\partial x_j} \neq 0$, i.e. when there is a deformation to the fluid particle, see Batchelor (1967).

**The non-Oberbeck-Boussinesq approximation** The only body force $\rho f_i$ considered in this analysis is that due to the effects of buoyancy and is calculated by means of a *simplified* version of the non-OBERBECK-BOUSSINESQ approximation.

In general terms, the OBERBECK-BOUSSINESQ approximation[2] expresses gravity forces only due to buoyancy effects in terms of relative density differences $\Delta\rho$ within the flow. A further characteristic of its classical formulation is that all physical properties of the flow are considered constant, except the density. On the other hand, the non-Oberbeck-Boussinesq appoximation deals with the case when fluid physical properties *cannot* be regarded as constants in time and space. Furthermore, in its *simplified* version, some physical properties are regarded as constant, while others cannot.

Which form of the Oberbeck-Boussinesq is taken must be assessed for each individual case with the systematic approach proposed by Gray & Giorgini (1976). Here, the *simplified* non-Oberbeck-Boussinesq approximation is used, considering only the dynamic viscosity $\mu$ as a temperature (and hence spatial) dependent variable, for more details see appendix A.

To account for the effects of buoyancy induced by gravitational acceleration, $f_i$ is set to $f_i = g_i$, where $g_i$ is the gravitational acceleration. Substituting the *simplified* non-Oberbeck-Boussinesq approximation into the Navier-Stokes equations one obtains

$$\rho_{ref}\frac{Du_i}{Dt} \approx \Delta\rho\, g_i - \frac{\partial p_{mod}}{\partial x_i} + \frac{\partial}{\partial x_j}\mu\left(\frac{\partial u_i}{\partial x_j} + \frac{\partial u_j}{\partial x_i}\right), \tag{2.5}$$

where $\Delta\rho = \rho - \rho_{ref}$ is the density difference between the local value of $\rho$ and the reference density $\rho_{ref}$, which may be variable in space. The pressure term also is modified by introducing the *modified pressure* $p_{mod} \equiv p_{mech} - p_{static}$ which accounts only for the dynamic component of pressure, i.e. not considering its static component.

Eqs. (2.5) and (2.2) sum up a total of four equations for a total of five unknowns. This means that the system is not closed. In order to close the system, one usually takes either the equation of state for gases or the equation of conservation of energy for liquids. Since here we are dealing with a liquid, the next step is to relate the density variations $\Delta\rho$ to the equation for conservation of energy. If density variations in the field are relatively small, $\Delta\rho$ can be approximated by truncating its Taylor expansion to the linear term around the reference point as:

[2]This approximation is sometimes also called the Boussinesq approximation in the literature. For historical reasons, the specialized literature tends to include the name of the original author of the approximation (OBERBECK).

$$\Delta\rho \approx \rho_{ref}\left[-\frac{1}{\rho_{ref}}\frac{\partial\rho}{\partial T}\bigg|_{ref}\right]\Delta T \equiv -\rho_{ref}\beta_{ref}\Delta T_{ref}, \tag{2.6}$$

where $\beta_{ref}$ is the isobaric coefficient of volume expansion evaluated at the reference temperature $T_{ref}$ and $\Delta T_{ref} = T - T_{ref}$ the temperature difference between the local temperature and a reference temperature. The effect of the variation of $\Delta\rho$ due to the change of static pressure can be shown to be orders of magnitude smaller than the one due to temperature difference $\Delta T_{ref}$, hence it can be neglected, see George (2009). Inserting Eq. (2.6) into Eq. (2.5) one obtains

$$\rho_{ref}\frac{Du_i}{Dt} \approx -\left(\rho_{ref}\beta_{ref}\Delta T_{ref}\right)g_i - \frac{\partial p_{mod}}{\partial x_i} + \frac{\partial}{\partial x_j}\mu\left(\frac{\partial u_i}{\partial x_j} + \frac{\partial u_j}{\partial x_i}\right), \tag{2.7}$$

where $\Delta T_{ref}$ still has to be determined.

An equation for the description of the temperature field is then needed, which is obtained from a simplified form of the equation for conservation of energy.

### Conservation of energy

**First law of thermodynamics for a fluid particle** The first law of thermodynamics reads in its general form for a fluid particle as (Schlichting & Gersten (2017), p.69):

$$\frac{DE_{total}}{Dt} = \dot{Q} + \dot{W} = \dot{Q} + \dot{W}_{body} + \dot{W}_{surface}, \tag{2.8}$$

where $E_{total}$ is the total energy of the fluid particle; $\dot{Q}$ is a source term representing the heat crossing the system boundaries per unit time (i.e. the heat flux) due to one or more heat sources; $\dot{W}$ is a source term representing the sum of the work done per unit time by body forces $\dot{W}_{body}$ and the power exerted by surface forces $\dot{W}_{surface}$ at the system boundaries of the fluid particle.

**The equation of heat** In order to calculate $T$ from Eq. (2.8) for a fluid particle, all the terms need to be related to the local temperature field. This can be achieved using basic thermodynamic relationships and ad hoc simplifications and assumptions. By doing so, one obtains the general form for the equation of heat (Schlichting & Gersten (2017)) which reads,

$$\rho c_p \frac{DT}{Dt} = \frac{\partial}{\partial x_i} \lambda \frac{\partial T}{\partial x_i} + \beta T \frac{Dp_{mech}}{Dt} + \mu \Phi, \tag{2.9}$$

where $c_p$ is the specific heat capacity of the liquid; $\lambda$ the thermal conductivity of the liquid; $\dot{Q} = \frac{\partial}{\partial x_i} k \frac{\partial T}{\partial x_i}$ (FOURIER empirical law for thermal conduction); $\dot{W}_{body} = \beta T \frac{Dp_{mech}}{Dt}$ (*pressure work* term) and $\dot{W}_{surface} = \mu \Phi$ (*viscous dissipation* term), where the dissipation function $\Phi$ is defined as $\Phi \equiv \tau_{ji} \frac{1}{2} \left( \frac{\partial u_j}{\partial x_i} + \frac{\partial u_i}{\partial x_j} \right) = \tau_{ji} S_{ji}$.

Since $\Delta T$ is needed to solve Eq. (2.7), it may become handy or *Boussinesq friendlier* to express the temperature equation in terms of $\Delta T$ by substituting $T = T_{ref} + \Delta T$ and $p_{mod} \equiv p_{mech} - p_{static}$ into Eq. (2.9)

$$\rho c_p \frac{D\Delta T}{Dt} = k \frac{\partial^2 \Delta T_{ref}}{\partial x_i \partial x_i} + \beta \Delta T_{ref} \frac{Dp_{mod}}{Dt} + \mu \Phi + \cancelto{0}{\left[ \frac{\partial}{\partial x_i} k \frac{\partial T_{ref}}{\partial x_i} - u_j \frac{\partial T_{ref}}{\partial x_j} \right]}, \tag{2.10}$$

where the spatial derivatives of $T_{ref}$ can be neglected if $T_{ref}$ is a constant in space. Since for this experiment, $T_{ref}$ is set as a constant, the spatial derivatives can be neglected.

Eqs. (2.2), (2.7) and (2.10) pose a closed system of equations, although simplifications to the equations can still be made analyzing the dimensionless numbers of the experiment.

### 2.1.2 Dimensionless equations governing the experiment

Writing the equations in dimensionless form allows for further simplifications through the calculation of dimensionless numbers or groups. The influence of each term can then be easily assessed, which poses a significant advantage in analyzing complex flows, like in this case.

#### Characteristic scales and dimensionless form of the governing equations

The first step for deriving the dimensionless form of the governing equations is to define non-dimensional variables $x_i^*$, $u_i^*$, $t^*$, $p^*$, $\theta$ and $\Phi^*$ and normalize them by the characteristic scales of the flow. These may be defined as follows, see Schlichting & Gersten (2017) or Ferziger & Peric (2008),

$$x_i^* = \frac{x_i}{l_c}; \; u_i^* = \frac{u_i}{U_c} = \frac{u_i}{U_{in}}; \; t^* = \frac{t}{t_c} = t \frac{U_c}{l_c}; \; p^* = \frac{p_{mod}}{\rho_{ref} U_c^2};$$

$$\theta = \frac{T - T_b}{T_w - T_b} = \frac{\Delta T_b}{\Delta T_c}\,;\; \Phi^* = \frac{l_c^2}{U_c^2}\Phi, \tag{2.11}$$

where $l_c$, $U_c$ and $t_c$ are the characteristic length, velocity[3] and time scales, respectively. The viscous dissipation $\Phi$ is normalized taking the characteristic length and velocity. The *dimensionless* temperature difference $\theta$ is normalized by the *characteristic* temperature difference $\Delta T_c$, which *can* - but doesn't *need* to - be defined as the difference between the heated surface temperature $T_w$ and an *ad hoc* bulk flow temperature $T_b$. Alternatively for this particular geometry, it is possible to define $\Delta T_c$ in terms of the specific heat flux $\dot{q}$ by means of Fourier's empirical law for heat conduction, see Bejan (2013) as

$$\Delta T_c \sim \frac{\dot{q} l_c}{\lambda_{ref}}, \tag{2.12}$$

assuming that the heat flux $\dot{q}$ normal to the heated plate is mostly due to the effects of thermal conduction, which may be taken as a first approximation for $Pr \ll 1$ flows in an order of magnitude sense. Thus, in this study the dimensionless temperature difference is defined as

$$\theta = \frac{\Delta T_b}{\Delta T_c} = \frac{T - T_b}{\frac{\dot{q} l_c}{\lambda_{ref}}}. \tag{2.13}$$

Furthermore, relative fluid properties can be defined as the ratio of the local value of the respective fluid property with its reference value,

$$\rho^* = \frac{\rho}{\rho_{ref}}\,;\; \mu^* = \frac{\mu}{\mu_{ref}}\,;\; \lambda^* = \frac{\lambda}{\lambda_{ref}}\,;\; c_p^* = \frac{c_p}{c_{p,ref}}\,;\; \nu^* = \frac{\nu}{\nu_{ref}}, \tag{2.14}$$

where $\nu \equiv \mu/\rho$ is the kinematic viscosity.

Substituting the characteristic scales into Eqs. (2.2), (2.7) and (2.9) one obtains,

$$\frac{\partial u_i^*}{dx_i^*} \approx 0; \tag{2.15}$$

[3] In the case of pure natural convection flows, one may define the characteristic velocity $U_c$ as a velocity scale due to a temperature difference between a heated plate and a reference temperature, e.g. $\sqrt{g\beta_{ref}(T_w - T_b)L_c}$, see Kays *et al.* (2007).

$$\rho^* \frac{Du_i^*}{Dt^*} \approx \underbrace{\left(\frac{g\beta_{ref}\Delta T_c l_c}{U_c^2}\right)}_{\Pi_1}\theta\hat{x} - \frac{\partial p^*}{\partial x_i^*} + \underbrace{\left(\frac{\nu_{ref}}{U_c l_c}\right)}_{\Pi_2}\frac{\partial}{\partial x_j^*}\mu^*\left(\frac{\partial u_i^*}{\partial x_j^*} + \frac{\partial u_j^*}{\partial x_i^*}\right); \tag{2.16}$$

$$\rho^* c_p^* \frac{D\theta}{Dt^*} = \underbrace{\left(\frac{\nu_{ref}}{U_c L_c}\right)}_{\Pi_2}\underbrace{\left(\frac{1}{\nu_{ref}}\frac{\lambda_{ref}}{\rho_{ref}c_{p,ref}}\right)}_{\Pi_3}\lambda^*\frac{\partial^2\theta}{\partial x_i \partial x_i^*} +$$

$$+ \underbrace{\left(\frac{U_c^2}{c_{p,ref}\Delta T_c}\right)}_{\Pi_4}\underbrace{\left(\beta_{ref}\Delta T_c\right)}_{\Pi_5}\beta^*\theta\frac{Dp^*}{Dt^*} + \underbrace{\left(\frac{\nu_{ref}}{U_c l_c}\right)}_{\Pi_2}\underbrace{\left(\frac{U_c^2}{c_{p,ref}\Delta T_c}\right)}_{\Pi_4}\mu^*\Phi^*; \tag{2.17}$$

where the non-dimensional groups $\Pi_i$ with $i = 1, ..., 5$ have been identified and are defined as follows, see Schlichting & Gersten (2017),

$$\Pi_1 = Ri \equiv \frac{g\beta_{ref}\Delta T_c l_c}{U_c^2} = \frac{Gr}{Re^2};$$

$$\Pi_2 = \frac{1}{Re} \equiv \frac{\nu_{ref}}{U_c l_c};$$

$$\Pi_3 = \frac{1}{Pr} \equiv \frac{1}{\nu_{ref}}\frac{\lambda_{ref}}{\rho_{ref}c_{p,ref}} = \frac{a_{ref}}{\nu_{ref}};$$

$$\Pi_4 = Ec \equiv \frac{U_c^2}{c_{p,ref}\Delta T_c};$$

$$\Pi_5 = K_\rho \equiv \beta_{ref}\Delta T_c, \tag{2.18}$$

where $Ri$ is the RICHARDSON number[4]; $Gr$ the GRASHOF number defined as $\frac{g\beta_{ref}\Delta T_c l_c^3}{\nu_{ref}^2}$; $Re$ the REYNOLDS number; $Pr$ the PRANDTL number; $Ec$ the ECKERT number and $K_\rho$ for thermal expansion number. Furthermore, the molecular thermal diffusivity is defined as $a \equiv \lambda/\rho c_p$, where all fluid properties are evaluated at the reference temperature $T_{ref}$.

It can be shown that in the context of this work the pressure work and the viscous dissipation terms can be neglected, for details see appendix A. Hence, the final set

[4]In the literature $\Pi_1$ is also called the ARCHIMIDES number

of equations to be used for this experiment read

$$\frac{\partial u_i^*}{dx_i^*} \approx 0; \tag{2.19}$$

$$\rho^* \frac{Du_i^*}{Dt^*} \approx Ri\,\theta\hat{x} - \frac{\partial p^*}{\partial x_i^*} + \frac{1}{Re}\frac{\partial}{\partial x_j^*}\mu^* \left(\frac{\partial u_i^*}{\partial x_j^*} + \frac{\partial u_j^*}{\partial x_i^*}\right); \tag{2.20}$$

$$\rho^* c_p^* \frac{D\theta}{Dt^*} \approx \frac{1}{Re\,Pr}\frac{\partial^2 \theta}{\partial x_i^* \partial x_i^*}, \tag{2.21}$$

where $\mu^*$ may be expressed in either linear or non-linear form, depending on the chosen temperature range (see the appendix A).

**Physical interpretation of dimensionless numbers**

It is possible to deduce or assign a physical interpretation to dimensionless groups or numbers. For example, this can be done as a result from fractional or the method of differential equations, see Zierep (1991) or Bejan (2013).

Fractional analysis calculates the ratio between two terms of Eq. (2.7) (force ratios) or Eq. (2.9) (energy ratios). The two dominant terms to be analyzed must be first expressed in dimensionless form using Eqs. (2.11). Since each term of Eqs. (2.7) and (2.9) can be assigned with a physical interpretation, the ratio between two terms gives a notion of the relative importance of each term with respect to another. The Reynolds and Richardson number are two examples. The former is the ratio between inertial and viscous forces in a flow, while the latter is the ratio between buoyancy and inertial forces.

Other dimensionless numbers are best interpreted by means the method of differential equations, e.g. the Prandtl number $Pr$. Equating the convection and the conduction terms in Eq. (2.9) and by selecting the proper length and velocity scales for the boundary layer along a heated wall, the following result is obtained for liquid metal flows ($Pr \ll 1$)

$$\frac{\delta}{\delta_T} \sim \frac{1}{\sqrt{Pr}}, \tag{2.22}$$

where $\delta$ is the velocity boundary layer thickness and $\delta_T$ is the thermal boundary layer thickness.

Hence, $Pr$ expresses the ratio between the velocity and thermal boundary layer thickness, i.e. the ratio between the viscous and thermal diffusivity of a fluid.

For fluids with $Pr \sim 1$, the velocity and thermal boundary layer thickness scale as $Pr^{-1/3}$.

The presented physical interpretation to the dimensionless numbers gets more clear in the next sections within their context of use, however the need to physically interpret dimensionless numbers must not be exaggerated, as mentioned by Merker (1987).

### 2.1.3 Convective heat transfer regimes and other important dimensionless numbers

So far, the influence of $Ri_h$ and $Pr$ on the equations of motion hasn't been considered. In this section, $Ri_h$ is used to define the convection regimes, the Nusselt number $Nu$ is introduced and some peculiarities for the $Pr \ll 1$ case are mentioned.

#### Regime definition

In general terms, for convective heat transfer, so-called *regimes* can be defined. They denote flow states related to the flow driving force.

First, forced convection corresponds to the case when the first term on the right-hand side in Eq. (2.20) can be neglected. Hence, when no body forces are present in the flow and the flow is driven only due to an externally imposed pressure gradient, e.g. a pump. Vice versa, in the case of *natural* or *free convection,* only body forces are the driving force of the flow, i.e. the pressure gradient term in Eq. (2.20) is equal to zero. A third pseudo-regime may be defined as *mixed convection*, which occurs if both pressure gradient and body forces contribute to the flow motion, thus when forced and natural convection regimes coexist. Mixed convection may be stated as the *transition* from one regime to another.

In terms of dimensionless numbers, one may define the convective regimes in terms of the relative importance of each term in Eq. (2.20), i.e. in terms of the Richardson number $Ri$ (Cebeci & Bradshaw (1984), Kays *et al.* (2007) and Bejan (2013), Merker (1987)). Generally, flows with $Ri \ll 1$ are driven by forced convection, while flows with $Ri \gg 1$ are dominated by natural convection. Thus, for $Ri \sim 1$ both convective regimes interact and must be considered in the analysis.

#### Onset to mixed convection

Lloyd & Sparrow (1970) theoretically estimated critical values for the Richardson

$Ri_{crit}$ number for the case when natural convection effects begin to be noticeable in a forced convection flow, i.e. the onset to mixed convection. Their analysis is based on a theoretical similarity analysis for a vertical heated plate. They determined $Ri_{crit}$ by taking the value of $Ri$ at which a 5% deviation for the NUSSELT number from the forced convection case is observed. Here, the Nusselt number is defined as

$$Nu \equiv \frac{\alpha\, l_c}{\lambda_{ref}} = \frac{\dot{q} l_c}{\lambda_{ref}\,(T_w - T_b)} = -\left.\frac{\partial T^*}{\partial y^*}\right|_{y^*=0}, \tag{2.23}$$

where $\alpha = \dot{q}/(T_w - T_b)$ is the convective heat transfer coefficient, see Jischa (1982); $\dot{q}$ the specific heat flux; $T_w$ the heated wall temperature; $T_b$ an ad hoc defined fluid bulk temperature, see Moffat (1998) and Bejan (2013), and $\frac{\partial \Delta T^*}{\partial y^*}$is the dimensionless temperature gradient evaluated at the heated wall. The Nusselt number can be alternatively *defined* as be the gradient of the dimensionless temperature gradient *at* a heated (or cooled) wall, hence giving a notion of the relative importance of local convective heat transfer versus conduction heat transfer *near* the wall, i.e. in the boundary layer.

Jischa (1982) shows the following order of magnitude relationship

$$Nu \sim \frac{l_c}{\delta_T}, \tag{2.24}$$

where $\delta_T$ is the thermal boundary layer thickness[5].

The results of the analysis of Lloyd & Sparrow (1970) are shown in Table 2.1. One can observe that for the liquid metal case, i.e. $Pr \ll 1$, the order of magnitude for the critical Richardson number is around $Ri_{crit} \sim 0.05$. From their analytical considerations, it can be deduced that liquid metal convective flows tend to be much more sensitive to buoyancy fluids with $Pr \sim 1$ or $Pr \gg 1$. The reason is that due to their very high thermal diffusivity, which temperature "spreads" much more efficiently and faster from a heated wall towards the flow core. In other words, compared to regular fluids (air, water) heated liquid metal flows will tend to have much bigger bulbs with a different density than rest of the flow. As a consequence, when analyzing both experimental and simulation results for the liquid metal case, one must be very careful when assuming the *pure* forced convection case (Pacio *et al.* (2015); OECD/NEA (2015)). This has been also mentioned by Grötzbach (2013) for application of numerical flow simulations in the nuclear sector.

[5]This relationship may serve as a rough order of magnitude estimate when discretizing a geometry into a mesh.

Table 2.1: Critical Richardson number for various Prandtl numbers. Data from Lloyd & Sparrow (1970) for forced convection over a vertical heated plate based on a similarity analysis. The fluid examples are given as a order of magnitude reference.

| $Pr$ | 100 | 10 | 0.72 | $0.03-0.003$ |
|---|---|---|---|---|
| Fluid example | Oils | Molten salts | Air and water | Liquid metals |
| $Ri_{crit}$ | 0.24 | 0.13 | 0.08 | $0.056-0.050$ |

**Comments on the natural convection case for $Pr \ll 1$**

As pointed out by Kakac (1987), by Bejan (2013) and by Merker (1987), a clear distinction must be made for the determination of $Nu$ for pure liquid metal natural convection. Usually for the case of $Pr > 1$, the Nusselt number for natural convection depends on the product of the Grashof and the Prandtl number, as

$$Nu_{Pr>1} = f(GrPr), \tag{2.25}$$

where the product $GrPr$ denotes the RAYLEIGH number $Ra \equiv GrPr$.

For liquid metals, i.e. $Pr \ll 1$, it can be shown that it is the square of the Prandtl number that plays a role in the determination of the Nusselt number, see Bejan (2013). That is,

$$Nu_{Pr\ll 1} = f\left(GrPr^2\right) = f(RaPr), \tag{2.26}$$

where the product $RaPr$ is usually is termed as the BOUSSINESQ number $Bo \equiv RaPr$. This difference in functional dependency is important when analyzing the flow of natural (or mixed) convection. For a comment on the physical interpretation to be given to $Gr$, $Bo$ and $Ra$, the reader is referenced to the appendix G.

## 2.2 General BFS flow description and definitions

**Flow description**

The general flow scenario is described based on the nomenclature and variable definition illustrated in Fig. 2.1.

The flow enters the BFS geometry through the inlet with constant bulk velocity $U_b$. Depending on the upstream flow characteristics, the *inlet section* length,

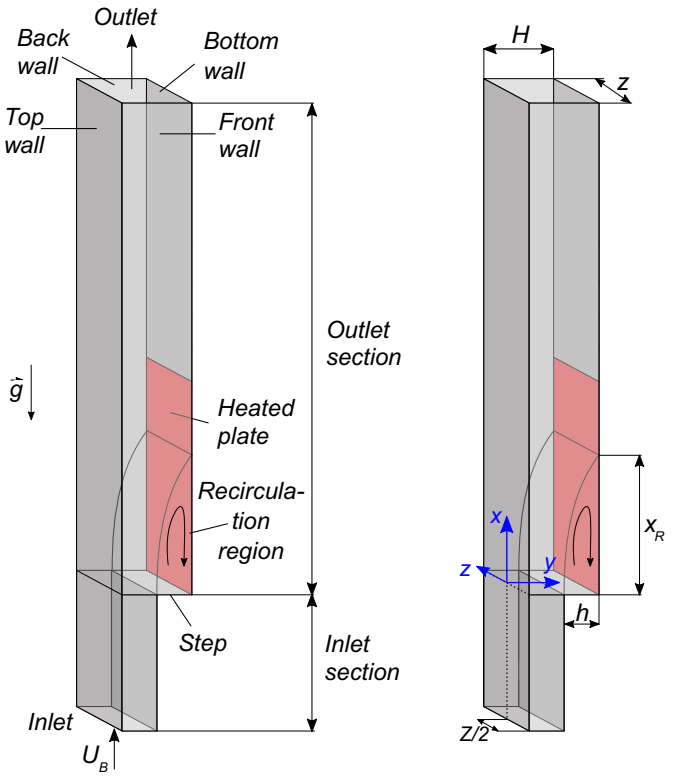


Figure 2.1: Sketch of a backward facing step (BFS) geometry. The nomenclature, reference coordinate system and its origin used in this study are defined as shown in the sketch.

its height ($H - h$) and the flow Reynolds number $Re_h$ (based on $U_b$ and the step height $h$), the boundary layer regime, thickness and turbulence intensity varies. The channel width $Z$ plays a major role in the flow characteristics as well as shown later.

The velocity boundary layer is perturbed by the channel sudden expansion at the *step* and detaches from the wall. A shear layer forms together with a recirculation region. The point at the *heated plate,* where the time averaged flow velocity is zero is defined as the reattachment point $x_R$. By exceeding a certain $Re_h$ threshold the BFS flow becomes highly unstable so that the definition of $x_R$ is only valid only in a statistically stationary sense. Downstream of $x_R$, a new boundary layer develops and growths under non-equilibrium conditions and the flow gradually returns to a fully developed channel flow state, see Bradshaw & Wong (1972).

### Geometrical definitions

The two most important geometry relations of a BFS are the aspect ratio and the expansion ratio. The aspect ratio $AR$ of a BFS is defined as $AR \equiv Z/h$ and the expansion ratio $ER$ is defined as $ER \equiv H/h$, see Fig. 2.1. The definition of these two geometric parameters is not arbitrary since the BFS flow structure is directly related to the numerical value of $AR$ and $ER$.

Depending on the $AR$, so-called *secondary flow of the second kind* may be of importance in the experiment. In rectangular ducts corner vortices form and transport fluid along the duct cross-sectional plane, see Bradshaw (1987). There is still no full agreement on the physical mechanism behind this flow phenomena, as discussed in Pinelli *et al.* (2010) and Nikitin *et al.* (2019). A systematic DNS analysis of the effect of secondary flow of the second king as a function of the aspect ratio in duct flow can be found in Vinuesa *et al.* (2018). De Brederode & Bradshaw (1972) determined experimentally that if $AR > 10$, the effect of corner vortices can be neglected at the $XY-$center plane at $z = Z/2$ for a BFS. In the literature, BFS flows with $AR \geq 10$ are termed as *non-confined* BFS flows, while BFS with $AR < 10$ are referred as *confined* BFS flows. Some studies also refer to BFS flows with $AR > 10$ as two-dimensional BFS; however, this concept is misleading, since turbulent flows are - per definition - three-dimensional.

A systematic assessment of the influence of $ER$ on a non-confined BFS can be found in Nadge & Govardhan (2014). They report that the reattachment point $x_R$ increases with $ER$ and the Reynolds number $Re_h$, where for $Re_h$ the step height $h$ is taken as the characteristic length and the bulk inlet velocity $U_b$ as the characteristic

velocity. However, at sufficient high $Re_h$, i.e. $Re_h > 20000$, $x_R$ stagnates at $x_R \approx 8.5$ for $ER > 1.8$.

## 2.3 Literature review on low Prandtl BFS flow

The experiment treated in this study is the first low Prandtl ($Pr \ll 1$) BFS experiment available in the open literature. The only BFS experiment for *moderate* low Prandtl ($Pr < 1$) BFS is described by Buckingham (2018), in which a mixture of helium and xenon is used to achieve $Pr < 0.71$ (air).

A comprehensive literature summary of all isothermal and non-isothermal BFS experiments and direct numerical simulations, mainly for $Pr \sim 1$, can be found in Chen *et al.* (2018). Nadge & Govardhan (2014) present an analysis of past and own experimental results ($Pr \sim 1$) demonstrating the dependence of the BFS recirculation region structure on geometrical and flow parameters.

In the absence of any other BFS experiments for $Pr \ll 1$ in the open literature, a literature review is presented on the numerical work conducted in the past years for $Pr \ll 1$ BFS.

Niemann & Fröhlich (2016b) ran the first DNS for a $Pr \ll 1$ BFS available in the literature. They simulated a non-confined BFS using sodium as a working fluid ($Pr = O(10^{-3})$) for both forced and mixed convection regimes at a Reynolds number of $Re_h = 4805$, based on the inlet bulk velocity and the step height. In Niemann & Fröhlich (2017), they extended their analysis of the flow by analizing the turbulence budgets of the flow. Niemann & Fröhlich (2016b) DNS data set triggered many turbulent heat flux model validation cases listed in the following paragraphs[6]. The reader is forwarded to appendix B for a short conceptual introduction to the different approaches to model turbulent heat fluxes (and also Reynolds stresses).

Schumm *et al.* (2018) modeled the Reynolds stresses $\left\langle u_i' u_j' \right\rangle$ using the Boussinesq analogy and calculated the eddy viscosity $\nu_t$ with a low Reynolds number $k-\varepsilon$ model. For the modeling of $\langle u_i' T' \rangle$ they assumed the simple gradient hypothesis and calculated the eddy diffusivity $\alpha_t$ by means of the Kays correlation for the turbulent Prandtl number $Pr_t$. Their results for velocity, turbulent kinetic energy and Reynolds shear stresses are in good agreement with the data of Niemann & Fröhlich (2016a) for the mixed convection regime. For the forced convection regime their results differ significantly. The Stanton number $St = {Nu}/{(Re\,Pr)}$ distribution along the

[6] In the cited validation cases, statements on the quantitative agreement or discrepancy with the reference data of Niemann & Fröhlich (2016b), either relative or absolute, are not given.

heated plate agrees qualitatively with the DNS data, but quantitatively underpredicts the heat transfer in the the mixed convection regime.

De Santis & Shams (2018) used the same approach for $\left\langle u_i' u_j' \right\rangle$ as Schumm *et al.* (2018), but calculated $\langle u_i' T' \rangle$ with an algebraic turbulent heat flux model. Their model for $\langle u_i' T' \rangle$ is based on the model of Kenjeres *et al.* (2005) and introduces new model constants for $Pr \ll 1$ fluids and all convection regimes. For the forced convection case, their results are in good agreement with the reference data of Niemann & Fröhlich (2016b) for velocity, turbulent kinetic energy and Reynolds shear stresses. For the mixed convection case, the flow field is also in good agreement, but the turbulent kinetic energy and the Reynolds shear stress exhibit quantitative discrepancies. The thermal field and the local $Nu$ number along the heated plate is also in good agreement. No quantitative statement can be done regarding the agreement between their simulations and the reference data, since

Da Via & Manservisi (2019) developed a so-called $2+2$ model, calculating $\left\langle u_i' u_j' \right\rangle$ with a low Reynolds $k-\omega$ two-equation model for the eddy viscosity $\nu_t$. The eddy diffusivity $\alpha_t$ is also calculated with a two-equation model (following a $k_\theta - \omega_\theta$ approach). A correction term is included to account for the different time scales of the flow and the temperature fields. They also studied the effect of different thermal boundary conditions for the heated plate and introduced further correction terms for bulk heat transfer effects (with the Kays correlation). They report reasonable agreement with the DNS data of Niemann & Fröhlich (2016b) for both mixed and forced convection flows for the velocity and thermal fields, turbulent kinetic energy turbulent heat fluxes, and RMS-values for the temperature fluctuations.

Star *et al.* (2021) developed a proper orthogonal decomposition POD-Galerkin reduced order model for the calculation of a sodium non-confined BFS and compared the results to complementary conducted RANS simulations. They report good agreement between the POD-Galerkin model and the RANS results at a much shorter calculation time compared to the RANS calculations.

In the past years, the DNS database for $Pr \ll 1$ BFS cases has further increased. Oder *et al.* (2019) performed a DNS simulation for confined BFS with liquid sodium ($Pr = O(10^{-3})$) for forced convection. The novelty of their work is the inclusion of the conjugate heat transfer calculation of the heated plate. They further compared their data with the model of Da Via & Manservisi (2019).

Wang *et al.* (2020), Zhao *et al.* (2018a) and Zhao *et al.* (2018b) conducted different DNS or quasi-DNS for non-confined BFS, also for mixed and forced convection

regimes, but for lead-bismuth ($Pr = O(10^{-2})$).

# 3

# Setup of the vertical BFS flow experiment

## 3.1 The liquid metal loop DITEFA 2

Here, a brief summary of the experimental setup is presented. More details can be found in Schaub *et al.* (2021) and Schaub *et al.* (2022).

The DITEFA 2 is a modular liquid metal experimental facility planned, designed, manufactured, commissioned and operated within the framework of this study. Its working fluid is the eutectic alloy of gallium, indium and tin (*GaInSn*). Its physical properties are shown in Table 3.1, together with those of liquid sodium and water as a comparison. *GaInSn* has the advantage of being a non-toxic liquid metal at room temperature. It has an almost negligible vapor pressure, making its handling easy and safe. Along with its disadvantages however, one may mention its chemical incompatibility with aluminum, its high price and large surface tension, which makes wetting of small objects and surfaces with GaInSn not an easy task. General handling guidelines for GaInSn can be found in Morley *et al.* (2008) and Cadwallader (2003). Long time studies on its chemical compatibility with metals and plastics have been recently published by Geddis *et al.* (2020).

The facility operation range is presented in Table 3.2 in terms of both absolute values and in terms of dimensionless numbers. $Pr$ has been calculated taking the range for $T_{ref}$. $Pe_h$ has been calculated taking a constant $Pr$ at $T_{ref} = 25\,^{\circ}C$ and varying $Re_h$ over its full range. The range for $Ri_h$ has been calculated by taking the heated plate maximum electric power input and varying $Re_h$ over its full range.

The design has been constrained by two mutually opposing factors: the very

low available pump head and the *relatively* low available inventory of liquid metal of 31 $l$. A sketch of the resulting facility and its components is shown in Fig. 3.1. All horizontal sections have a 4° inclination (not shown) to allow fast discharge of the fluid. Since every component is flanged to one another, they can be easily assembled and exchanged. The facility is thermally insulated, including its test section, the heated plate and the thermocouple connections.

The loop can be divided into five sections: the pump, the flow conditioning, the test section and the return and the flow metering sections.

### Pumping section

The liquid metal is pumped by a SAAS permanent magnet pump which is controlled by a Danfoss VLT digital variable frequency drive. The pump must be considered a heat source due to Ohmic heating caused by induced eddy current by the rotating magnets, see Buchenau (2012) and Davidson (2017). The pump duct made of stainless steel has a rectangular cross-section. Because of the curvature of the pump channel and the magnetohydrodynamic (MHD) interaction of the rotating permanent magnets with *GaInSn*, the outlet velocity profile is non-homogeneous and requires to be corrected to guarantee adequate inlet boundary conditions for the test section. Therefore, two *perforated plates* are installed in the pump outlet .

### Flow conditioning section

All components have been designed and positioned based on best practice guidelines and existing knowhow from wind tunnel and water channel designs. All components have been manufactured in-house.

Since the pump has a low pump head, the pressure drop along the flow conditioning section has to be minimized. This is achieved by progressively increasing the cross-section of the pump duct, which is realized in three steps by means of three *wide angle diffusers* (diffusers 1, 2 and 3 in Fig. 3.1). Wide angle diffusers are characterized by achieving large inlet-to-outlet area ratios in short distances. Boundary layer detachment along the wide angle diffusers is avoided by installing *vanes* and g*rids* or *screens*. A 90°*bend* with vanes has been installed between diffusers 2 and 3 to enable a smooth fluid turn. The third diffuser leads to the *settling chamber*. It is the main flow conditioning component, which consists of a grid, a honeycomb and two further grid stages. Finally, the *contraction 1* (5 : 1 inlet-to-outlet area ratio) connects the settling chamber to the inlet of *test section*.

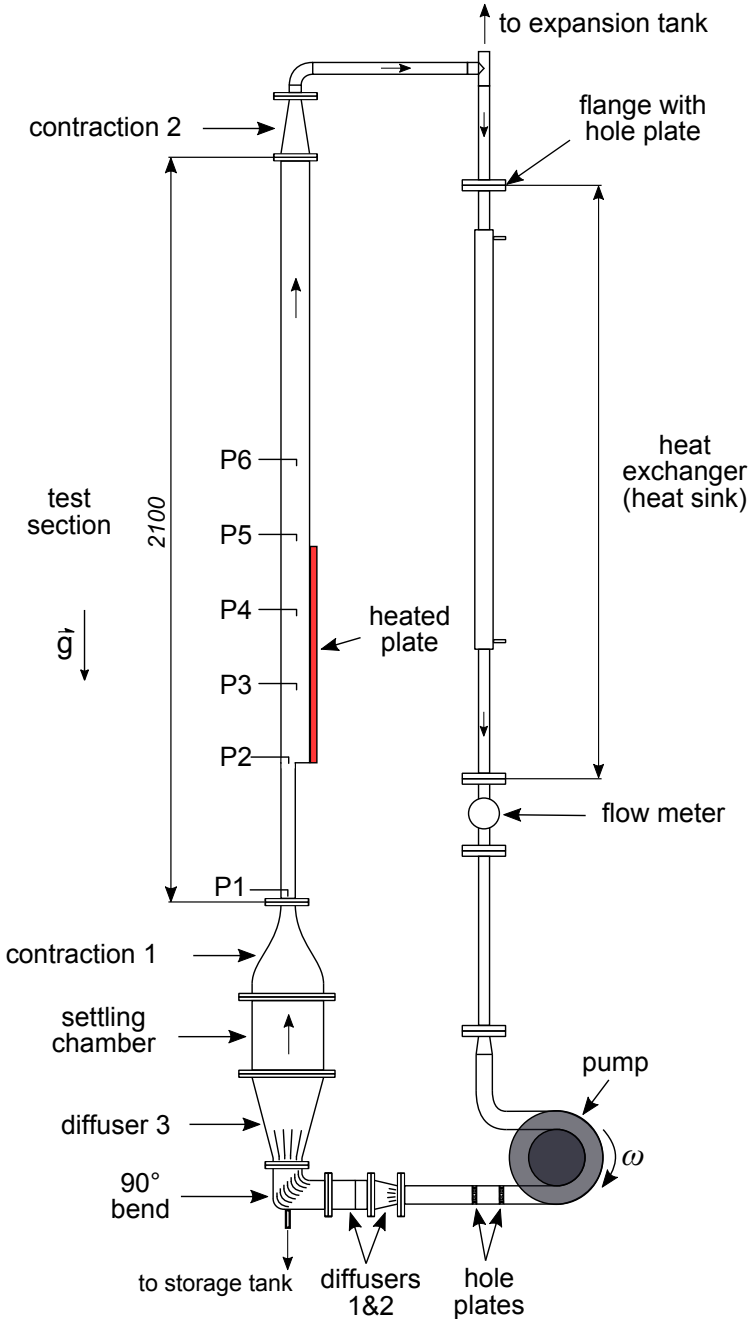


Figure 3.1: Sketch to scale of the DITEFA 2 facility. The fluid flows in clockwise direction, where $\omega$ is the angular velocity of the pump. The flow direction is also indicated by arrows in the loop. As a reference, the test section has a total length of $2100\,mm$. The relevant test section dimensions are shown in Fig. 3.2.

The spanwise dimension (i.e. "into the paper") from the 90°bend to the end of the test section is constant and equal to 80 *mm*. The lowest point of the facility is at the 90°*bend*, where the liquid metal storage tank is also connected.

#### Return section

The duct square cross-section profile of the test section is adapted to the return pipe by means of *contraction* 2 (duct-to-pipe adapter). This contraction doesn't play a role in the flow conditioning and its influence on the upstream flow is assumed negligible, since it is positioned far away from the region of interest, i.e. the recirculation region. The highest point of the loop is connected to a *expansion tank* to compensate for fluid volume variations during operation.

#### Heat exchanger

The in-house designed and manufactured *GaInSn*-to-water counter-flow *heat exchanger* removes the heat supplied to the *GaInSn* by the heated plate and the pump. The heat exchanging surfaces have been roughened to enhance the overall heat transfer coefficient. The heat exchanger cooling water is provided by a ERS ENERGIE- & KÄLTETECHNIK GMBH system cooler with a cooling power of 7.2 *kW* and a thermostat switching differential of 1.5 *K*.

## 3.2 Operational instrumentation of the DITEFA 2 loop

#### Flow meters

Three flow meters with different operating principle have been tested: an ABB Hygenic Master inductive flow meter (IFM), a NATEC NT turbine flow meter (TFM) and an EMERSON Micro Motion ELITE Coriolis flow meter (CFM). The IFM have been mounted in series to the TFM and both have been tested simultaneously during the commissioning phase of the facility. Both flow meters require an inflow without any large upstream flow disturbances (high flow swirl and large eddies) and a sufficiently long outflow. Therefore, a perforated plate is installed upstream of the heat exchanger inlet to remove any traces of swirl in the flow. Furthermore, since both flow meters have been calibrated by external certified laboratories[1] with fully

[1] Deutsche Akkreditierungsstelle (DaKKs)

Table 3.1: Physical properties of gallium-indium-tin (*GaInSn*), liquid sodium (*Na*) and water ($H_2O$) at 1 $[bar]$. References: Emmendörfer (2015) and Plevachuk *et al.* (2014) for *GaInSn* , Sobolev (2011) for *Na* and, Lemmon *et al.* (2022) for $H_2O$.

| | *GaInSn* | *Na* | $H_2O$ |
|---|---|---|---|
| $T_{ref}$ $[^\circ C]$ | 25 | 200 | 25 |
| $\rho$ $[kg/m^3]$ | 6412 | 903 | 997 |
| $\mu$ $[mPa \cdot s]$ | 2.10 | 0.45 | 0.89 |
| $\nu$ $[m/s^2]$ | $0.32 \cdot 10^{-6}$ | $0.50 \cdot 10^{-6}$ | $0.89 \cdot 10^{-6}$ |
| $\lambda$ $[W/(m \cdot K)]$ | 25.06 | 81.94 | 0.68 |
| $c_p$ $[J/(kg \cdot K)]$ | 400 | 1343 | 4218 |
| $a$ $[m/s^2]$ | $9.78 \cdot 10^{-6}$ | $67.57 \cdot 10^{-6}$ | $0.16 \cdot 10^{-6}$ |
| $Pr$ $[-]$ | 0.034 | 0.007 | 5.52 |
| $\gamma[N/m]$ | 0.59 | 0.19 | 0.07 |
| $\sigma[S/m]$ | $3.25 \cdot 10^6$ | $7.70 \cdot 10^6$ | $5.49 \cdot 10^{-6}$ |

Table 3.2: Operation range of the DITEFA 2 facility in absolute terms and expressed in dimensionless numbers.

| | minimum value | maximum value |
|---|---|---|
| $T_{ref}$ $[^\circ C]$ | 15 | 32 |
| $\dot{V}$ $[l/s]$ | 0.1 | 2.0 |
| $\dot{m}$ $[kg/s]$ | 0.64 | 12.82 |
| $U_{bulk,inlet}$ $[m/s]$ | 0.031 | 0.625 |
| $U_{bulk,outlet}$ $[m/s]$ | 0.016 | 0.313 |
| $\dot{q}$ $[W/m^2]$ | 0 | 14985 |
| $Re_h$ $[-]$ | 3813 | 76256 |
| $Pr$ $[-]$ | 0.036 | 0.032 |
| $Pe_h$ $[-]$ | 128 | 2557 |
| $Ri_h$ $[-]$ | 0.003 | 1.14 |

developed inlet velocity profiles, it is recommended to attain to these boundary conditions to achieve the instrument *accuracy* indicated in the calibration certificate.

The TFM did not work properly over longer periods of time. However, when it did, the agreement between the measured values for the IFM and the TFM has been excellent. The reason for the day-to-day functionality variability of the TFM is thought to be related with issues regarding the turbine plain bearing, as it needs to be lubricated with the working fluid itself: the clearance between the rotor and the plain bearing is narrow while the surface tension of the *GaInSn* is very high (see Table Table 3 in the appendix). Another issue with the TFM is its negative influence on the flow conditioning section. The induced flow swirl could not be fully corrected by the flow conditioning measures. Hence, the TFM has been demounted from the facility, leaving only the IFM installed for the experimental campaign. The accuracy of the used IFM is 0.42% as indicated by the calibration certificate of the manufacturer. For details on how the IFM accuracy influences the measurement uncertainty, see the appendix E.

Due to time and space constraints, the CFM has been tested separately after the experimental campagin. If one assumes the measurement of the CFM to represent the true value for the mass flow rate measurement, the measurement error of the inductive flow meter is in fact negligible. This, in spite of the IFM being calibrated in water. Water and *GaInSn* have different electron/molecular configurations (van der Waals forces versus electron cloud, respectively). Hence, the transferability of the calibration of the IFM from water to *GaInSn* is not obvious. Nevertheless, measurements at the Karlsruhe Liquid Metal Lab (KALLA) showed that the difference between both measurements are indeed negligible within experimental uncertainty (private communication). It consists of an inductive flow meter and a turbine flow meter.

**Temperature sensors (thermocouples)**

In addition to the thermocouples installed in the test section for the experiment purposes (heated plate and permanent magnet probes), a total of 8 thermocouples are installed along the DITEFA loop to monitor the liquid metal temperature. Two type T-thermocouples are placed at the inlet and the outlet of the pump rectangular channel, while 3 thermocouples are mounted at each the heat exchanger inlet and outlet at different pipe radial positions to account for possible not fully developed thermal boundary layer effects (which proved to be negligible).

**Pressure sensors**

One absolute and two differential SIEMENS SITRANS DS III/P410 pressure sensors have been mounted to the test section to measure the loop absolute pressure at its lowest point to monitor the filling process of the loop and to measure the pressure drop along the test section. During the facility commissioning, we noticed liquid metal leaks in all pressure transducers. For this reason, the sensors have been unmounted and the pressure drop along the test section has not been measured during the actual measurement campaign.

## 3.3 The BFS test section

The test section dimensions, the instrumentation position and numbering nomenclature are indicated in Fig. 3.2 in dimensionless form normalized by the step height $h = 40\,mm$. The test section has an expansion ratio $ER$ and an aspect ratio $AR$ of 2.

The test section has been manufactured based on a double-wall-channel concept with an inner channel material made of polyetheretherketone (PEEK) enveloped by an external housing made of stainless steel (Fig. 3.3). In the inlet section, a trip wire is fixed along the inner perimeter of inlet channel[2]. The wire has a rectangular shape of $2\,mm$ times $2\,mm$. Its position indicated in Fig. 3.2 is taken from the inlet to the trip wire center. Right after the BFS step located at $x = 0\,h$, a copper heated plate is mounted. It consists of two copper blocks: an *inner* and an *outer* block. The inner block is in direct contact with the liquid metal and also acts as a sealing element of the PEEK/stainless steel structure. The outer block is the heated plate in which electrical resistance heaters are embedded.

Along the test section, six so-called permanent magnet probes (PMP) allow the local and simultaneous measurement of the fluid temperature and velocity at the test section center plane $z = {}^{Z}/_{2} = 1h$ . The local temperature near the interface between the heated plate and the liquid metal is measured by means of 120 type $K$ thermocouples arranged in five columns ($A$ to $E$), each with 24 thermocouples. The thermocouple column positioning measures are indicated in Fig. 3.2. The thermocouples are guided from outside through the heated plate to a distance of $0.5\,mm$ from the liquid-wall interface, see Fig. 3.4.

[2]In left photograph in Fig. 3.3 the trip wire can be seen behind the white teflon stopper.

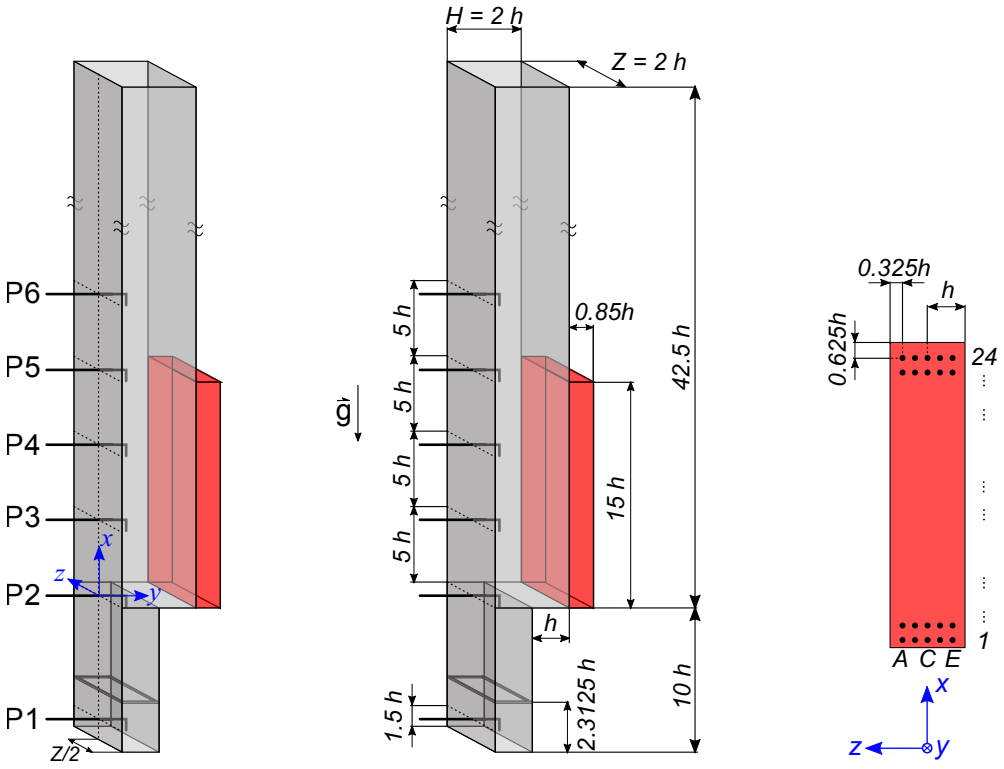


Figure 3.2: Sketch of the vertical confined backward facing step test section (left and center) and its heated plate (right). The black dots in the right figure represent the embedded thermocouples in the heated plate. All dimensions are normalized by the step height $h = 40mm$. The reference coordinate system, its origin and the probe numbering nomenclature are defined as shown in the left sketch.

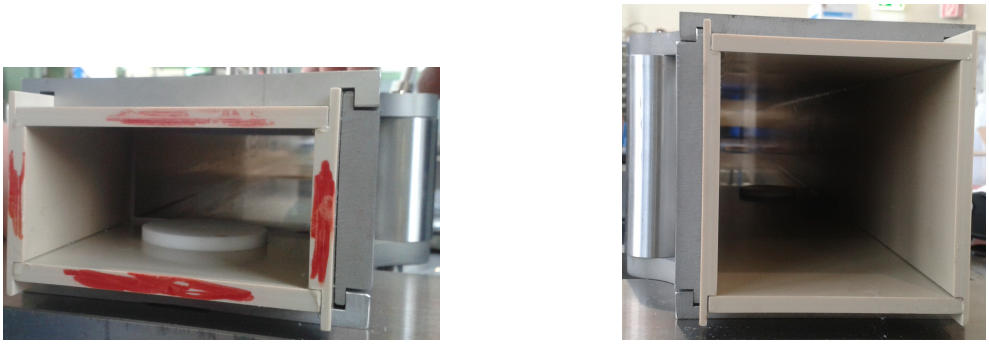

Figure 3.3: Pictures of the double-wall concept chosen for the manufacturing of the test section.

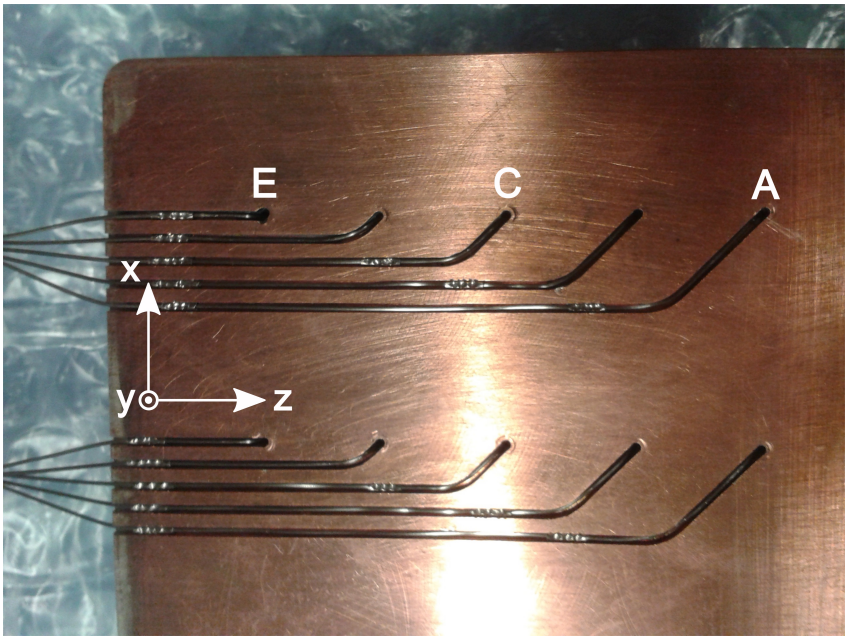


Figure 3.4: Picture of the backside of the heated plate first block. Picture of the backside of the heated plate first block. The thermocouple diameter is 1 *mm* as a scale reference.

## 3.4 Probes for the local and combined measurement of fluid velocity and temperature

The used permanent magnet probe (PMP) for the local measurement of flow velocity and temperature is introduced. From now on, PMP or simply "probe" are used indistinctly. The probes and their measurement chain have been developed and manufactured from scratch and in parallel to the design, manufacturing and commissioning of the facility and its test section. A detailed description of the developed probe is found in Schaub *et al.* (2021). Here, only a broad overview is given.

### 3.4.1 Construction and working principle

#### Construction

A picture of the developed permanent magnet probe is shown in Fig. 3.5, whereas in Fig. 3.6 the mounting into its housing is illustrated. A sketch of the probe is shown in Fig. 3.7 from different perspectives.

The probe consists basically of five components:

i. A cylindrical shaped sheath made of polyether ether ketone (PEEK) which is glued to a stainless steel (SS) probe shaft or sheath. The probe sheath is welded to a stainless steel support shaft. The distance between the support shaft axis and the probe tip is $30\,mm$.

ii. Inside the probe tip, an annular shaped permanent magnet with diametric magnetization direction is positioned so that the north pole of the magnet points in the $-y$ direction (Fig. 3.7).

iii. A thermocouple is passed through the permanent magnet and guided approximately $0.5\,mm$ outside of the probe tip ($TC3$ in Fig. 3.7).

iv. Two additional thermocouples of the same size as are embedded and guided outside and along the probe tip on opposite sides ($TC1$ and $TC2$ in Figure 2). These thermocouples are electrically insulated from the liquid metal with glue along their length, except for the immediate vicinity at their tips (Fig. 3.6).

All three thermocouples are of type $K$, with an ungrounded measurement junction, an outer diameter of $0.25\,mm$ and a length of $500\,mm$. All used thermocouples are enclosed by a stainless steel sheath (1.4401) along their complete extension and have been manufactured from one batch by ThermoExpert GmbH. They are guided inside the probe stainless steel sheath outside of the experiment. For the temperature measurement, not *compensation* but *extension* cables have been used (all also from one batch). The magnet is a neodymium ($NdFeB$) permanent magnet with an external diameter equal to its length $d_m = l_m = 1.0\,mm$ and a remanence of $1.4\,T$ (indicated by the manufacturer in the data sheet). The probe tip outer diameter is $d_{tip} = 1.6\,mm$, i.e. the support shaft-to-probe tip diameter ratio is 18.75. All components in the probe tip are glued together and electrically insulated from each other.

The probe tip positioning coordinates are indicated in Table 3.3, where the reference coordinate system defined in Fig. 3.2 is used as the reference. The probe positioning location indicated in Fig. 3.2 refers to the probe housing center axis; the actual probe measurement point is located $18.7\,mm = 0.4675h$ upstream from the probe housing center axis. Due to space constraints, the probe support shaft axis does not coincide with the probe housing center axis, as is observed in Fig. 3.6. The probes are transversed in the $y-$axis with TOLOMATIC ERD15 linear actuators with a positioning accuracy of $0.15\,mm$ and a backlash of $0.18\,mm$. To avoid

Table 3.3: Coordinates of the permanent magnet probe (PMP) measurement point.

| Probe number | $x\ [mm]$ | $y\ [mm]$ | $z\ [mm]$ |
|---|---|---|---|
| $P1$ | $-340-18.7=358.7$ | $5\leq y\leq 35$ | 0 |
| $P2$ | $0-18.7=-18.7$ | $5\leq y\leq 35$ | 0 |
| $P3$ | $200-18.7=181.3$ | $5\leq y\leq 75$ | 0 |
| $P4$ | $400-18.7=381.3$ | $5\leq y\leq 75$ | 0 |
| $P5$ | $600-18.7=581.3$ | $5\leq y\leq 75$ | 0 |
| $P6$ | $800-18.7=781.3$ | $5\leq y\leq 75$ | 0 |

the backlash induced positioning uncertainty, the probes are transversed only in one direction during the measurement campaign. The probes are transversed within a range $5\,mm$ from the test section walls to avoid accidental collisions and probe damage.

**Working principle of the probe**

The probe working principle is based on well known electromagnetic and MHD principles, a detailed review may be taken from Davidson (2017).

When a electrical conductive fluid particle flows with velocity $\vec{u}$ through an externally imposed magnetic field $\vec{B}$, an electromotive force $EMF$ will be induced according to Faraday's law of induction. This $EMF$ gives origin to a volumetric current density $\vec{J}$ according to Ohm's empirical law

$$\vec{J}=\sigma\left(\vec{E}+\vec{u}\times\vec{B}\right), \tag{3.1}$$

where $\sigma$ is the electrical conductivity of the liquid metal, $\vec{u}\times\vec{B}$ is the $EMF$ induced due to the relative motion between the fluid with velocity $\vec{u}$ and the magnetic field $\vec{B}$ and $\vec{E}$ denotes an externally imposed electric field; here it describes the resulting electric field due to the charge separation created by the $EMF$.

In non-isothermal liquid metal flows, thermo-electric $\vec{E}_{th,el}$ and thermo-magnetic $\vec{E}_{th,ma}$ electric potentials, may be induced as well. Thus, Eq. (3.1) can be expanded to

$$\vec{J}=\sigma\left(\vec{E}_{el}+\vec{E}_{th,el}+\cancelto{0}{\vec{E}_{th,ma}}+\vec{u}\times\vec{B}\right), \tag{3.2}$$

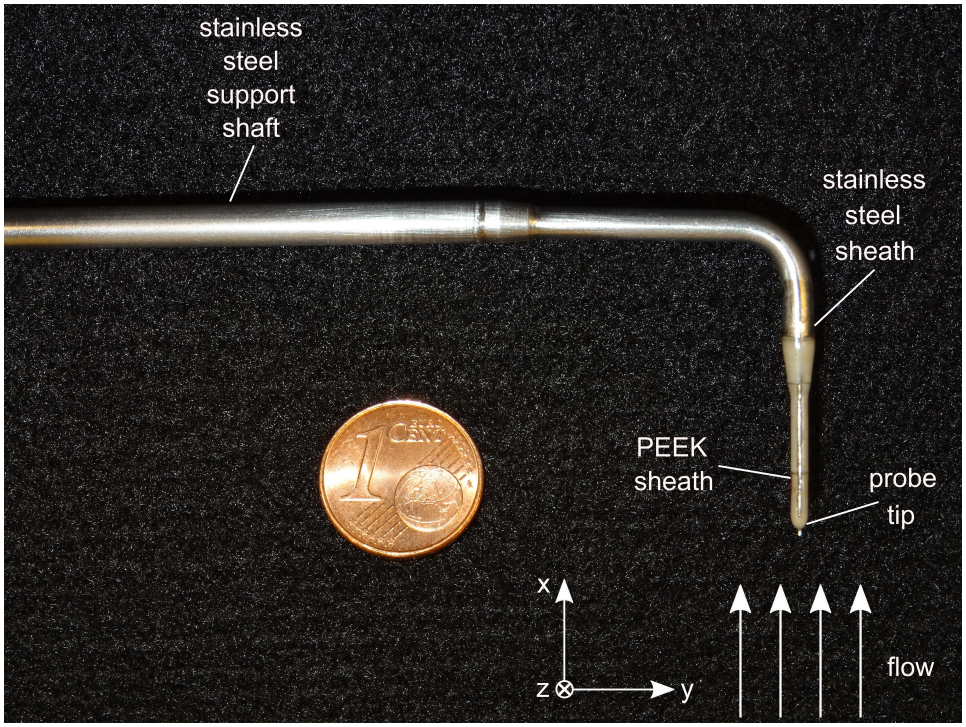


Figure 3.5: Photograph of the developed permanent magnet probe (PMP) with a probe tip diameter $d_{tip}$ of $d_{tip} = 1.6\,mm$ and a stainless steel sheath diameter of $3\,mm$.

where the thermo-magnetic effects can be shown to be neglected, see section 3.4.3.

### 3.4.2 Probe measurement equation

The derivation of the probe equation is not trivial as it includes the use of GREEN'S functions to solve the divergence of Eq. 3.2. A detailed derivation of the probe equation can be found in Kapulla (2000). Here, only the result is presented.

Taking the nomenclature of figure 3.8 and using Kirchhoff's voltage circuit law (positive in clockwise direction as shown in the sketch), the general measurement equation for the probe reads to

$$Ku_{vol} + S_{SS}(T_{amb} - T_1) - V_{SS} + S_{SS}(T_2 - T_{amb}) + S_{e,tip}(T_1 - T_2) + V_0 = 0 \quad (3.3)$$

where $K$ is the probe sensitivity or calibration constant determined empirically; $u_{vol}$ the volume averaged fluid velocity in the permanent magnet magnetic field sphere of influence, hence $Ku_{vol}$ is the induced velocity proportional component of the signal

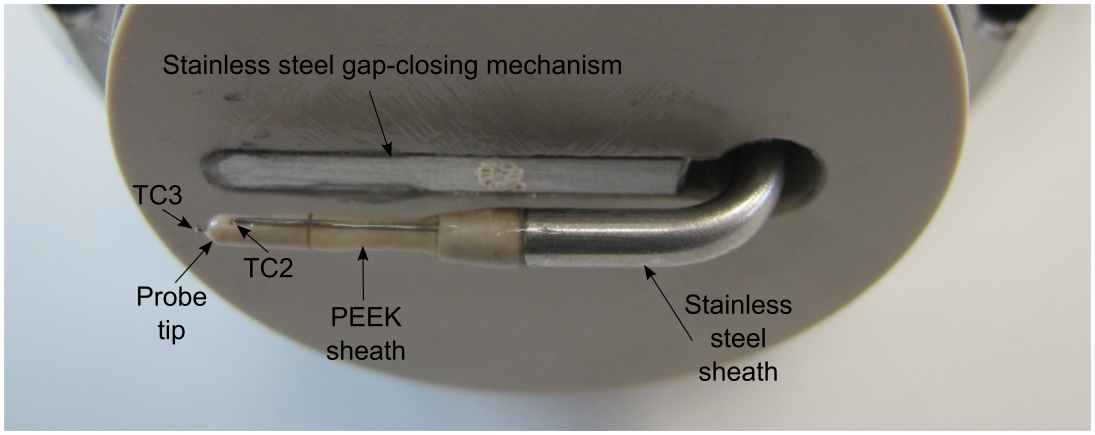


Figure 3.6: Photograph of the probe in its housing as it has been mounted to the BFS test section. The PEEK housing contact surface is coplanar to the test section top wall and corresponds to the reference coordinate system $y-$axis origin, see Fig. 2.1.

corresponding to the potential due to induced electromotive force the $V_{emf}$; $S_{SS}$ the Seebeck-coefficient of stainless steel (i.e. the thermocouple sheaths); $T_1$ and $T_2$ the temperature of the liquid metal at points 1 and 2; $T_{amb}$ is the ambient temperature of the thermocouple connectors outside of the test section where the potential $V_{SS}$ is measured and $S_{e,tip}$ is the effective Seebeck-coefficient of the probe tip. $T_{amb}$ is assumed to be equal for both thermocouple connectors.

Rearranging Eq. (3.3) yields

$$V_{SS} = Ku_{vol} + (S_{SS} - S_{GaInSn})(T_2 - T_1) + V_0 = Ku_{vol} + S_e(T_2 - T_1) + V_0 \qquad (3.4)$$

where $S_e = S_{SS} - S_{e,tip}$ can be interpreted as an effective Seebeck-coefficient for the probe and the thermocouple sheaths.

Thus, the local volume averaged velocity of the fluid $u_{vol}$ is acquired by measuring the induced voltage $V_{SS}$, obtaining the probe sensitivity $K$ by calibration and measuring the temperatures $T_1$ and $T_2$ across the probe for correcting for any superimposed thermo-electric effects.

### 3.4.3 Considerations when designing the probe

There are a few a priori considerations that need to be taken into account to design the probe. These are described in detail in Schaub *et al.* (2021) and are based in the results of Kapulla (2000).

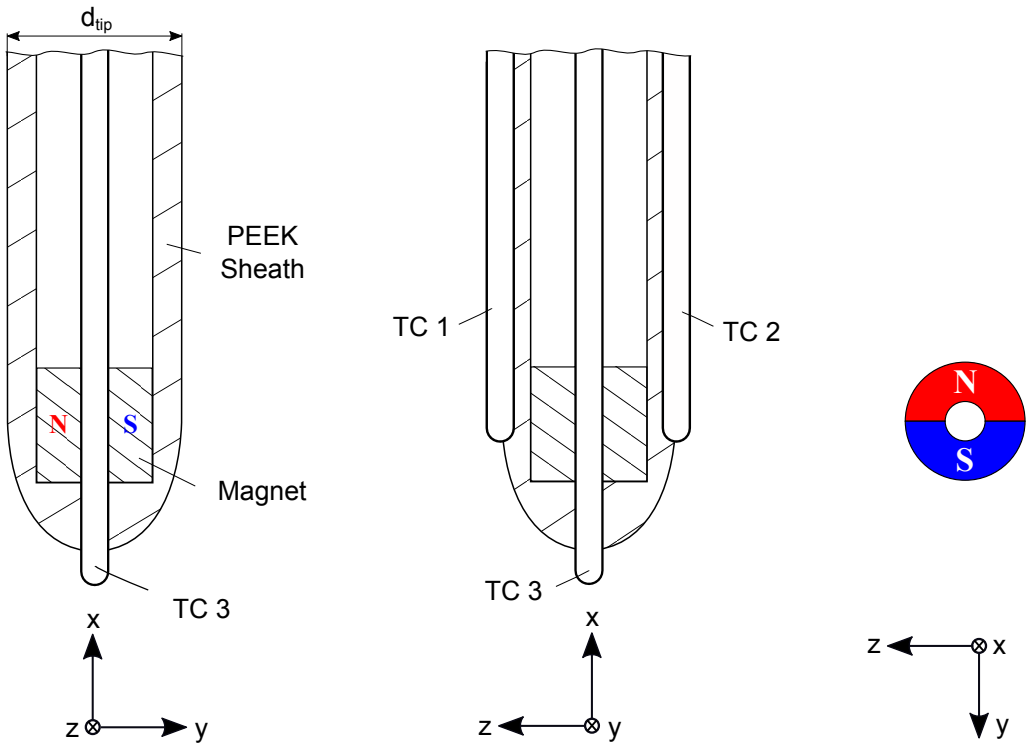


Figure 3.7: Sketches of probe tip and its components (approximately to scale). Left: probe mid-plane cut in the XY-plane, i.e. same orientation as in 3.5. Center: mid-plane cut of the probe (ZX plane). Right: sketch of the permanent magnet front view (ZY plane). The probe tip and its components dimensions are: probe tip outer diameter $d_{tip} = 1.6\,mm$; thermocouple (TC) diameter $d_{TC} = 0.25\,mm$; permanent magnet diameter $d_m = 1\,mm$; permanent magnet length $l_m = 1\,mm$. $TC3$ points out of the probe tip $\sim 0.5\,mm$. The distance between the tips of $TC1$ or $TC2$ and $TC3$ is $\sim 1.5\,mm$.

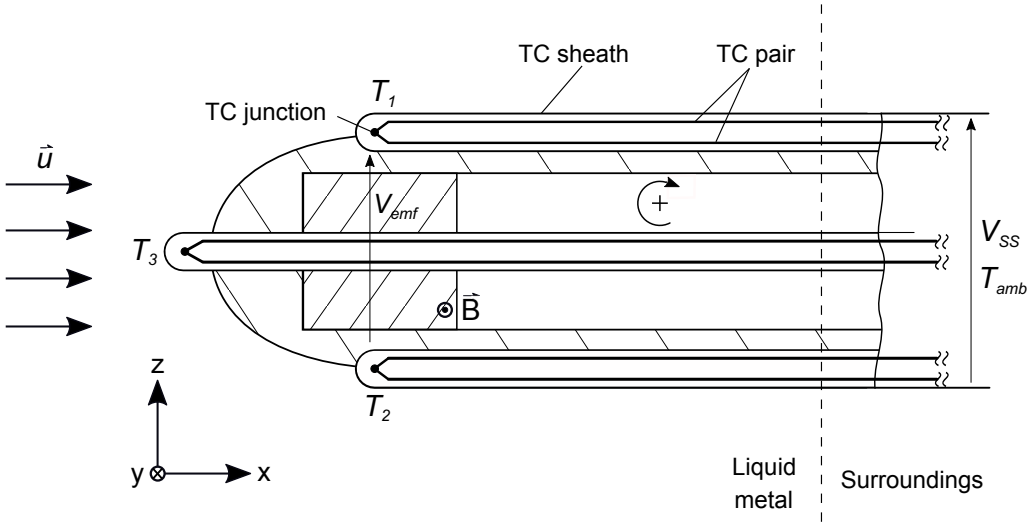


Figure 3.8: Sketch of the tip of the PMP.

**Theoretical estimation of the probe sensitivity**

The theoretical probe sensitivity $K_{th}$ is calculated as $K_{th} = 51\ (\mu V/m/s)$. The equation to calculate $K_{th}$ is based on several assumptions, hence its result is either to be understood in an order of magnitude sense. As will be shown later, the estimate for $K_{th}$ agrees well with the measured sensitivities in the calibration campaign. Taking $K_{th}$ together with the estimated velocity range of the experiment, the effective induced voltages can be calculated being of the order of $\mathcal{O}\left(10^0\right) \lesssim V_{SS} \lesssim \mathcal{O}(10^1)\,\mu V$ for mean *DC* values.

**Deviation of the probe sensitivity from linearity**

The probe sensitivity is assumed linear. As is shown later by observing the measured sensitivities, this is a good approximation. However, under certain circumstances, non-linear effects may affect the probe signal, such as MHD-effects coupled to effects associated with the growing velocity boundary layer around the probe tip. Furthermore, the velocity boundary layer may contribute to non-linear effects by itself.

**Possible MHD effects** The influence of non-linear effects due to MHD effects can be estimated by means of two dimensionless numbers. First, the magnetic Reynolds number

$$Re_m = \mu_s \sigma U_c l_c, \tag{3.5}$$

where $\mu_s$ is the permeability of free space; $\sigma$ the electrical conductivity of the fluid, $u_c$ the characteristic velocity and $l_c$ the characteristic length of interest of the liquid metal flow. Second, the interaction parameter

$$N = \frac{\sigma \bar{B}_0^2 l_c}{\rho U_c}, \tag{3.6}$$

where $\bar{B}_0$ is the volume average of the magnetic field density around the probe tip and $\rho$ the fluid density.

For the present probe $Re_m \approx 0.006$ and $N \approx 0.051$, i.e. for the parameter and velocity range in this experiment, non-linear effects are neglected. Non-linear effects can be expected for this probe for flow velocities below $0.83\,{}^{mm}/_{s}$. In fact, Cramer *et al.* (2006) measured the threshold for non-linear effects in a similar probe to be $< 1\,{}^{mm}/_{s}$ in a flow driven by a rotating magnetic field.

**Possible viscous effects** Depending on the thickness of the viscous boundary layer around the probe tip, non-linear effects can also be expected. As for the covered range in this experiment, a linear sensitivity curve is assumed, as shown in section 3.4.7.

### Thermo-electric effects (inside and outside of the facility)

**Inside of the facility** When using permanent magnet probes in non-isothermal experiments, thermo-electric effects need to be compensated and/or corrected, since these may be in the same order of magnitude as the signal of interest.

Assuming that a thermal gradient exists over the probe tip and that the probe electrodes are not only electrically connected over the liquid metal, but also over the electrically conducting probe sheath and permanent magnet, thermo-electric voltages are induced along the probe tip. These induced thermo-electric Seebeck-voltages can be treated as an effective probe tip Seebeck-coefficient $S_{e,tip}$. However, if all probe tip components are electrically insulated from each other, $S_{e,tip}$ can be taken as $S_{e,tip} = S_{GaInSn}$, i.e. equal in value as the Seebeck-coefficient of the liquid metal. Thus, in Eq. (3.4) $S_e$ is determined only by material properties. Contrary, if the probe tip components are *not* electrically insulated from each other, $S_e$ needs to be determined by calibration.

Further non negligible and measurable thermo-electric effects may also be induced in the liquid metal by macro thermal gradients along the test section, see Kapulla *et al.* (2000). These are neglected in this experiment by placing the probe wires or thermocouples perpendicularly to the thermal gradients and further considering that the thermal gradients are small due to the good thermal conductivity of *GaInSn* and the relatively low heated plate heat transfer rate.

**Outside of the facility** Also all external thermo-electric effects potentially influencing the signal outside of the test section need to be considered. These are reduced to a minimum by enclosing the thermocouple connectors of each probe within an aluminum housing box which in turn is thermally insulated. Furthermore, the used thermocouples are thermally insulated along their extension to avoid locally induced voltages across temperature gradients, see Fenton (1980) and Bentley (1998).

### Thermo-magnetic effects

Among the different thermo-magnetic effects, only the Nerst-Ettingshausen plays a role for this type of probe, see Kapulla (2000). The relation of the Nerst-Ettingshausen thermo-magnetic potential has the form $V_{th,magn} \propto \nabla T \times \vec{B}$. Thus, orienting the magnetic field $\vec{B}$ parallel to the thermal gradients, this effect is eliminated. Since wall normal temperature gradients in this experiment are substantially larger than those in streamwise direction, this effect can be neglected to the leading order.

### Probe orientation and its influence on the flow

From $\vec{J} = \sigma\left(\vec{E} + \vec{u} \times \vec{B}\right)$ it becomes evident that there exists a directional dependency on the induced signal intensity with respect to the angular probe orientation with respect to the flow. In this case, any angular orientation deviation of the probe tip is included in the calibration constant $K$.

The ratio between the displacement area of the probe tip and the inlet cross section area is $0.063\%$ and for the outlet cross section $0.031\%$. The distance between the probe tip and the stainless steel shaft is $30\,mm = 18.75 d_{tip}$. The influence of the probe tip on the flow is thus assumed to be negligible.

### Time lag for velocity fluctuations

By Eq. (3.4), the value of the the instant velocity is directly related to the dynamic response of thermocouples $TC1$ and $TC2$. Kapulla (2000) presents strategies on how to account for these issues. For the measurement of velocity fluctuations a synchronous measurement of $V_{SS}$, $T_1$ and $T_2$ in Eq. (3.4) is hence mandatory. In the present case, due to time and minor technical constraints of the project, the study of velocity fluctuations has been not done. The technical constraints are discussed in section 3.4.5.

### Wetting issues

The main drawback when working with *GaInSn* is the issue regarding its high surface tension, i.e. the wetting of surfaces and small objects or gaps. For a permanent magnet probe to work optimally, we observed that the probe tip needs to be wetted in a *hydrodynamical* and an *electrical* sense.

**"Hydrodynamic" wetting** Hydrodyanmic in the sense that the probe tip must be mechanically wetted, i.e. *GaInSn* must be mechanically rubbed onto the probe tip surface. This reduces the probability of gas pockets to get trapped around the probe tip when it is submerged into the liquid metal. At the same time, this allows a viscous boundary layer to grow around the probe, reducing the flow displacement thickness. This positively affects the probe sensitivity and its stability over time

**"Electrical" wetting** Electrically in the sense that the electrical connection between the three electrodes must be "good enough". This means that an electrical connection between the electrodes per se is not sufficient, but that the electrical resistance between the electrodes must be below a certain threshold. If the electrodes are only partially electrically connected, i.e. an electrical resistance $R$ between the electrodes of order $R > O\left(10^2\right)$ is established, the external electromagnetic shielding effectiveness is reduced because the shield potential is no longer tightly connected to the potential of the liquid metal. Furthermore, inductive/capacitive coupling between the electrodes cannot be neglected. In the case of poor connection between the electrodes, a large constant DC voltage offset of $\sim \mathscr{O}\left(10^0\right)\ mV)$ is observed in the the signal. This DC offset shift is believed to be caused by electromagnetic interferences signals tending to get rectified within the sensitive frontends of the used measurement system (to be introduced in section 3.4.5). The electri-

cal connection between the sheaths has been assessed by measuring the electric resistance between the electrodes. Interestingly, after once accidentally leaving the multimeter connected to a probe for a few minutes, the electric resistance of the probe circuit has been observed to drop from a few mega-ohms to $\sim 35\,\Omega$. This phenomenon could be reproduced with all probes. By connecting probe electrodes with a regular $9\,V$ battery for a few seconds the process could be enhanced and accelerated. The method of wetting an electrically conducting surface with a liquid metal by applying an external voltage between the fluid and the surface is called electro-wetting, see Eaker & Dickey (2016).

### 3.4.4 Probes used in the past

#### Past probe developments

A general summary of the probes used in the past is shown in Table 3.4. PMP developed in the past are similar in design but varied in the used number of thermocouples and the thermocouple junction type. Depending on these differences, more or less complex calibration routines and velocity signal temperature correction methods need to be implemented. Also, the type of flow to be analyzed plays a role in the detail design of the probes. The first probe has been developed by von Weissenfluh (1985) and has been used in a sodium vertical pipe flow, while von Weissenfluh & Sigg (1987) further developed their probe and applied it to a rod bundle flow. Knebel *et al.* (1998) used a different probe concept in a sodium vertical confined jet flow. Kapulla (2000) adapted their probe concept for a sodium horizontal mixing layer experiment. All these experiments have been of course non-isothermal. Up to the best knowledge of the author, there are no further PMP developments with thermocouples as electrodes available in the open literature.

#### Advantages and disadvantages of the present probe design in comparison with those used in the past

The working fluid plays a major role in the probe design. Since *GaInSn* is used as the working fluid, PEEK can be used for the probe tip material, which is an electric insulator. The electric insulation of the probe tip component has the major advantage that the probe effective Seebeck coefficient $S_e$ has not to be determined by calibration. For higher temperatures and for liquid sodium, ceramic materials can also be used, see von Weissenfluh & Sigg (1987).

Another advantage of our probe design is the separation of the treatment of the temperature and velocity signal by using ungrounded thermocouples and by measuring the velocity proportional signal over the thermocouple sheath. All probes in the past used grounded thermocouples, i.e. the velocity proportional signal has been measured over the thermocouple pair. In other words, the velocity-proportional signal is superimposed on the temperature signal when using the grounded thermocouple approach. Hence, corrections and/or compensations for both temperature and velocity signals are needed. Alternatively, three-wire thermocouples can be used as well to achieve the same objective as ours of treating both signals separately.

Along the disadvantages of our approach we mention the lower frequency response for the temperature signal when using ungrounded thermocouples. This can be compensated by using thinner thermocouples, but we preferred to stick to thicker thermocouples since extremely thin thermocouples tend to break very easily (during the calibration campaign, the probes have been mounted and unmounted several times – hence we opted to use more robust thermocouples).

An advantage of past probes compared to the present development is that probes used in the past placed the thermocouples on the permanent magnet surface. As a consequence, higher probe sensitivities are theoretically possible. We compensated this effect by using stronger magnets than those used in the past, see Table 3.4.

### 3.4.5 Signal and data processing

A sketch of of the data-flow diagram is shown in Fig. 3.9.

#### Temperature signal DAQ

The probe temperature signals $V_{TC_i}$ and the temperature signals $T_{w,iA/C/E}$ corresponding to the heated plate columns $A$, $C$ and $E$ are induced between the respective thermocouple hot junction and a ISOTECH TRU 937 cold junction at $0°C$. The signals are digitized through NATIONAL INSTRUMENTS NI9213 thermocouple modules connected to a CDAQ-XT chassis. The heated plate temperature signals $T_{w,iB/D}$ of columns $B$ and $D$ are directly measured in the NI9213 modules. NI9213 modules have 16 channels and a maximum sampling rate of 75 samples per second *per module*, i.e. a sample rate *per channel* of $75/16 \sim 4.69\,Hz$.

Table 3.4: Geometrical and operational characteristics of selected PMP found in the literature.

| | von Weissenfluh (1984), von Weissenfluh (1985) | von Weissenfluh & Sigg (1987) | Knebel & Krebs (1993), Knebel *et al.* (1998) | Kapulla *et al.* (2000), Kapulla (2000) | This work |
|---|---|---|---|---|---|
| Experiment / liquid metal | Vertical pipe flow / *Na* | Rod bundle flow / *Na* | Confined vertical jet & plume in a co-flow / *Na* | Confined horizontal plane mixing layer flow / *Na* | Confined vertical backward facing step / *GaInSn* |
| Temperature range $[^{\circ}C]$ | $200-250$ | $<450$ | $300-375$ | $230-300$ | $25-32$ |
| Probe outer diameter $[mm]$ / probe material | 1.5 & 1.3 / Stainless steel | 3.5 & 8.6 / Stainless steel | 2.5 / Stainless steel | 2.5 / Stainless steel | 1.6 / PEEK |
| Magnet type / Remanence $T$ $[Vs/m^2]$ | RECOMA / 1000 | AlNiCo (n.a.) / n.a. | AlNiCo 450 / n.a. | AlNiCo 450 / $1000-2000$ | NdFeB / 10000 |
| Used number of thermocouples | 2 & 4 | 2 | 3 | 3 | 3 |
| Thermocouple and junction type | Type K, 2 wired, open | Type K, 3 wired, ungrounded | Type K, 3 wired, grounded | Type K, 2 wired, grounded | Type K, 2 wired, ungrounded |
| Thermocouple diameter $[mm]$ | 0.25 | 0.5 | 0.25 | 0.5 with reduced tips to 0.27 | 0.25 |
| Calibration method | in situ; *Re*-correlation, flow meter comparison | in situ; flow meter comparison | in situ; flow meter comparison | in situ; flow meter comparison | ex situ; flow meter comparison |
| Probe sensitivity $K$ $[\mu V/m/s]$ | 30 | $70-122$ | 47 | $67-80$ | $30-55$ |
| Temperature compensation method type for $V_{SS}$ | Static | Static | Static | Dynamic correlation analysis | Static |

**Velocity signal DAQ**

The main challenge has been to identify a commercially available measurement system capable of reaching the limit of what is technically possible. The chosen measurement system is an LTT24 from LABORTECHNIK TASLER GMBH with an included LINEAR TECHNOLOGY LT6018 operational amplifier. The probe signal $V_{SS}$ enters the differential ended mode channel with a range of $\pm 5\,mV$. For this particular task, the standard LTT24 differential amplification stage $(20:1)$ is preceded by a further amplification stage $(50:1)$ with an LT6018 operational amplifier (soldered into the LTT24 system). The amplified signal is digitized immediately with a $24\,bit$ A/D converter which oversamples the signal with $32\,MHz$. The digital signal is fed into a noise-shaping routine and is finally transferred at a decimation at rate of $5\,kHz$ to the PC. Finally, the signal is digitally low-pass filtered with an 8-pole Butterworth filter at $200\,Hz$ for mean velocity measurements and at $500\,Hz$ for time-resolved signal measurements.

A rough estimation of the noise level due to intrinsic physical phenomena of any measurement system can be found in the appendix of Schaub *et al.* (2021). The calculations for the measurement system alone (i.e. without plugging the probe to the LTT24) indicate that achieved noise level has been below the mentioned theoretical worst-case threshold for thermal- and flicker noise contributions. When plugging the probe to the LTT24, the external electromagnetic interferences have been suppressed down to $\sim 80\,nV$ (representative estimate for all channels and probes).

### 3.4.6 Required measurement synchronization, sampling time and sampling rate

**Needed data acquisition synchronization for the measurement of velocity fluctuations**

By Eq. (3.4), the measurement of the instant flow local velocity $u_{vol}(t)$ requires also the measurement of the instant temperatures $T_1(t)$ and $T_2(t)$. To correct the flow velocity fluctuations $u'$ measurement a synchronous measurement of $T_1'$ and $T_2'$ together with $u'$ is mandatory. Thus, the NI9213 temperature modules needs to log data synchronized to the LTT24 measurement system. Since both data acquisition systems are controlled by separate software packages (LABVIEW for the NI9213 modules and LTTPRO for the LTT24 system), the synchronization of both systems is not a trivial task. Due to time constraints, this could not be solved within this

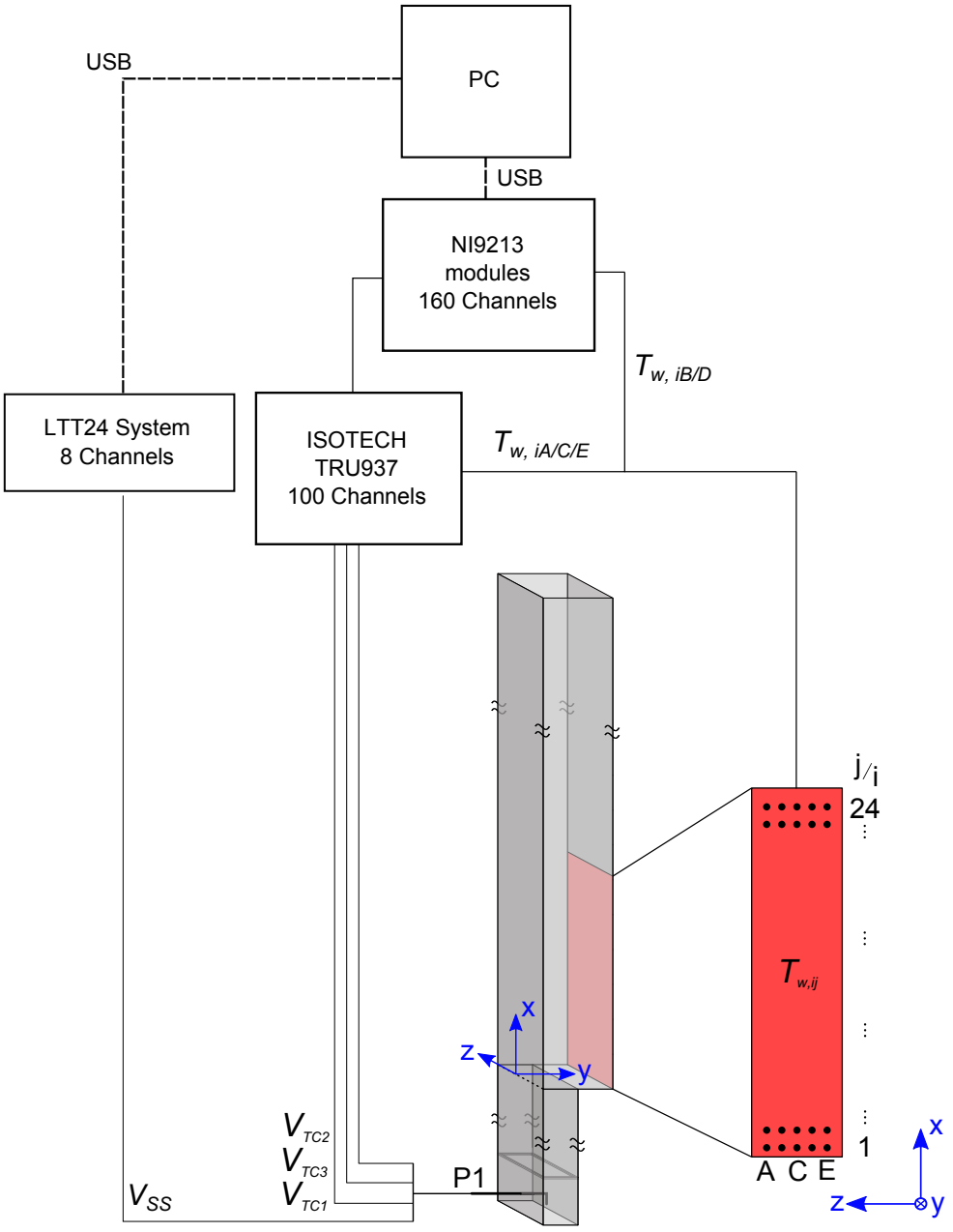


Figure 3.9: Data flow diagram.

study.

#### Defining sampling times and rates

The sampling time per measurement point and the respective sampling frequency has been determined based on the statistical analysis presented by Tropea *et al.* (2007) considering additionally the optimum operation of the LTT24 measurement system.

The chosen sampling time $t_s$ for the PMP per measurement point in the flow has been chosen to $t_s = 105\,s$ for the BFS profile measurements and $t_s = 52.43\,s$ for the calibration of the probes. The data have been decimated at a decimation rate (equivalent to an analog sampling frequency) of $f_d = 5000\,Hz$ and using a 8-pole Butterworth low-pass filter with cut-off frequency $f_c = 200\,Hz$. Of course, for the measurement of mean quantities, a much lower sampling frequency is sufficient. However, as already mentioned, an optimum operation of the LTT24 measurement system had to be guaranteed, hence a higher decimation rate has been chosen than actually needed. The chosen cut-off frequency $f_c$ is calculated taking the probe diameter $d_{tip} = 1.6\,mm$ and assuming the maximum inlet bulk velocity for the measurement campaign of $U_b = 0.247\,m/s$, yielding a probe frequency cutoff is$f_{tip} = 154\,Hz$.

### 3.4.7 Probe calibration

#### Calibration procedure

By the calibration task consists the measured voltage $V_{SS}$ is related to an actual velocity $u$ at isothermal conditions. An in-situ calibration for PMP is always preferred, because the measurement uncertainty of the measured probe sensitivity $K$ can be reduced. Unfortunately, due to the geometry of this particular experiment, an in situ calibration is not feasible. Hence, all probes have been sequentially mounted and calibrated at the test section inlet corresponding to $P1$ in Fig. 3.9 or 3.1). Taking the measured flow rate and the inlet channel dimensions, a inlet bulk velocity $U_b$ is calculated.

The probes have been sequentially calibrated in the order: $P2$, $P3$, $P4$, $P5$, $P6$ and $P1$ following a systematic procedure:

i. Each probe has been prepared for calibration, i.e. cleaned and mechanically wetted.

ii. The probe to be calibrated has been mounted the test section at position $P1$ and positioned at the channel center.

iii. The facility has been filled with *GaInSn* and the electrical resistance between all three electrodes has been checked to be $R < 35\,\Omega$. If this had not been the case, electro-wetting has been applied.

iv. The signal $V_{SS}$ has been measured for a time period $t_s$ under ambient electromagnetic interference with the pump variable frequency drive once turned off and then on.

v. The pump has been set at a rotational frequency $\omega = 10\,rpm$ and the flow has been let to stabilize. The signal $V_{SS}$ has been measured for a period of time $t_s$.

vi. $\omega$ has been increased in $10\,rpm$ steps until reaching $200\,rpm$. This is called a "run up". Then $\omega$ has been decreased back, again every $10\,rpm$. This is called a "run down". For each point $V_{SS}$ has been measured for a period of time $t_s = 52.43\,s$.

vii. The facility has been drained and then filled again. Steps 2 to 6 have been repeated two further times for each probe, i.e. six calibration curves have been obtained for every probe.

viii. The probe has been demounted from position $P1$ and mounted into its final position.

The reason for measuring several "runs" or calibration curves for each probe is to assess the calibration repeatability in terms of wetting quality of the probe tip. This, to exclude potential calibration curve transfer issues when demounting and mounting the probe from the calibration point to the actual measuring position. For every "run" the measurement chain has been thermally stabilized for at least 12 hours to exclude potential thermal drifts during the measurement campaign. The offset has been measured before and after all runs. In both measurements for all probes the offset may have varied during the calibration $\pm 0.060\,\mu V$.

**Results of the probe calibration**

The measured probe sensitivities $K$ together with their extended experimental uncertainty $2u_{\overline{K}}$, i.e. for a confidence interval of 95.45%, are shown in Table 3.5. The

Table 3.5: Measured probe sensitivities $K$ and evaluated experimental extended uncertainties $2u_{\overline{K}}$(confidence interval 95.45%).

| | $K$ $[\mu V/m/s]$ | $2u_{\overline{K}}$ $[\mu V/m/s]$ |
|---|---|---|
| $P1$ - All runs | 52.41 | 1.72 |
| $P2$ - All runs | 50.85 | 1.16 |
| $P3$ - All runs | 41.95 | 6.42 |
| $P3$ - $3^{rd}$ run only | 46.83 | – |
| $P4$ - All runs | 23.18 | 8.50 |
| $P5$ - All runs | 43.97 | 2.91 |
| $P5$ - $3^{rd}$ run only | 45.78 | – |
| $P6$ - All runs | 54.82 | 3.99 |
| $P6$ - $3^{rd}$ run only | 57.62 | – |

uncertainty analysis is presented in detail in appendix E. For each probe, a total of six calibration curves have been recorded.

**Probes $P1$ and $P2$** The calibration results for probes $P1$ and $P2$ are shown in Fig. 3.10 and both show very similar results. Their measured sensitivities agree well with the theoretically predicted estimate of $K_{th} = 51\,\mu V/m/s$. No major difference in the probe sensitivity is observed between runs (slope of the curve), which also indicates a robust wetting of the probe tip and between the electrodes of the probe. Both probes have been mounted to the test section during the commissioning of the facility and the measurement chain. For these two probes, no electro-wetting had been needed for the probes to properly work, even when the test section has been empty, both probes remained wetted.

Probe $P2$ has been the first probe to be calibrated in the calibration campaign, while probe $P1$ has been the last one. $P1$ has been electro-wetted for its first run alone since by that point of the campaign, we have had realized this effect. One can observe the minor decrease of its sensitivity along runs. This means that electro-wetting cannot be expected to hold its positive effect between facility draining and filling procedures.

**Probes $P3$, $P5$ and $P6$** These probes exhibit a similar behavior during the calibration campaign and are shown in Fig. 3.11 and 3.12. The measured sensitivities

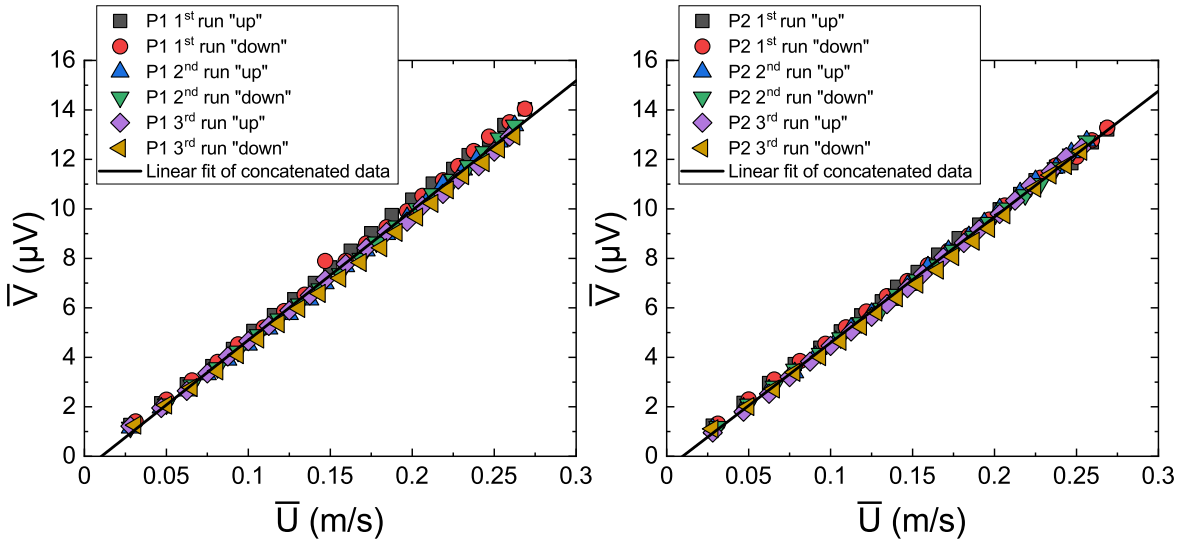


Figure 3.10: Measured sensitivity curves for probes $P1$ and $P2$.

correspond to those theoretically predicted (in an order of magnitude sense). For these probes an increasing sensitivity is observed during the calibration campaign. The black linear fit curve corresponds to the concatenated linear fit for all data points, whereas the red line corresponds to concatenated linear fit for the third run (both “up” and “down”).

For probes $P3$ and $P5$, which have been only wetted mechanically, a constant sensitivity increase is observed between single runs, indicating that probes mechanically wetted eventually reach their asymptotic sensitivity with time. However, it must be noted compared to electro-wetting, this time is large. The probes had to be demounted, mechanically re-wetted and mounted again several times before they recovered their functionality capability to the expected degree.

During the calibration of probe $P6$ electro-wetting and its positive effect on the probe sesitivity had been recognized. Therefore, it has been wetted both mechanically and by electro-wetting. Nevertheless, the sensitivity of the second run is lower than that of the other two runs. A possible reason is that for this probe, electro-wetting has been executed only prior to the first run only, i.e. for this run the sensitivity can be expected to be at its maximum due to optimum wetting. After draining and filling again the facility for the second and third runs, the probe has not been wetted again by electro-wetting. This means that the sensitivity increase from the second to the third run may be explained by regular mechanical flow-wetting.

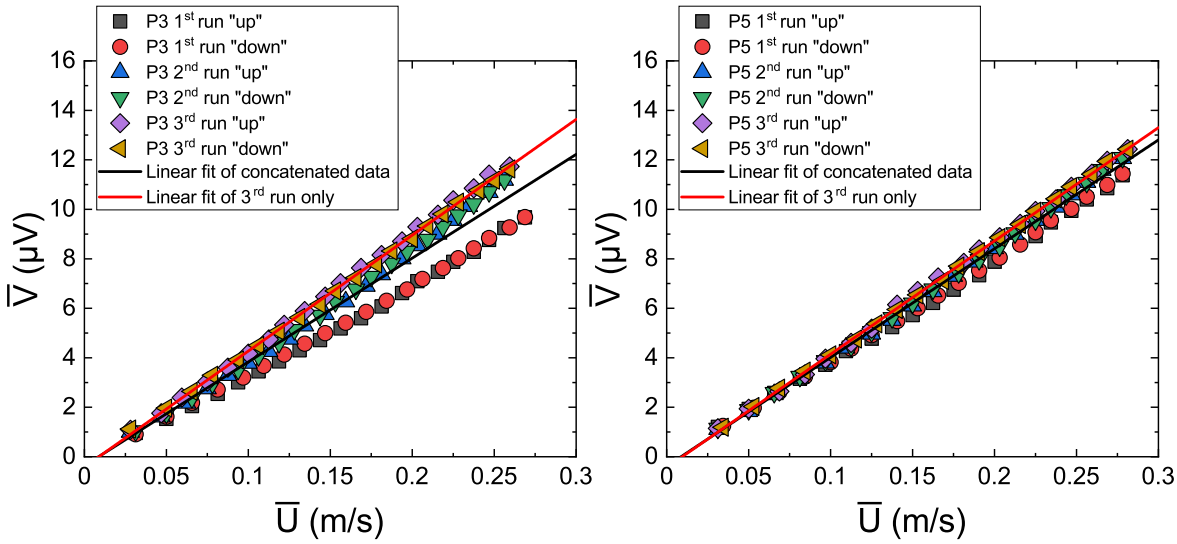


Figure 3.11: Measured sensitivity curves for probes *P*3 and *P*5.

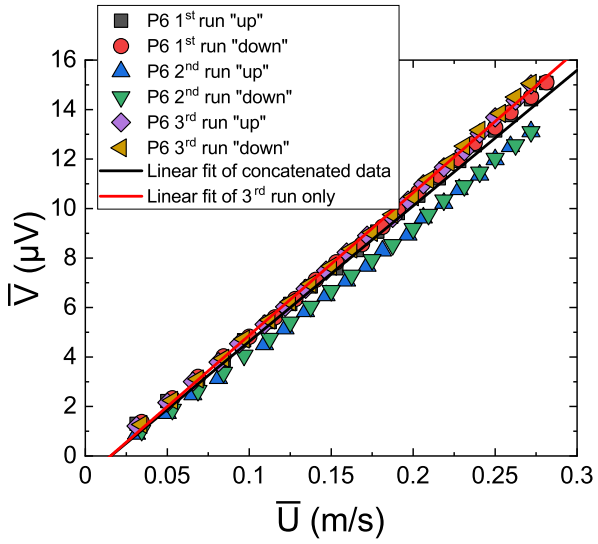


Figure 3.12: Measured sensitivity curves for probe *P*6.

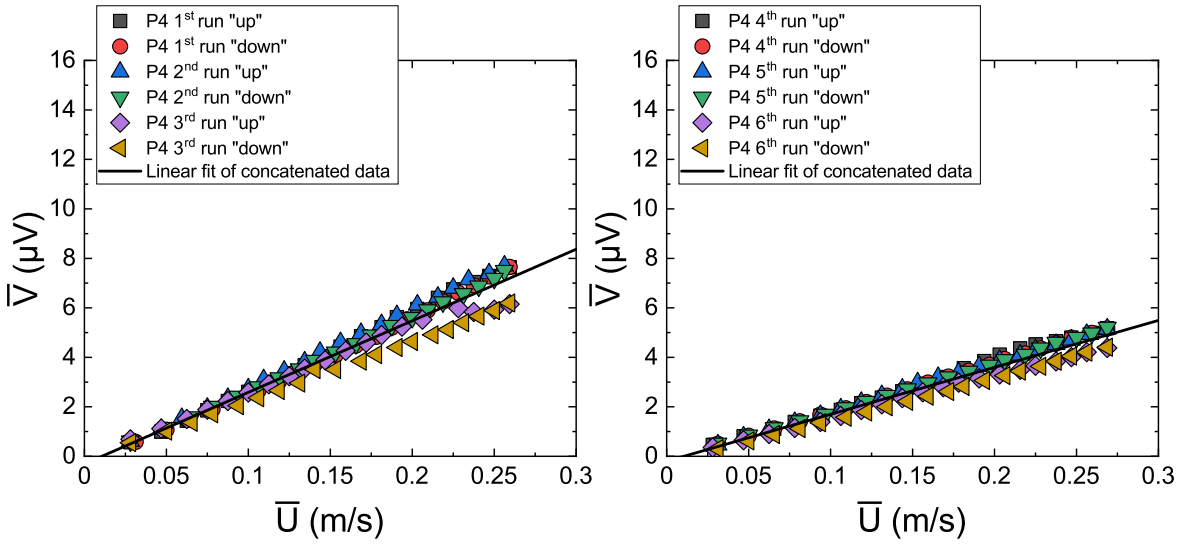


Figure 3.13: Sensitivity curves for probe $P4$

**Probe** $P4$ This probe exhibits the lowest measured sensitivity and reveals an atypical behavior. Taking a closer look to Fig. 3.13 one can observe that the probe sensitivity declines after every drain procedure of the facility. In fact, during the "third run up" one can observe that the probe suffers a sudden sensitivity decline during the calibration campaign. After noticing this behavior during the experiments, the probe has been demounted and re-wetted. The results for this probe after being re-mounted correspond to runs 4 to 5. The behavior for a decreasing sensitivity can still be observed, however, the deviations between the runs is lower. Since there is no way to know a priori for the actual experimental campaign which sensitivity can be used for this probe, it has been decided to take the slope of the concatenated linear fit for the full data set with the penalization of a high standard uncertainty for the sensitivity value. This means that the experimental uncertainty for the results measured for $P4$ are the highest.

**General comments for all probes** For all probes the intersection of the linear fits with the ordinate axis is negative. This is not physically possible since all sensitivity curves have been offset-corrected within $\pm 60\,nV$ before calibration and checked afterwards ($V_0$ in Eq. (3.4)). A possible explanation for this effect is that below a certain velocity, non-linear effects appear when the fluid velocity in the surroundings of the probe passes below a certain threshold. As mentioned in section 3.4.3, the non-linear threshold should be $U_c < 0.83\,{}^{mm}/_{s}$.

To ensure experiment conformity, a post-calibration of all probes after the actual

backward facing step measurement campaign should have been performed. However, due to time constraints, this has been not possible but remains an important task to be done to further assess the quality of the present results.

A further contribution to the good behavior of probes $P1$ and $P2$ may have had to do with the cleaning procedure for these two probes. Heptane has been used as a cleaning medium for these two probes. However, due to safety concerns of the safety authorities regarding the use and the disposal of heptane on a daily basis, isopropanol has been used instead for the rest of the probes. Whether this may have had an influence or not, is unclear.

Finally, the question which sensitivity for the calculation of the flow velocities in the actual experiment must be addressed. The question is whether the sensitivity coefficient for the full data set is to be used or if only the data, e.g. for a third run only should be considered. This has a major influence in the uncertainty estimation (see in the appendix E). It is important to mention that for the actual experimental campaign the facility has not been drained during the measurement campaign. Furthermore, before beginning the measurement campaign, every probe has been electro-wetted up to a point to achieve an electrode resistance below $35\,\Omega$. Hence, it is assumed that probes $P3$, $P5$ and $P6$ exhibit a behavior similar to that of probes $P1$ and $P2$ after hours of operation. By the chosen approach, which may be considered over-conservative, the full data set for each probe is used for both the calculation of the sensitivity and the uncertainty analysis.

## 3.5 Analysis of the experiment boundary conditions

### 3.5.1 Inlet and outlet

The BFS flow is sensitive to its boundary conditions (Nadge & Govardhan (2014), Tihon *et al.* (2010)). The ideal scenario is to place the BFS inlet and outlet as far away as possible from the region of interest, i.e. the recirculating region downstream of after the step. On the one hand this facilitates the comparison of the experimental results with numerical calculations, since the generation of a simulated fully developed turbulent inlet profile is straightforward. On the other hand, due to the elliptic nature of pressure fields (Pope (2000), Davidson (2015)), any disturbance near the test section outlet will be felt by the upstream flow. By placing the outlet as far away as possible, these disturbances can be reduced to a minimum. However, due to the limited available amount of liquid metal, a compromise is made

regarding the extension of the inlet and the outlet sections. Inlet disturbances are managed by means of flow conditioning techniques (perforated plates, screens, honeycombs), while any outlet disturbances are dissipated by placing the outlet as far away as possible. The test section dimensions are shown in Fig. 3.2, where all dimensions are scaled by the step height.

A constant velocity profile is required at the test section inlet to calibrate the permanent magnet probes. The measured inlet velocity profiles at three different $Re_h$ are shown in Fig. 3.14. The red band denotes a uncertainty band of 5%. The velocity profiles have been measured on different days to test the long term stability of the facility. The values for $Re_h = 20000$ and 30000 lie above unity, although the probes for measuring the profiles have been actually calibrated at this position for these velocities. This is explained by the general repeatability effects of the facility and improved wetting effects of the probes at higher velocities, since the viscous boundary layer around the probe tip becomes thinner as the volume averaged velocity around the probe tip increases, see Schaub *et al.* (2021).

A velocity profile tilt of $\sim 2.5\%$ is observed towards the low values of $y$ in Fig. 3.14. Looking at Fig. 3.1, it appears that the influence of the 90° bend with vanes is not fully corrected by the three grid stages and the honeycomb in the settling chamber. The settling chamber pressure drop had to be limited due to the relatively low pressure head of the pump. Hence, relatively coarse grids are chosen, i.e. grids with the lowest possible solidity, but guaranteeing a value below the jet coalescence limit (Groth & Johansson (1988)). After commissioning the facility, the pump pressure head has been measured to be higher than indicated in the data sheet. This is most likely due to the poor wetting of *GaInSn* along the facility (not the test section), although some issues related to the pump characteristic curve provided by the manufacturer cannot be totally excluded. In the future, screens with a higher pressure drop along the flow conditioning section could be installed. This should guarantee a more uniform inlet profile at the test section.

The turbulence intensity $Tu$ at position $P1$ (Fig. 3.1) is estimated to be 1%, see Schaub *et al.* (2021). $Tu$ is defined in the appendix C and gives a quantiative measure of the relative velocity fluctuation level compared to the local time averaged mean velocity. $Tu$ had to be estimated for $P1$ since the velocity fluctuation signal at the test section inlet dissapeared in the signal noise. The flow integral time scale $t_{int}$ has been estimated by assuming a worst-case scenario, i.e. by calculating $t_{int}$ from the integral length scale $l_{int}$ for a fully developed turbulent flow between two parallel plates assuming the Taylor hypothesis of frozen turbulence, see Bailly

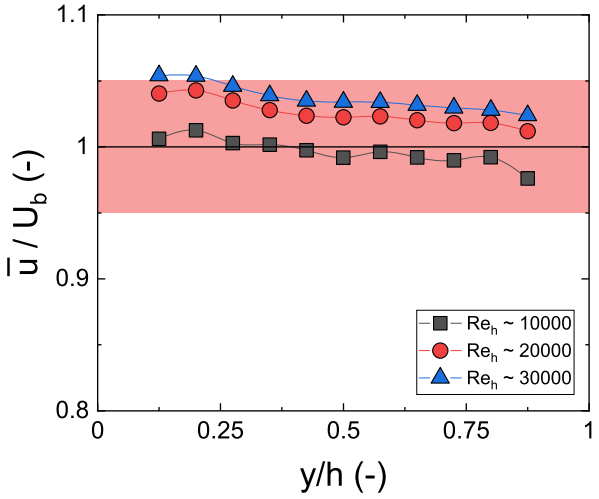


Figure 3.14: Measured dimensionless profiles at three different $Re_h$ of the streamwise velocity component along the test section inlet (probe $P1$ in Fig. 3.1). The red band denotes a 5% uncertainty band.

& Comte-Bellot (2015). As shown in Tropea *et al.* (2007), $t_{int}$ and $Tu$ are needed for the estimation of the statistical uncertainty of the measured mean velocities and for defining the sampling time and sampling frequency during the calibration and measurement campaigns.

At the test section inlet a very thin and eventually relaminarized boundary layer cannot be avoided. A trip wire is placed after the calibration position ($P1$ in Fig. 3.1) to trigger at a single point the boundary layer transition from laminar to turbulent. Because a turbulent boundary layer grows faster than a laminar one, a thicker and hence an easier-to-measure boundary layer is obtained at position $P2$ in Fig. 3.1.

The temporal stability of the temperature inlet boundary condition - the baseline temperature stability of the facility - is given by the interaction between the heat sources and heat sinks of the facility. The result can only be reliably assessed in practice during the commissioning phase of the facility. In Fig. 3.15 the facility *baseline* temperature is measured with $P1$ at the inlet channel center, i.e. at $y/h = 0.5$ and is plotted over time. The red band denotes a period of time of $t = 50s$, which approximately represents the sampling time of one measurement point when measuring a velocity and temperature profile along the test section.

The temporal temperature baseline fluctuation shown in the figure exhibits a peak-to-peak temperature difference of $\sim 0.4°C$, which originates only by the mentioned interaction between the heat sources (heated plate and pump) and the heat

sink (heat exchanger). The peak-to-peak fluctuation level varies depending on heated plate input power. On average, a value of $\sim 0.5°C$ is representative for all measured parameter sets. For the forced convection parameter sets, the baseline temperature variation is the same order of magnitude of the temperature gradients induced in the fluid by the heated plate. Thus flow- and heated plate-induced temperature transversal *gradients* (in the $y-$axis) are not distinguishable from the baseline temperature fluctuation of the loop because each measurement point sampling time is shorter than the baseline temperature fluctuation period. This also holds for turbulence-induced temperature *fluctuations* as they cannot be statistically distinguished in a RMS-sense from the inlet temperature baseline fluctuation. In other words, when measuring velocity and temperature profiles, each measurement point "rides" on top of the baseline temperature fluctuation at a different time as can be seen in Fig. 3.15 if the red band is imagined to move along the time axis.

One alternative to eliminate the inlet temperature baseline variability is to zero average it by taking longer measurements for a full baseline fluctuation period $t_p$ or multiples from it ($t_p \sim 8-15\,min$ depending on the input heat power). This would have to be done for *each* of the 114 measurement points and for *each* parameter set, which is not feasible in practice. Hence, at this stage of the project, although *qualitative trends* are observed in the results for the mean temperature profiles for the forced convection regime, for the rest of the measured profiles, the results *are not* conclusive and hence not shown in this study. However, as will be shown later, the zero-averaging strategy has been successfully implemented for the measurement of the heated plate local temperature, which have been measured for $5t_p$ (in Fig. 3.15 a total of $3t_p$ are shown).

### 3.5.2 Walls

All walls have been mechanically wetted with *GaInSn* by rubbing it to the walls with a sponge-like device made of foamed polystyrene. The result is depicted in Fig. 3.16.

A comparison between pressure drop measurements along the test section and complementary conducted numerical simulations with empirical correlations (Idelchik (2007)) are in good agreement. Hence, the the no-slip boundary condition is assumed. Since the inner walls of the test section channel are manufactured of PEEK and the test section external channel is further insulated with $\sim 40\,mm$ (Armaflex ®), they are considered as adiabatic.

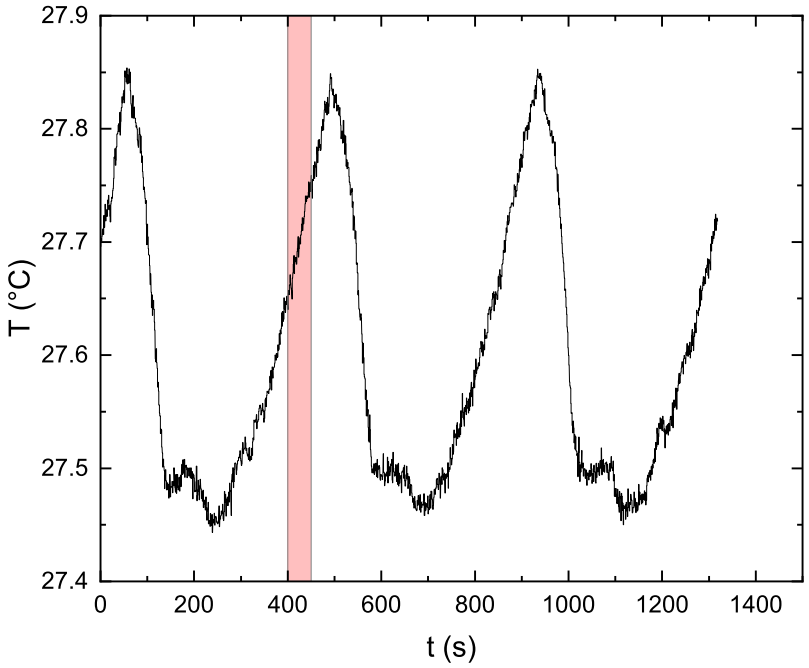


Figure 3.15: Measured facility baseline temperature fluctuation at the test section inlet measured with probe $P1$ in Fig. 3.1 at the inlet channel center, i.e. $y/h = 0.5$ for $Re_h \approx 10000$ and $Ri = 0.15$. The red band denotes a $\sim 50\,s$ time interval corresponding to the sampling time of an exemplary measurement point.

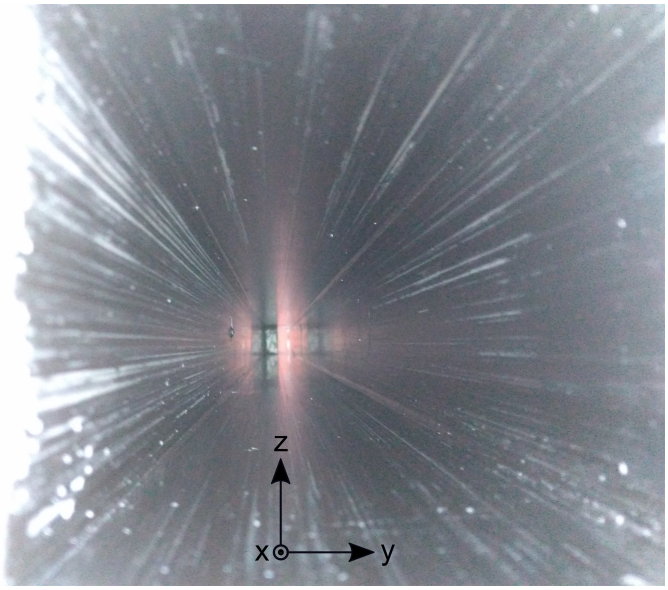


Figure 3.16: Photograph of the mechanically wetted test section, viewed from the outlet into the test section.

The position of the pressure measurement points is not shown in Fig. 3.2. During the facility commissioning, liquid metal leaks have been noticed in the pressure transducers. Hence, the pressure sensors had to be unmounted. As a consequence, pressure drop measurements along the test section have been not performed during the actual measurement campaign.

### 3.5.3 Heated plate

The heated plate consists of two copper blocks, an inner and an outer block having a total thickness of $0.85h$, see Fig. 3.2.

The inner block is mounted into the test section and works as the contact surface to the liquid metal. The inner block has the same wall thickness as the PEEK inner- and stainless steel outer-walls together, i.e. it overlaps both walls. To avoid axial thermal losses to the test section stainless steel outer wall, the inner copper block is thermally insulated over its perimeter with a PEEK frame. The sensing thermocouples are integrated into the inner copper block. The outer copper block acts as the heat source and is pressed onto the inner block. To guarantee a homogeneous thermal contact between both blocks, the outer block is wringed (as done with gauge blocks) and pressed to the inner block. Electrical steel housed resistance heaters are integrated within the outer copper block. The external surface is thermally insulated with a $\sim 100\,mm$ thick high-temperature insulating wool layer, which is housed in

a $\sim 40\,mm$ thick Armaflex ® box. The resistance heaters are embedded in grooves in the heated plate (second block) following a serpentine shape[3].

The heated plate type of thermal boundary condition can be assessed by calculating the heated plate Biot number

$$Bi \equiv \frac{\alpha\, l_c}{\lambda_{HP}}, \tag{3.7}$$

where $\alpha$ is the convective heat transfer coefficient, $\lambda_{HP}$ the thermal conductivity of the heated plate (in this case copper, with $\lambda_{HP} = 401\,W/(K \cdot m)$ and $l_c$ the characteristic length of the heated plate calculated as $l_{HP} = {}^{V_{HP}}/_{A_{HP}}$ , where $V_{HP}$ is the heated plate volume and $A_{HP}$ is the heated plate contact surface to the liquid metal.

The heat transfer coefficient $\alpha$ along the heated plate is defined as

$$\alpha = \frac{\dot{q}}{T_w - T_b}, \tag{3.8}$$

where $\dot{q}$ is the heated plate specific heat flux, $T_w$ the heated plate wall temperature and $T_b$ a case-specific ad hoc bulk temperature, in this case $T_b = T_{inlet}$, where $T_{inlet}$ is the test section inlet temperature.

The Nusselt number is calculated as

$$Nu = \frac{\alpha l_c}{\lambda_{ref}} = \frac{\dot{q} l_c}{\lambda_{ref}\,(T_w - T_b)}, \tag{3.9}$$

where $l_c$ is the characteristic length (in this case the step height), $\lambda_{ref}$ the thermal conductivity of the working fluid at the reference temperature $T_{ref} = 25°C$.

For all measured cases, the estimated Biot number is of order $Bi = \mathscr{O}\left(10^{-1}\right)$. This is an indication that neither a constant heat flux nor a constant temperature thermal boundary condition can be assumed for the heated plate. A mixed type thermal boundary condition is more likely to describe the actual thermal boundary condition of the heated plate. Thus, a local specific heat flux $\dot{q}_{local}$ is to be used to calculate $Nu$ in Eq. (3.9). When calculating $Nu$ assuming either way a constant specific heat flux $\dot{q}_{const}$, $Nu$ can then only be interpreted as a quantity proportional to the reciprocal of the local $\Delta T = T_w - T_b$.

In future experiments, $\dot{q}_{local}$ will be measured or, alternatively, it will be calculated by solving the inverse Fourier problem from local temperature measurements (Woodfield *et al.* (2006)). For the present experimental campaign, $\dot{q}_{const}$ is used to

[3]The idea behind using copper for both blocks is to homogenize the residual thermal trace left by the serpentine-shaped electric heaters.

determine $Nu$ and is calculated as $\dot{q}_{const} = \dot{Q}_{HP}/A_{HP} = V_{DC}I_{DC}/A_{HP}$, where $\dot{Q}_{HP}$ is the thermal power given by the product of $V_{DC}$ and $I_{DC}$, being $V_{DC}$ and $I_{DC}$ the heated wire electrical DC-voltage and current, respectively, and $A_{HP}$ denotes the heated surface area. The effect of assuming $\dot{q}_{const}$ for $\dot{q}$ in Eq. (3.9) instead of $\dot{q}_{local}$ is discussed in section 4.4.

### 3.5.4 In situ calibration of the test section and probe thermocouples

An advantage of liquid metal facilities is that at sufficiently high mass flow rate, a constant fluid temperature can be assumed along a section of the facility, in this case the test section. Under isothermal conditions, taking the maximum possible flow rate of the facility and estimating the thermal losses of the test section, the theoretical fluid temperature is calculated to be constant within $\pm 0.05^{\circ}C$, see Stephan *et al.* (2019). Under these conditions, the thermocouples of all probes and those of the heated plate are calibrated in situ relative to a master thermocouple, which was chosen to be $TC3$ of $P1$, see Fig. 3.1 and 3.8. Relative to this master thermocouple all thermocouples are *precise* within $\pm 0.05^{\circ}C$. This procedure has been repeated for 11 temperature levels covering the entire temperature range for the experiment. Thereby, an average offset value for each thermocouple relative to the master thermocouple is obtained. After the offset-correction of the temperature readings, the thermocouple readings of all thermocouples in the test section are *precise* within $\pm 0.31^{\circ}C$ relative to the master thermocouple (95.45% confidence interval). Between the same master thermocouple and all the heated plate thermocouples, the precision improves to $\pm 0.03^{\circ}C$ (95.45% confidence interval). These worst-case value are *repeatable* on different days. However, the *trueness* of the temperature measurements is still within the typical uncertainty for thermocouples[4] .

### 3.5.5 Energy balance of the facility

The energy balance of the facility is monitored by comparing the electrical heat input versus the temperature difference between the inlet and outlet of the facility

[4]Here, the concepts of *precision, trueness* and *accuracy* are clearly distinguished from each other. The term *accuracy* is a metrology concept *related* to the two quantitative metrology concepts of *precision* and *trueness*, see the International Vocabulary of metrology (VIM) of the Joint Committee for Guides in Metrology (JCGM 200:2012). Strictly speaking, *accuracy* cannot be stated in quantitative terms, only in relative qualitative terms.

heat exchanger. Due to the relatively high mass flows and relatively low heated plate power input, the measured temperature differences between the heat exchanger inlet and outlet cannot be distinguished from their experimental uncertainty with sufficient precision. Hence the facility energy balance cannot be accurately assessed to the required precision. However, after performing a simple sensitivity analysis based on rough estimations of the experiment thermal losses, the experiment non-dimensional parameters didn't show important variations to the values indicated in this publication. Nevertheless, this important issue definitely needs to and is going to be addressed in future experiments by taking respective technical measures.

## 3.6 Experiment objectives and covered parameter set

The definition of the experimental campaign parameter set targets to cover both forced and mixed convection regimes at sufficiently high Reynolds numbers of $Re_h \sim \mathcal{O}\left(10^4\right)$ to ensure fully turbulent flow exhibiting a constant mean reattachment length $x_R$. This should establish in a BFS flow with $ER > 1.8$ and $Re_h \geq 20000$, see Nadge & Govardhan (2014). The aim of including $Re_h = 10000$ is to observe the BFS stagnation process. Lloyd & Sparrow (1970) predicted analytically the theoretical critical Richardson number $Ri_{crit,th}$ for the onset of buoyancy effects for a vertical flat plate for various Prandtl number ($Pr$) fluids. They predicted a critical Richardson number $Ri_{crit,th} \approx 0.05$ for $0.003 < Pr < 0.03$ . In the absence of alternatives at the time of planning the experiment, this value has been considered as an estimate for the onset of mixed convection, being aware of the differences between a vertical flat plate and a vertical BFS. This estimate seems to underpredict the measured onset of mixed convection for the present experiment by one order of magnitude. Thus, a more representative order of magnitude estimate for $Ri_{crit,th}$ has been derived afterwards for the actual present flow by means of scale analysis based on the work of Li & Djilali (1995).

The detailed uncertainty analysis methodology of the measured data is provided in appendix E. The uncertainty estimation has been calculated following the methodology proposed by the GUIDE TO THE EXPRESSION OF UNCERTAINTY IN MEASUREMENT (GUM) from the JOINT COMMITTEE FOR GUIDES IN METROLOGY (JCGM). All shown error bars in the data are expressed as combined extended uncertainties for a 95.45% confidence interval. The measured profiles for each probe in the next section are shown following the nomenclature of Fig. 3.2, where the exact position of each probe is also indicated. The error bars are shown only for

Table 3.6: Covered parameter set. The flow rate values indicate more significant digits than the measurement resolution.

| $\dot{V}$ $[l/s]$ | $\dot{m}$ $[kg/s]$ | $U_{b,in}$ $[m/s]$ | $\dot{q}$ $[W/m^2]$ | $\dot{Q}$ $[W]$ | $Re_h$ | $Re_h$(approx.) | $Ri_h$ |
|---|---|---|---|---|---|---|---|
| 0.267 | 1.71 | 0.083 | 585 | 28 | 10180 | 10000 | 0.006 |
| 0.530 | 3.40 | 0.166 | 2245 | 108 | 20208 | 20000 | |
| 0.792 | 5.08 | 0.248 | 4841 | 232 | 30197 | 30000 | |
| 0.266 | 3.40 | 0.083 | 3824 | 184 | 10142 | 10000 | 0.04 |
| 0.268 | 1.71 | 0.084 | 14274 | 685 | 10218 | | 0.15 |
| 0.530 | 3.40 | 0.166 | 3729 | 179 | 20208 | 20000 | 0.01 |
| 0.529 | 3.39 | 0.165 | 14644 | 703 | 20170 | | 0.04 |

those probes, for which the error bar is clearly distinguishable from the respective data symbol. For the sake of a better visualization of some profiles, only selected – yet generally representative – error bars are shown. For the shown dimensionless temperature profiles error bars have not been calculated, because the shown data only offers a qualitative flow description. For the local Nusselt number $Nu$ along the heated plate, some data points are missing since for these points the thermocouples broke during the mounting of the experiment.

# 4

# Flow and heat transfer analysis of a heated vertical BFS

## 4.1 Conceptual characterization of the flow field in the test section

Fig. 4.1 sketches the main flow phenomena present in the test section for forced (upper sketch) and mixed convection (lower sketch). In the sketch for the forced convection case the heat flux $\dot{q}_1$ is lower than the heat flux $\dot{q}_2$ for the mixed convection case. In Fig. 4.2 a snapshot of the instant velocity contours is shown for an isothermal large eddy simulation of an isothermal confined backward facing step, see Steiner (2019). Roman numbers are used in both figures to indicate important flow features. The test section is shown horizontally in both figures for a better visualization.

After the facility settling chamber and contraction 1 (see Fig. 3.1), the flow enters the test section through the inlet with a constant bulk velocity $U_b$ and a inlet bulk temperature $T_b$. The inlet flow boundary layer is assumed laminar. For guaranteeing a clearly defined turbulent boundary layer regime onset, a rectangular trip wire is placed a few units of length after the inlet to force the transition from laminar to turbulent boundary layer regime. On the contrary, the turbulent boundary layer onset point fluctuates having undesired pressure fluctuations as a consequence, which would affect the downstream flow characteristic, see Tihon *et al.* (2010). Furthermore, turbulent boundary layers grow faster than laminar ones. This effect is desired for this experiment, since a measurable boundary layer thickness is needed right before the step in order to properly describe the inlet boundary conditions of

the test section. The boundary layer thickness along the inlet section is depicted as *Ia* before the trip wire and *Ib* after it.

Due to the sudden expansion of the geometry cross section, the turbulent boundary layer detaches and separates from the wall at the step. A free shear layer flow develops between the incoming turbulent boundary layer and the recirculation region *II* after the step. The time averaged dividing streamline of the recirculation region, defined as the zero net mass flow rate line of the BFS cross-section, does not coincide with the time averaged zero-velocity line between the free shear layer and the recirculation region, see Nadge & Govardhan (2014). One further characteristic of the shear layer is the formation Kelvin-Helmholtz-instabilities or -eddies. Passed a few unit lengths from the step, smaller eddies *roll up* together to form large-scale eddies, see Le *et al.* (1997). These eddies take further momentum from the mean flow to form big recirculating flow structures rotating in clockwise direction. A second smaller recirculation region *III* forms between the step wall and the heated plate, which rotates in anti-clockwise direction. While the large-scale recirculation region growths, the reattachment length $x_R$ decreases and moves upstream; once it is detached from the step and is convected downstream by the mean flow, $x_R$ increases and moves downstream. This unsteady *flapping* of $x_R$ is a key characteristic of the transient dynamic behavior of a BFS flow. More details on the BFS dynamic behavior is found in Ma & Schröder (2017), Chovet *et al.* (2017), Pont-Vílchez *et al.* (2019), Ma *et al.* (2020) and references therein.

After $x_R$, a new boundary layer *Ic* develops under non-equilibrium conditions until a fully developed duct is achieved. In the literature there is no full agreement on this characteristic length, although a minimum of $\sim 50h$ seems to be a good estimate.

The test section in this study is an enclosed geometry with $AR = 2$, i.e. the influence of secondary flow of the second kind cannot be neglected. Secondary flow of the second kind is characterized by corner eddies, shown on the upper right part of Fig. 4.1, which transport fluid perpendicular to the streamwise main flow, see Bradshaw (1987) and Vinuesa *et al.* (2018). The effect of secondary flow of the second kind on the heat transfer characteristics of the present study is discussed in detail in section 4.5.

In forced convection, i.e. for a Richardson number $Ri_h$ below the critical Richardson number $Ri_{h,crit}$, temperature is transported as a passive scalar as it has no influence on either the flow statistically stationary flow nor the flow dynamics. This, independently of the BFS geometry orientation with respect to gravity. In a verti-

cal BFS configuration, as it is in the present study, the influence of buoyancy on the flow structure is as follows. Passed the critical Richardson number threshold $Ri_{h,crit}$, $x_R$ is observed to displace upstream, see the lower sketch in Fig. 4.1. The anti-clockwise rotating corner *III* recirculating eddy expands with increasing $Ri_h$ up to the point of detaching the clock-wise rotating recirculation region *II* from the heated wall. This, because buoyant forces transfer momentum to fluid particles near the heated plate, helping them to counteract the adverse pressure gradient imposed by the sudden duct expansion and hence the recirculation region.

## 4.2 Analysis for the forced convection case

The measured dimensionless velocity profiles for probes $P1$ to $P6$ and the local Nusselt number along the heated plate for variable $Re_h$ and constant $Ri_h = 0.006$ are shown in Fig. 4.3 and Fig. 4.4, respectively. The corresponding local Nusselt number is shown for the thermocouple center column, i.e. column $C$ at $z = 0$ in Fig. 3.2. The error bars of the velocity profile data are depicted for $Re_h \approx 30000$ and only for $P3$ and $P4$.

The flow enters the test section in a flat profile at $x = -10h$ ($P1$). As the flow proceeds downstream ($P2$) a turbulent boundary layer establishes triggered by the trip wire. Since the used probes are invasive, the velocity data at $x = 5h$ for $P3$ near and in the recirculation zone of the BFS exhibits a higher uncertainty than that considered in the error bars. The mean reattachment point $x_R$ is between $P3$ and $P4$, i.e. $5h < x_R < 10h$. In forced convection, as the temperature is transported as a passive scalar, the BFS recirculation region is not expected to exhibit alterations from the known behavior of isothermal BFS flows. This as can be concluded from the shape of the velocity profiles for $P3$ and $P4$. Downstream $x_R$ the redevelops towards a turbulent duct flow. For $P6$ at $x = 20h$ the turbulent duct flow is still not fully developed.

The measured velocity profiles for all $Re_h$ agree with each other within experimental uncertainty. The general flow structure seems to be independent on $Re_h$, however for $Re_h \approx 30000$ higher dimensionless velocities compared to those for $Re_h \approx 10000$ and $Re_h \approx 20000$ are observed in regions where the dimensionless velocity is larger. This can be explained in terms of local fluid dynamical phenomena around the probe tip. The higher the fluid velocity, the thinner the fluid velocity boundary layer and hence the higher the volume averaged fluid velocity around the probe tip. In other words, this non-linear interaction between the fluid flow at higher

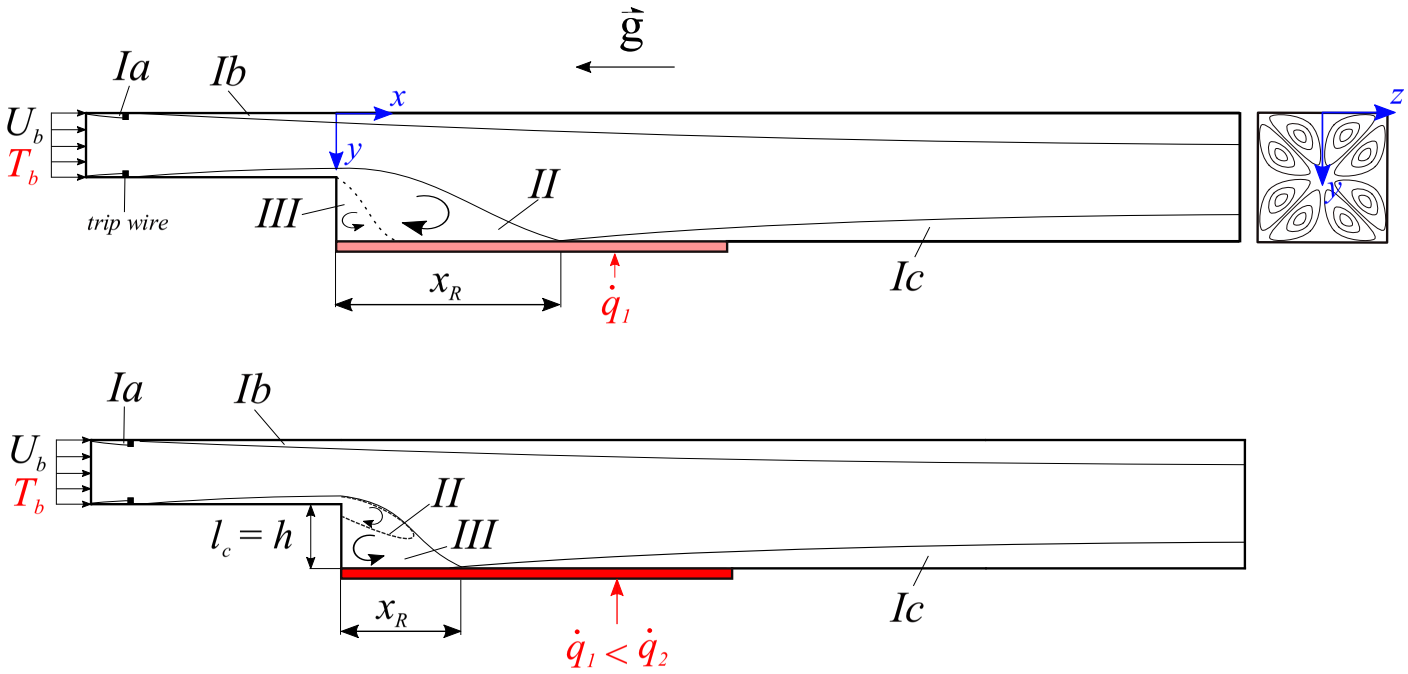


Figure 4.1: Sketch of statistically stationary flow phenomena present in a vertical confined BFS flow for forced convection (upper figure) and mixed convection (lower figure). On the right to the forced convection figure the typical streamline structure of secondary flow of the second kind is shown for a fully developed turbulent the square duct flow.

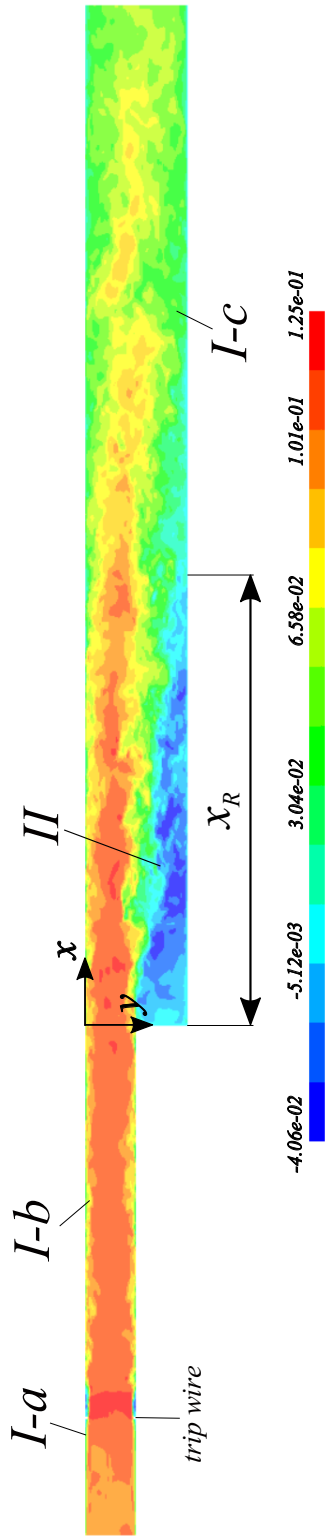


Figure 4.2: Snapshot of instant velocity contours of a large eddy simulation of an isothermal confined backward facing step flow for a flow visualization, see Steiner (2019). The simulations have been executed under similar yet not the same boundary conditions as for the experiment. Color contours represent the flow velocity ($x-$component) magnitude and direction. The indicated scale values are in $\frac{m}{s}$.

velocities and the measured probe sensitivities may explain the slightly higher measured values for $Re_h \approx 30000$. For more details see Schaub *et al.* (2021).

For $Pr < 1$ fluids, $Nu$ is relatively low, so that convective and conductive heat transfer rates are comparable in magnitude to each other. Thus, an increasing $Re_h$ yields higher $Nu$, as illustrated in Fig. 4.4. For all studied $Re_h$, a $Nu$ maxima can be estimated at $x \approx 8.75h$. This means that at this point $\Delta T = T_w - T_b$ is lowest, which does not necessarily mean that the mean reattachment point $x_R$ is located the same position. The relationship between a $Nu$ maxima and $x_R$ is not only determined by the flow structure but also by the conjugate heat transfer at the heated plate contact region with the fluid.

Besides the main $Nu$ maxima at $x \approx 8.75h$, two further maxima are observed at $x \approx 5h$ and $x \approx 12.5h$. One may argue the expected shape for local $Nu$ to be a nearly linear increase/decrease around $x_R$, which may be contained within the error bars. However, in all measured cases the maxima appear and pronounce with increasing $Re_h$ and they further seem to be independent of the heat input. An analysis made of the heated plate during its manufacturing and mounting on the test section, as well an a post test analysis, provides no evidence of an altered thermal boundary condition during the experimental campaign. However, it cannot be discarded entirely that these two maxima are an artifact of the experimental setup. A further possible explanation is that they arise as a result of the influence of secondary motions of the second kind originated due to the rectangular shape of the duct. However, it is hard to verify these hypotheses without any further data. The only available DNS data comparable to this experiment are that of Oder *et al.* (2019), which doesn't contain the local Nusselt number distribution along the heated plate.

## 4.3 Onset to mixed convection: impact of the Richardson number

### 4.3.1 For Reynolds number $Re \approx 10000$

The measured dimensionless velocity and dimensionless temperature profiles are shown in Fig. 4.5 and Fig. 4.6, respectively. In Fig. 4.7 the measured values for $P3$ are illustrated for detailed view of that dimensionless temperature profile. The time-averaged measured temperature points $\bar{T}$ have been normalized with the time-averaged inlet bulk temperature $\bar{T}_b$.The Nusselt number distribution along the

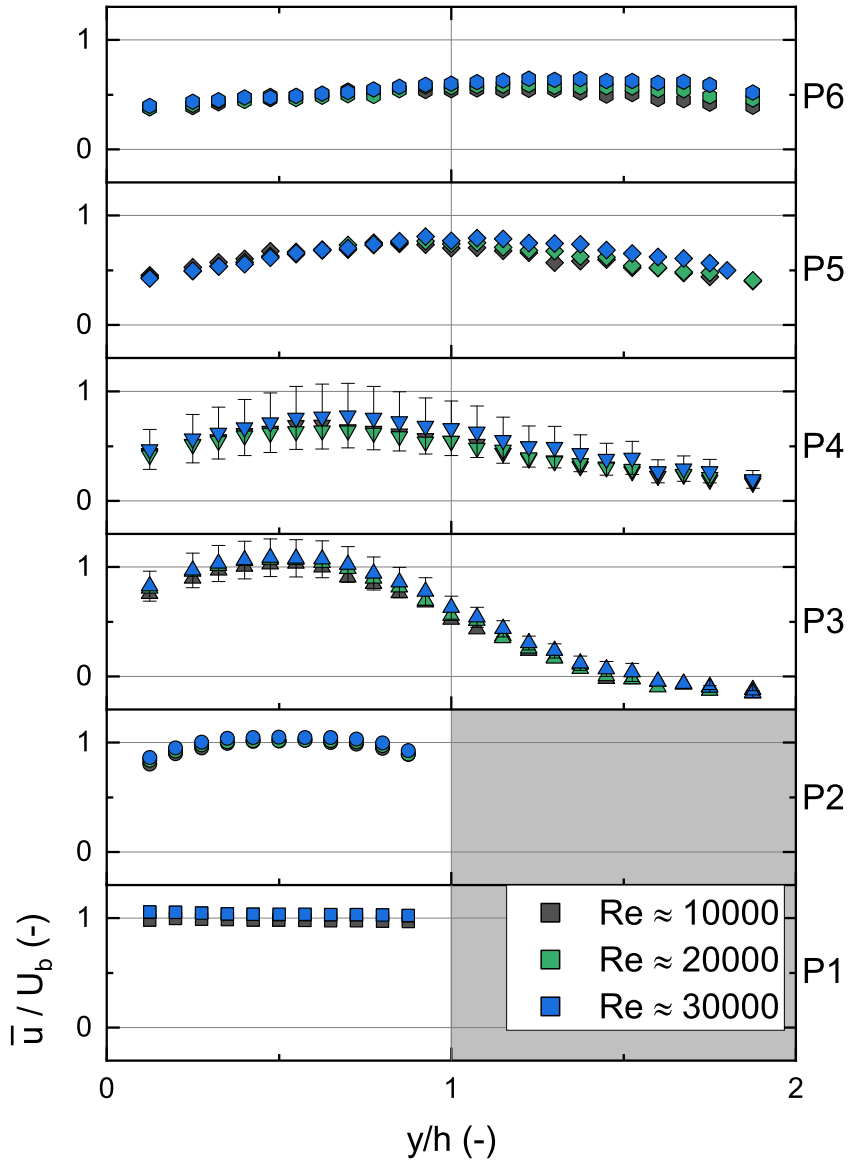


Figure 4.3: Measured dimensionless velocity profiles in the centerplane ($z/h = 0$) at several positions for different $Re_h$ at a constant $Ri_h = 0.006$.

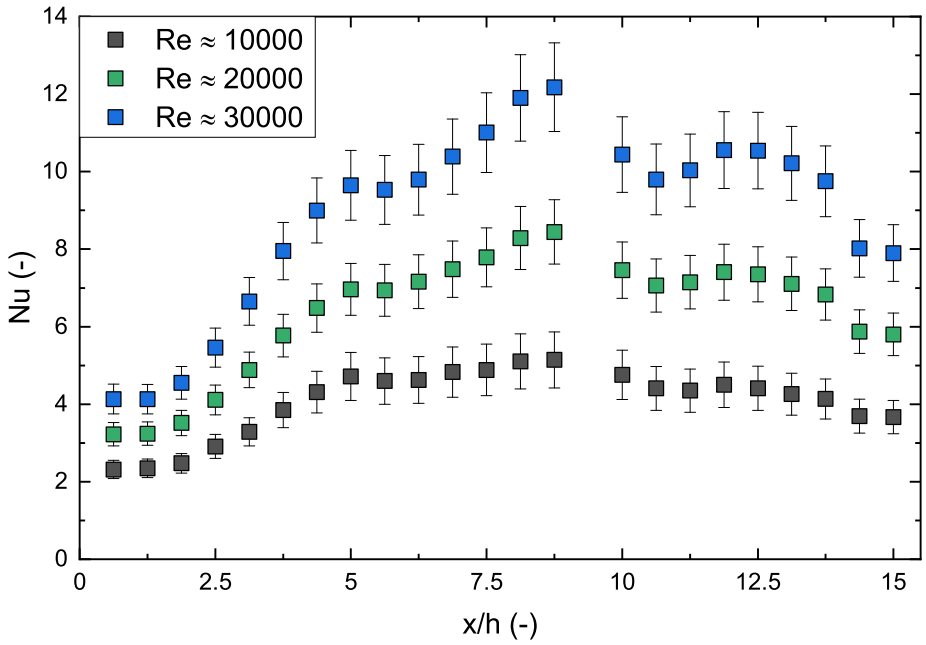


Figure 4.4: Measured local $Nu$ along the heated plate centerline ($z/h = 0$, thermocouple column $C$) for different $Re_h$ at a constant $Ri_h = 0.006$.

heating plate is depicted in Fig. 4.8. The error bars of the velocity profile data are only indicated for $P3$ and $P4$ for $Ri_h = 0.15$.

This parameter set shows the same behavior for $P1$ at $x = -10h$ and $P2$ at $x = 0h$ as for the results for forced convection presented in the previous section. An onset of buoyancy effects on the flow is expected at $Ri_{crit,th} \sim 0.05$. Analyzing Fig. 4.5 however shows that the velocity profiles for $Ri_h = 0.006$ and $Ri_h = 0.04$ coincide within experimental uncertainty. Although the error bars for $Ri_h = 0.15$ overlap with those for the other cases in some extent, a marginal deviation is observed in terms of an acceleration of the fluid in the region near to the heated plate due to buoyancy forces opposing to the fluid motion in the recirculating region. This behavior is characteristic for a mixed convection regime in a BFS flow and is also observed in DNS simulations of Niemann & Fröhlich (2016b). This indicates that the originally used order of magnitude estimate for $Ri_{crit,th}$ is underestimated by about one order of magnitude. This is not surprising because the mixed convection onset threshold has been calculated for a vertical flat plate (Lloyd & Sparrow (1970)).

The measurement points along an $y-$axis profile for every probe have been measured consecutively in time so that for the measurement of temperature profiles the fluctuation shape shown in Fig. 3.15 is observed in Fig. 4.7 as a baseline noise fluctuation along the measured profiles. The dimensionless temperature profiles are hence not conclusive due to the loop baseline temperature fluctuation, see section 3.5. Nevertheless, they the indicate the expected trend. The values in the recirculation region for for $Ri_h = 0.006$ and $Ri_h = 0.04$ are similar, however a relative temperature increase is observed for $Ri_h = 0.04$. Whether this trend can be distinguished from experimental uncertainty cannot be stated with the current data. However, the values for $Ri_h = 0.15$ indicate temperature increase relative to the inlet flow temperature. This induces buoyancy forces leading to the flow acceleration near the heating plate observed in Fig. 4.5.

The presumably onset of mixed convection for $Ri_h = 0.15$ is almost not observable in the $Nu$ distributions. All values but the first one at $x \approx 0.5h$ cannot be distinguished from each other within experimental uncertainty.

### 4.3.2 For Reynolds number $Re_h \approx 20000$

The measured dimensionless velocity profiles and Nusselt number distribution for different $Ri_h$ at a fixed $Re_h \approx 20000$ set are illustrated in Fig. 4.9 and Fig .4.10, respectively. The Nusselt number distribution is shown along the center plane at

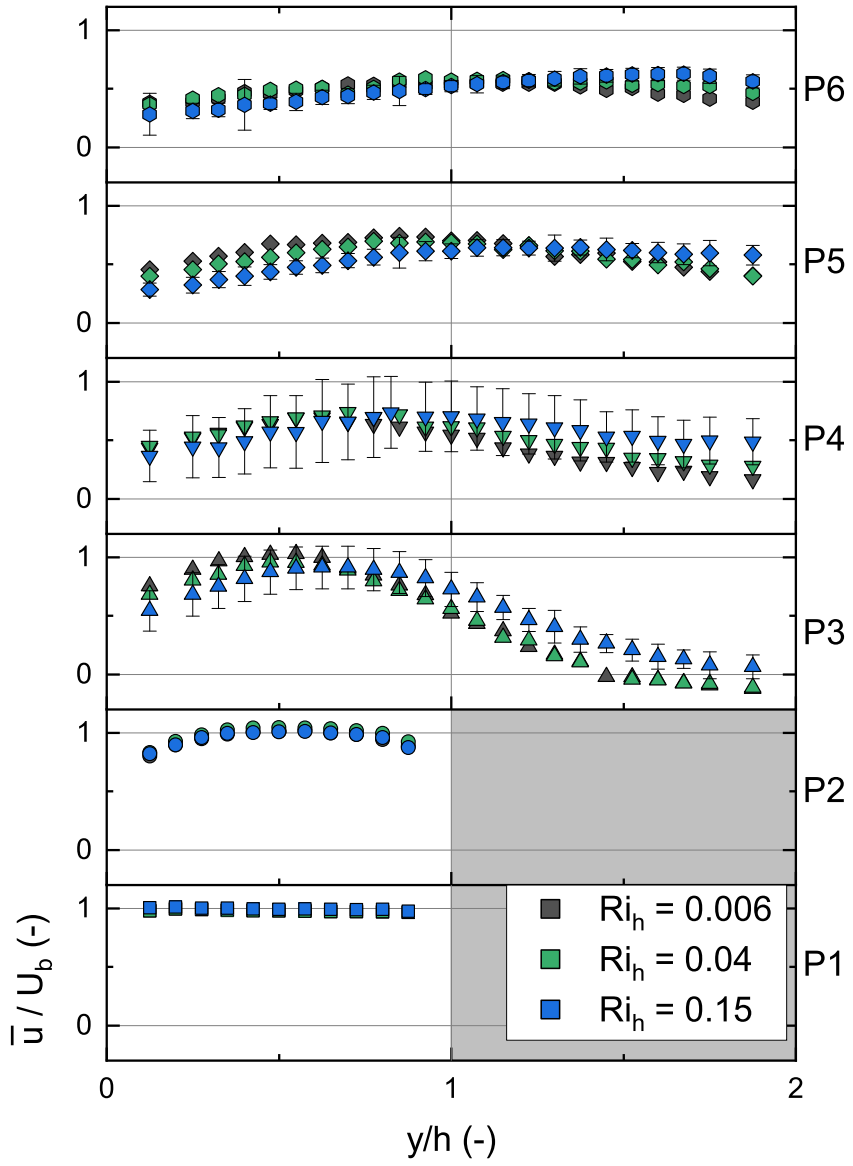


Figure 4.5: Measured dimensionless velocity profiles in the centerplane ($z/h = 0$) at several positions for a constant $Re_h \approx 10000$ and different $Ri_h$.

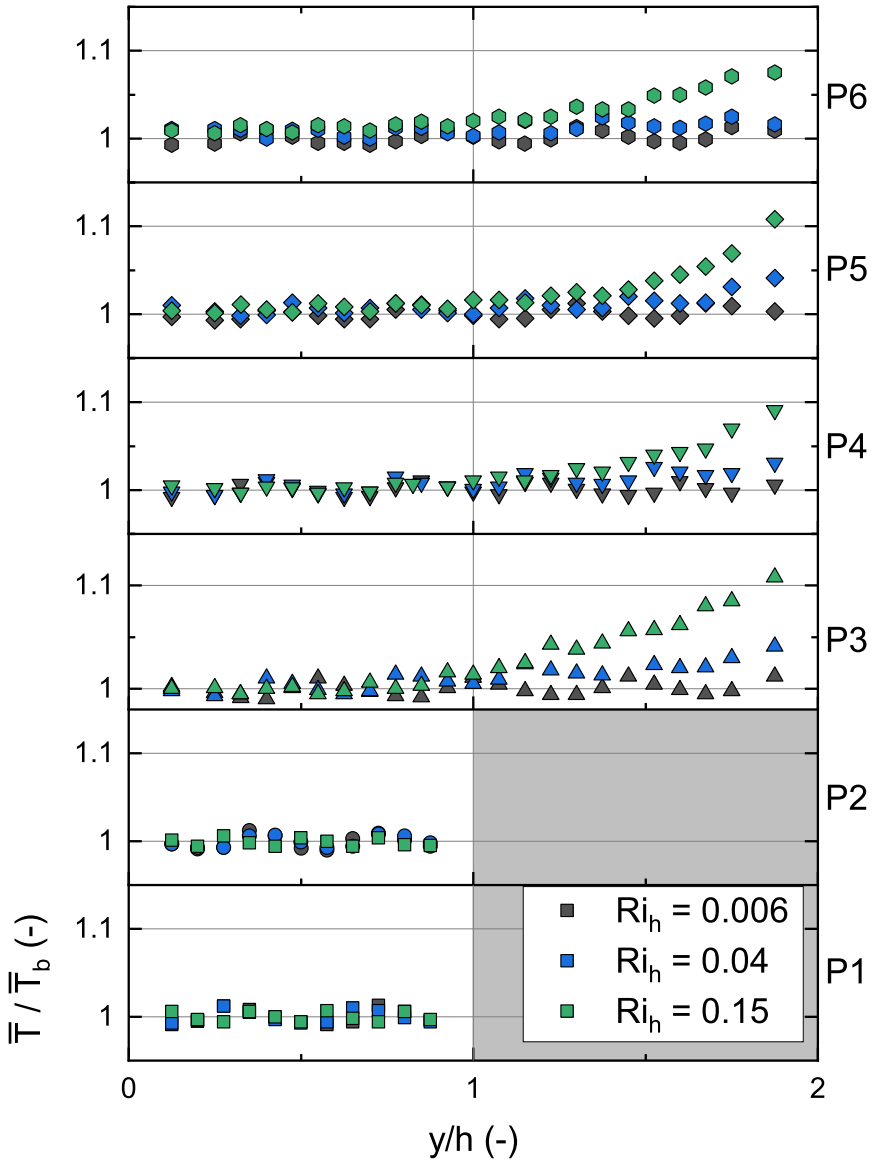


Figure 4.6: Measured dimensionless temperature profiles in the centerplane ($z/h = 0$) at several positions for constant $Re_h \approx 10000$ and different $Ri_h$.

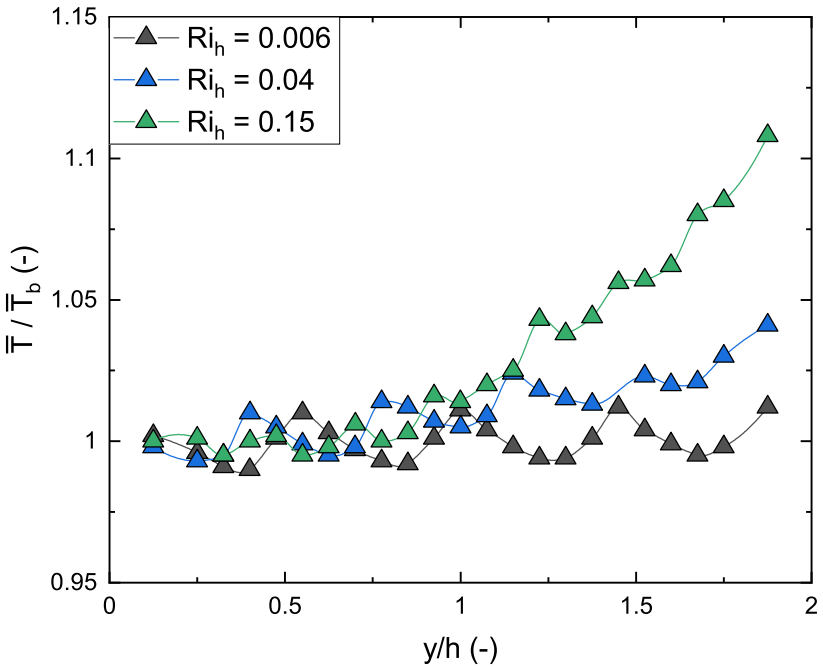


Figure 4.7: Detailed view of the measured data for *P*3 shown in Fig. 4.6. The measurement points are connected with a line to highlight the facility temporal baseline temperature fluctuation.

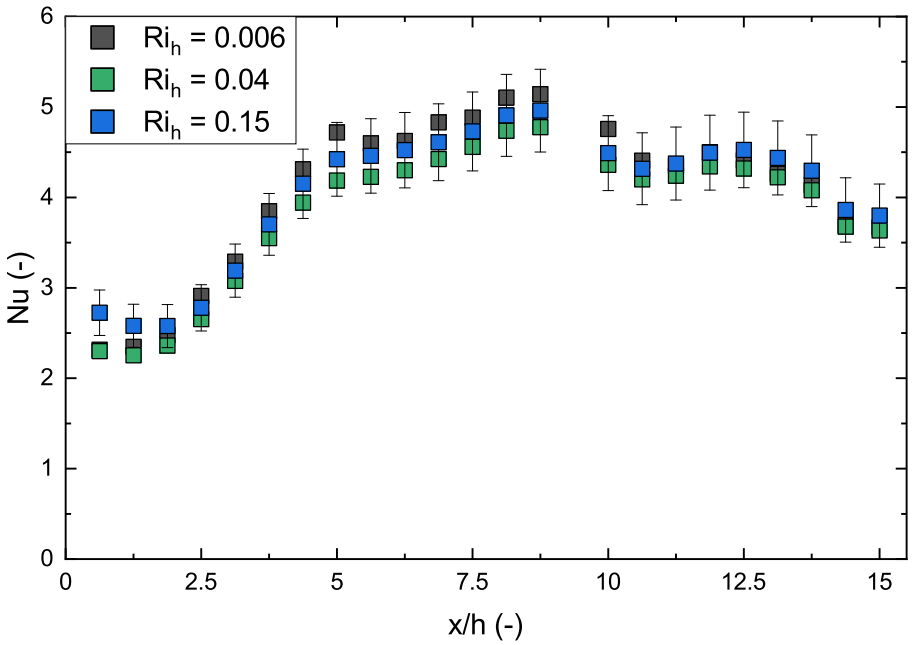


Figure 4.8: Measured local $Nu$ along the heated plate centerline ($z/h = 0$, thermocouple column $C$) for different $Re_h \approx 10000$ and different $Ri_h$.

$z = 0$, i.e. for the thermocouple center column $C$ in Fig. 3.2. The error bars of the velocity profile data are depicted for $Ri_h = 0.04$ and only for probes $P3$ and $P4$.

Observations for the velocity profiles and $Nu$ distributions for this case do not deviate from the previous results and analysis. It seems that the onset of mixed convection is independent $Re_h$, although this hypothesis cannot be validated in the present experimental campaign. For $Re_h \approx 20000$ and $Ri_h = 0.04$ the heated plate power supply reached its upper limit, hence the $Ri_h = 0.15$ case for $Re_h \approx 20000$ was not attained.

### 4.3.3 Theoretical order of magnitude estimation of the critical Richardson number

The following analysis is based on Li & Djilali (1995) who predicted the $Re_h$ qualitative dependency of $x_R$ for a non-confined BFS by means of dimensional analysis. Here, a similar scale analysis is presented to estimate $Ri_{h,crit}$ considering inertial and buoyancy effects in the equations but neglecting the viscous terms.

The starting point are the $2D$ Navier-Stokes equations including buoyancy effects, which are modeled assuming the Boussinesq approximation. The steady state equations read to

$$u\frac{\partial u}{\partial x} + v\frac{\partial u}{\partial y} = -\frac{1}{\rho_{ref}}\frac{\partial p}{\partial x} + \nu_{ref}\left(\frac{\partial^2 u}{\partial x^2} + \frac{\partial^2 u}{\partial y^2}\right) + \left(\rho_{ref}\beta_{ref}\Delta T\right) g, \tag{4.1}$$

$$u\frac{\partial v}{\partial x} + v\frac{\partial v}{\partial y} = -\frac{1}{\rho_{ref}}\frac{\partial p}{\partial y} + \nu_{ref}\left(\frac{\partial^2 v}{\partial x^2} + \frac{\partial^2 v}{\partial y^2}\right). \tag{4.2}$$

For the scale analysis, the equations are expressed in terms of characteristic length scales $x_c$ and $y_c$, velocities $u_c$ and $v_c$ and critical temperature difference $\Delta T_{crit}$ in the region near the recirculation region. These equations read to

$$\frac{u_c^2}{x_c} + \frac{v_c u_c}{y_c} \sim -\frac{1}{\rho_{ref}}\frac{p_c}{x_c} + \nu_{ref}\left(\frac{u_c}{x_c^2} + \frac{u_c}{y_c^2}\right) + \left(\rho_{ref}\beta_{ref}\Delta T_{crit}\right) g, \tag{4.3}$$

$$\frac{u_c v_c}{x_c} + \frac{v_c^2}{y_c} \sim -\frac{1}{\rho_{ref}}\frac{p_c}{y_c} + \nu_{ref}\left(\frac{v_c}{x_c^2} + \frac{v_c}{y_c^2}\right). \tag{4.4}$$

Replacing $v_c \sim u_c y_c / x_c$ (continuity) and after some algebra, the following expression is obtained

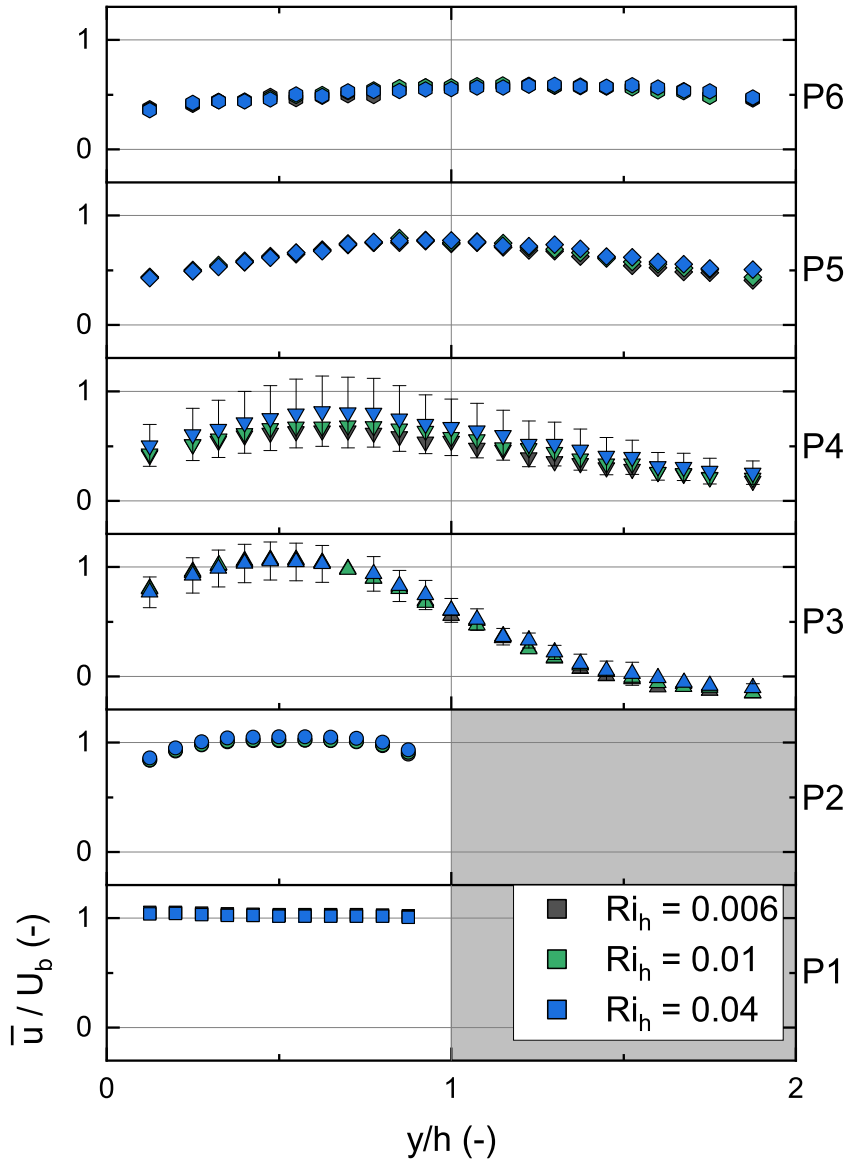


Figure 4.9: Measured dimensionless velocity profiles in the centerplane ($z/h = 0$) at several positions for a constant $Re_h \approx 20000$ and different $Ri_h$.

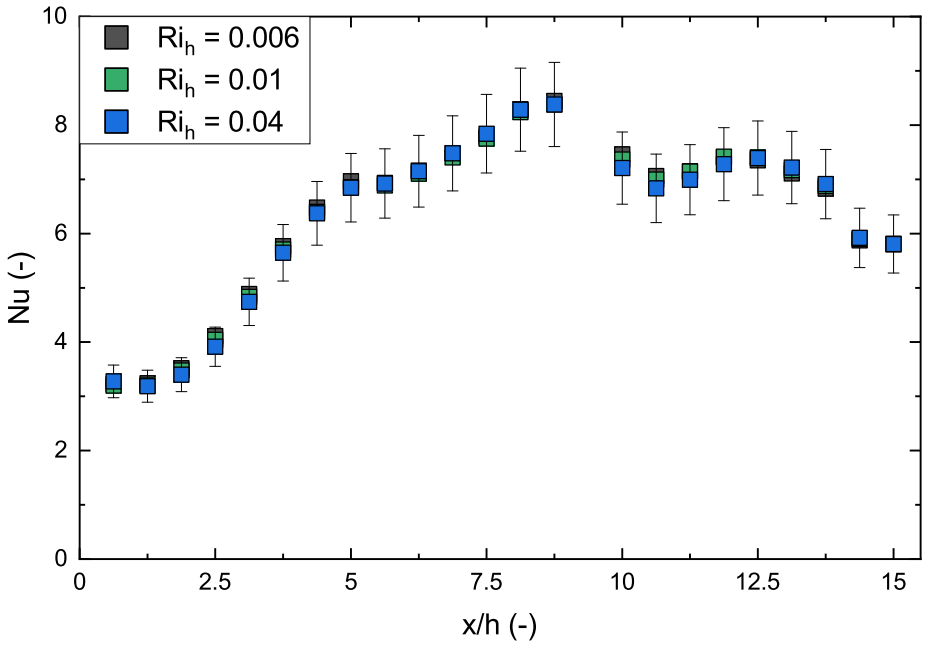


Figure 4.10: Measured local $Nu$ along the heated plate centerline ($z/h = 0$, thermocouple column $C$) for different $Re_h \approx 20000$ and different $Ri_h$.

$$u_c^2\left(\frac{y_c^2}{x_c^2}-1\right)+x_c\left(\rho_{ref}\beta_{ref}\Delta T_{crit}\right)g\sim\nu_{ref}u_c x_c\left(\frac{y_c^2}{x_c^2}-1\right)\left(\frac{1}{x_c^2}+\frac{1}{y_c^2}\right). \quad (4.5)$$

Since this is a rough order of magnitude estimate, the viscous terms are neglected in a next step. Rearranging Eq. (4.5), one obtains

$$\frac{y_c^3}{x_c^3}-\frac{y_c}{x_c}-Ri_{h,crit}\sim 0. \quad (4.6)$$

Considering only the real solutions to Eq. (4.6), $Ri_{h,crit}={}^{2\sqrt{3}}/_{9}\approx 0.385=O\left(10^{-1}\right)$ is obtained.

Again, this is only a rough order of magnitude estimate assuming the case when inertial forces are in the same order as buoyancy forces. Nevertheless, the result agrees well the measurement data. For the case $Re_h\approx 10000$ and $Ri_h=0.15=O\left(10^{-1}\right)$ one can observe in Fig. 4.5 that buoyancy forces begin to become noticeable.

## 4.4 Impact of boundary conditions on heat transfer analysis and data interpretation

### 4.4.1 Flow symmetry

A total of five thermocouple columns have been integrated into the heated plate to assess the flow symmetry with respect to the $XY-$plane at $z=0$. The idea is also to obtain more detailed spatial distribution of the local $Nu$ distribution on the heated plate. The result for thermocouple columns $A$ at $z\approx 0.66h$, $C$ at $z=0h$ and $E$ at $z\approx -0.66h$ are shown in Fig. 4.11 including their respective error bars. A point to consider is that the actual temperature differences between the columns are below $0.8^{\circ}C$ for the highest heat flux rates and even lower for the rest of the cases.

The recorded local $Nu$ distribution is not symmetric with respect to the center plane at $z=0$. Although the error bars of columns $C$ and $E$ overlap, it is clear that the data for column $A$ are lower than for the other two. Particularly in the region where the $Nu$ maxima are located, i.e. the minima for $\Delta T=T_w-T_b$. This is very unlikely to be associated with a flow asymmetry. The only explanation for the local $Nu$ asymmetry is the heated plate itself. Taking a look at Fig. 3.4 this becomes evident. Here, the back of the copper plate where the thermocouples

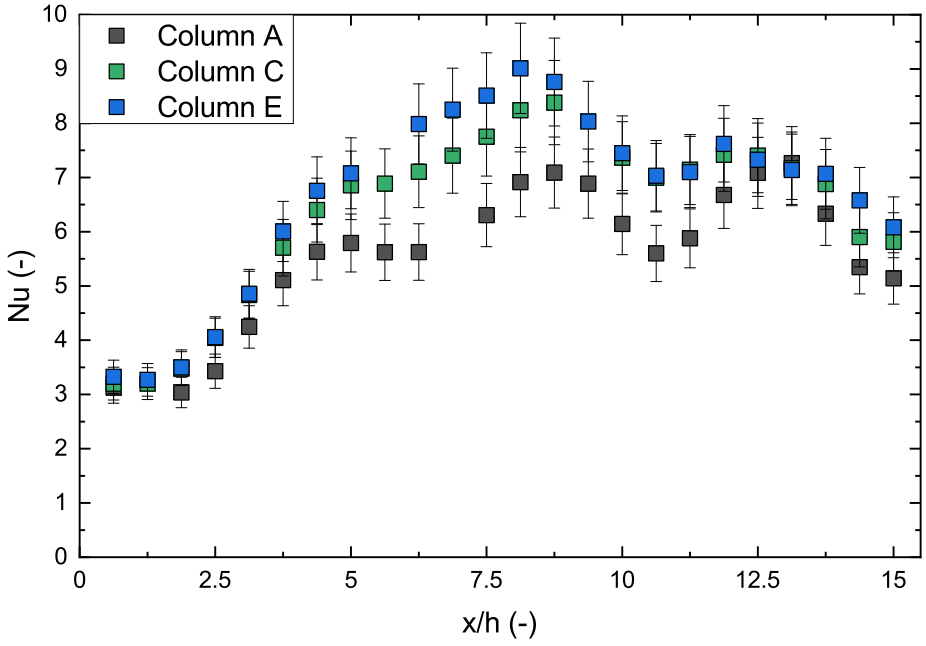


Figure 4.11: Measured local $Nu$ distribution close to the fluid-solid interface of the heated plate for thermocouple columns $A$, $C$ and $E$ for $Re_h \approx 20000$ and $Ri_h = 0.04$.

have been inserted are shown. All thermocouples are guided from only one side, making the heat conductivity resistance on this side higher. That is, heat tends to diffuse into the flow on the side of column $A$. This also matches the observation of the Nusselt number distribution. For column $A$ the Nusselt numbers are generally lower, meaning that the heat transfer due to thermal conductivity is higher on this side than for the other two columns. The fact that the region near the reattachment length is where the three curves separate the most, is a further argument in favor of explaining the two smaller maxima in terms of flow phenomena. The lower the Nusselt number, the higher the heat transfer due to thermal conductivity and the smaller the discrepancy between the curves (within experimental uncertainty).

### 4.4.2 Relationship between the thermal boundary definition and the data interpretation

Why can't the mixed convection onset be observed in the $Nu$ profiles yet in the velocity profiles it can? To answer this question, conjugate heat transfer numerical

simulations of the experiment have been performed.

### Numerical simulation setup

The steady-state Reynolds Averaged Navier-Stokes equations have been solved in ANSYS CFX for the present BFS geometry. The buoyancy term has been modelled using the Boussinesq approximation. The conjugate heat transfer problem has been numerically solved, i.e. by including the heated plate as a solid body in the computational domain. A constant specific heat flux $\dot{q} = \dot{Q}_{HP}/A_{HP}$ has been applied on the exterior surface of the heated plate similar as in the experiment. The inlet boundary condition is a constant mass flow rate for $Re = 10218$ with a constant velocity profile and an inlet turbulence intensity of 1%.

Numerical schemes of first order have been used for the momentum and energy equations (otherwise the solution wouldn't converge), while the turbulence related quantities are calculated with second order schemes. The simulation convergence has been assessed by letting the calculation run until all numerical residuals are below $10^{-6}$ and by judging local monitoring points of relevant variables such as the three velocity components, the turbulent kinetic energy and the flow and heated plate temperature. The monitoring points in the flow have been located at two points for each variable; one in the computational domain outlet and the other in the recirculation region.

In a geometry independence study an outlet section extension of $30h$ proved to be long enough. The numerical mesh has a value of $y^+ = u_\tau y/\nu \approx 1$ but at some local areas around the trip wire, where $u_\tau = \sqrt{\tau_w/\rho}$ with $\tau_w$ the wall shear stress and $\rho$ the fluid density; $y$ the distance between the computational domain wall and the first numerical cell center and $\nu$ the fluid kinematic viscosity. A qualitative mesh independence study has been performed and a mesh independent solution has been achieved based on the local inspection of relevant variable profiles (mean velocity and temperature, turbulent kinetic energy, Reynolds stresses, etc.).

The profiles have been extracted at the same position as the permanent magnet probes are mounted in the test section. The Reynolds stress tensor has been calculated with a baseline omega-based Reynolds stress model. The turbulent heat flux has been modelled by calculating the turbulent Prandtl number $Pr_t$ using the Kays correlation $Pr_t = 0.85 + 0.7/Pe_t$, where $Pe_t = \nu_t/\nu$ with $\nu_t$ the eddy kinematic viscosity and $\nu$ the liquid metal kinematic viscosity.

This section is *not* intended to be a validation of our numerical simulations, but

to offer a *qualitative* comparison between our numerical and experimental results. The aim is to show the *qualitative* effect that the way the heat flux $\dot{q}$ is calculated has on the local $Nu$ distribution along the heated plate and to gain further insight into the flow physics.

**Nusselt number physical interpretation for this case**

Fig. 4.12 depicts the numerical results for the local $Nu$ distribution along the heated plate center-plane at $z = 0$ for $Ri_h = 0.006$ and $Ri_h = 0.15$ for $Re_h = 10218$ together with the experimental results for $Nu$ for $Ri_h = 0.15$ at $Re_h \approx 10000$ (same data points as for Fig. 4.8). Four curves for the numerical results of $Nu$ are depicted in Fig. 4.12, two for each $Ri_h$. The difference between the two curves for each dimensionless parameter set relies on the heat flux $\dot{q}$ used to calculate $Nu$ in Eq. (3.9). Once assuming a constant heat flux over the heated plate, i.e. $\dot{q} = \dot{Q}_{HP}/A_{HP} = \dot{q}_{const}$ (as for the experiment), and once using the local heat flux distribution along the heated plate as obtained from the numerical results, i.e. $\dot{q} = \dot{q}_{local} = \lambda_{fluid} \frac{\partial T}{\partial y}\Big|_{y=0}$.

The heated plate Biot number is $Bi = \mathcal{O}\left(10^{-1}\right)$ and although the $Bi \gg 0.1$ condition is not fully satisfied, a constant heat flux boundary condition is assumed as a first approximation[1]. In fact, in Fig. 4.12 a good qualitative agreement of the experimental and numerical results is observed for $\dot{q}_{const}$ for the $Ri_h = 0.15$, case. The trend for $Nu$ at lower $x/h$ in Fig. 4.8 is captured as well by the numerical results. However, the disagreement between the $\dot{q}_{const}$ and $\dot{q}_{local}$ in Fig. 4.12 becomes obvious. This evidences that a constant heat flux boundary condition is not applicable to this case. This can also be seen in Fig. 4.13, where contours of $\dot{q}_{local}$ are illustrated normalized with $\dot{q}_{const}$ at the contact surface between the heated plate and the liquid metal. The correct thermal boundary condition for the heated plate is hence a mixed type boundary condition. Thus, $Nu$ is a function of *both* the local temperature difference $\Delta T(x,z) = T(x,z) - T_b$ *and* the local heat flux $\dot{q}_{local}(x,z)$ distributions. The presence of a mixed type thermal boundary condition is further evidenced when trying to relate $\dot{q}_{local}/\dot{q}_{const}$ in Fig. 4.13 to the dimensionless temperature difference $\theta$

$$\theta = \frac{\Delta T}{\Delta T_c} = \frac{T_{local} - T_b}{\Delta T_c} = \frac{T_{local} - T_b}{\frac{\dot{q}_{const} h}{\lambda_{ref}}}, \tag{4.7}$$

in Fig. 4.14. There is no evident relationship between $\theta$ and $\dot{q}_{local}/\dot{q}_{const}$.

[1]For $Bi \gg 0.1$ temperature gradients within the heated solid are much larger than those in the fluid boundary layer, i.e. a constant heat flux boundary condition can be assumed (Incropera *et al.* (2017)).

This explains why only for the $\dot{q}_{local}$ cases in Fig. 4.12 the mixed convection case can be distinguished from the forced convection case. In other words, the reason why the onset to mixed convection in Fig. 4.8 is not observed is explained by the way the measured $Nu$ has been defined, i.e. by taking $\dot{q} = \dot{q}_{const}$ in Eq. (3.9) instead of $\dot{q} = \dot{q}_{local}$. This high sensitivity on thermal boundary conditions is typical for liquid metal flows contrary to the moderate $Pr$ fluid case, see Straub *et al.* (2019) and Kays *et al.* (2007).

To measure $\dot{q}_{local}$ is not a trivial task. An alternative is to locally measure $T$ and then solve the two-dimensional inverse Fourier problem as proposed by Woodfield *et al.* (2006). This procedure will be implemented in future experiments.

It is important to assess the physical interpretation to be given to $Nu$ in Fig. 4.12. For the $\dot{q}_{const}$, $Nu$ may be interpreted as the reciprocate of the dimensionless wall temperature only. For the $\dot{q}_{local}$ cases, $Nu$ can be interpreted as approximately proportional to the dimensionless wall temperature gradient, see Eq. (2.23). To interpret $Nu$ as usual, i.e. as the actual dimensionless wall temperature gradient, $T_b$ needs to be determined ad hoc (Moffat (1998)). Here, $T_b$ has been defined as $T_b = T_{inlet}$ in the absence of other alternatives.

In any case, as mentioned by Kasagi *et al.* (1989) conjugate heat transfer CFD calculations are generally needed in order to reproduce the experimental conditions when heated plates are present, since the temperature distribution within the heated plate strongly affects the contact surface temperature distribution between the heated plate and the fluid.

**Nusselt number as an indicator to the mean reattachment point**

In Fig. 4.15 the streamwise skin friction coefficient $C_f$ component along the heated plate centerplane at $z = 0$ is shown, where $C_f = \tau_w/\rho U_b^2$ with $\tau_w$ the wall shear stress. Flow stagnation regions can be identified by zero-crossings of $C_f$. The general behavior of $C_f$ coincides with that reported in Niemann & Fröhlich (2016b).

The BFS reattachment point can (but doesn't necessarily need to) be defined as a zero-crossing of $C_f$. It is interesting to note that for this case the flow reattachment point $x_R$ at $x/h \approx 10$ for $Ri_h = 0.006$ and at $x/h \approx 5$ for $Ri_h = 0.15$ can't be related in an obvious way to $Nu$ in Fig. 4.12. This means that for a mixed thermal boundary condition $Nu$ loses its capability of being an indicator of $x_R$.

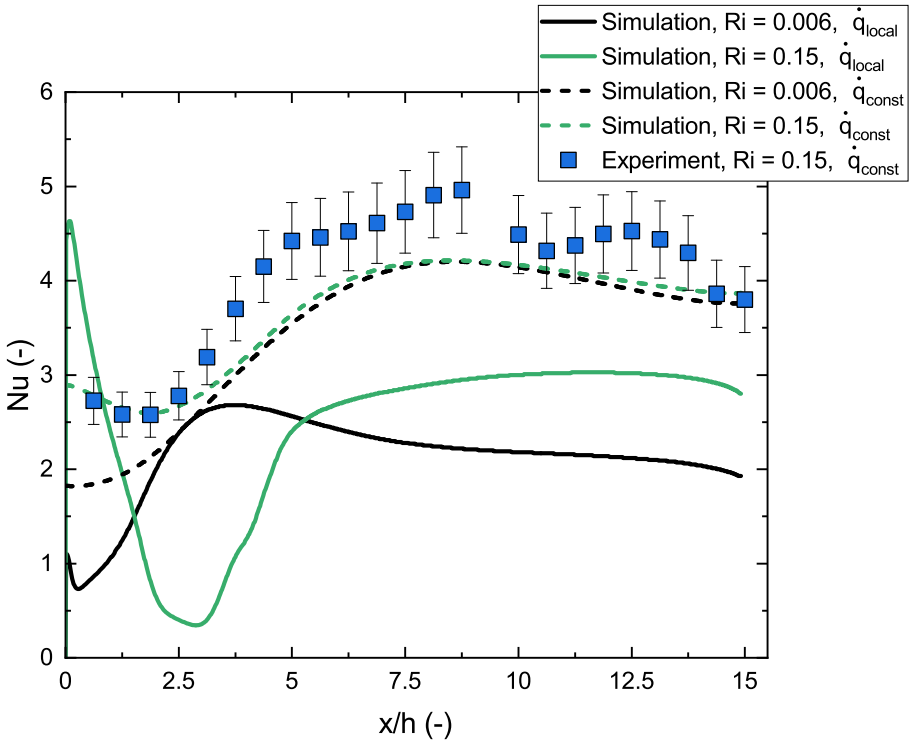


Figure 4.12: Comparison of measured and calculated Nusselt number $Nu$ distribution along the centerline ($z/h = 0$) of the heated plate.

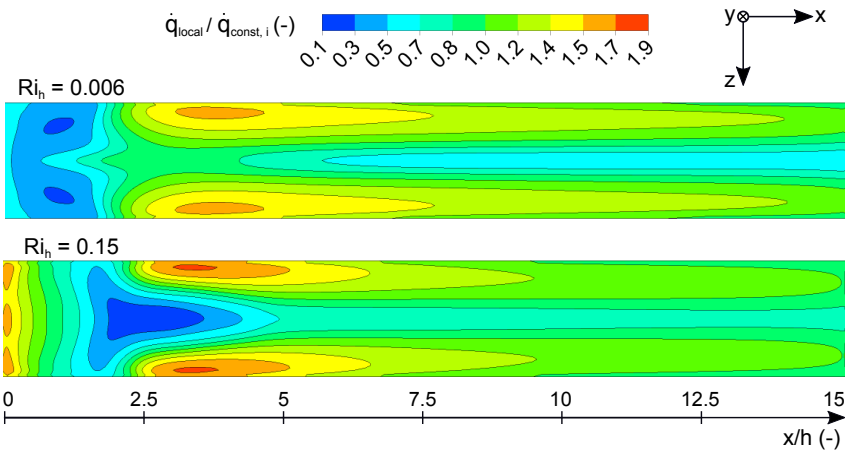


Figure 4.13: Contours of $\dot{q}_{local}$ at the liquid/solid interface normalized with $\dot{q}_{const}$ for $Ri_h = 0.006$ and $Ri_h = 0.15$.

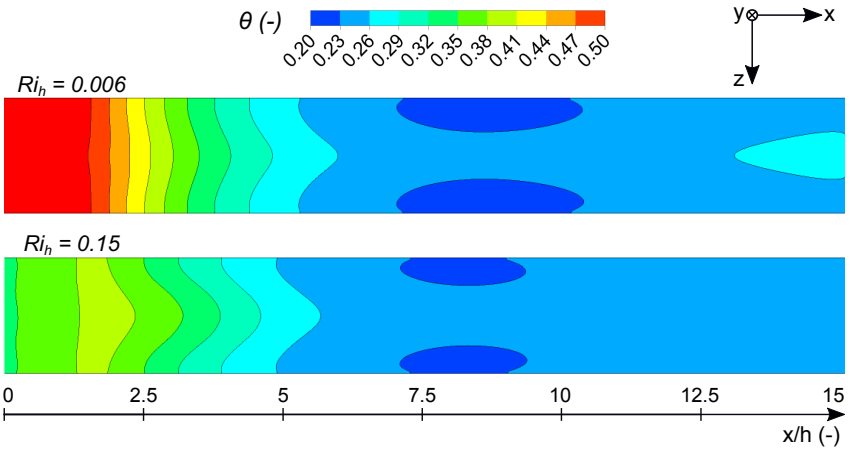


Figure 4.14: Contours for $\theta = {}^{T_{local}-T_b}/_{\Delta T_c}$, with $\Delta T_c = {}^{\dot{q}_{const}h}/_{\lambda_{ref}}$ at the liquid/solid interface for $Ri_h = 0.006$ and $Ri_h = 0.15$.

## 4.5 Heat transfer mechanisms between the bulk flow and the liquid/solid interface

Figures 4.13 and 4.14 evidence further non-trivial and non-intuitive phenomena. Why are there heat flux maxima (${}^{x}/_{h} \sim 3$) and temperature minima (${}^{x}/_{h} \sim 8$) at the sides of the heated plate and not at the center near the reattachment point according to Fig. 4.15, as expected from the typical behavior of non-confined BFS? Does the three-dimensional character of the heated plate play a role in the present conjugate heat transfer problem?

To answer these questions, Figs. 4.16, 4.17, 4.18 and 4.19 are introduced. They show both fluid and solid domains of the BFS RANS calculations described in section 4.4.2, the fluid domain corresponding to the liquid metal flow and the solid domain corresponding to the heated plate. In the fluid domain normalized velocity vectors are shown together with the corresponding velocity contours. Fig. 4.16 shows the dimensionless streamwise velocity component ${}^{u}/_{U_b}$ for forced and mixed convection at the centerplane (${}^{z}/_{h} = 0$), while Figs. 4.18 and 4.19 show the normalized resultant spanwise velocity component ${}^{s}/_{U_b}$ at different $x-$ positions for forced and mixed convection, where

$$s = \sqrt{v^2 + w^2}, \tag{4.8}$$

with $v$ the $y-$axis velocity component and $w$ the $z-$axis velocity component.

In all solid domains the contours of the normalized temperature difference $\theta$

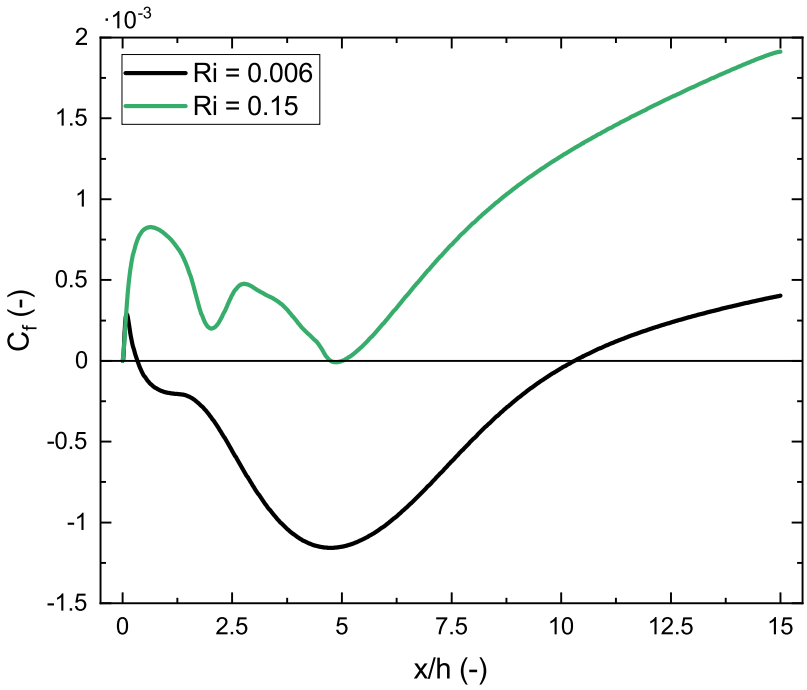


Figure 4.15: Comparison of the streamwise skin friction coefficient coefficient on the heated plate in the BFS geometry centerplane ($z/h = 0$) for $Ri_h = 0.006$ and $Ri_h = 0.15$.

(Eq. (4.7)) are depicted.

### Conjugate heat transfer phenomena between the fluid and the heated plate

The observed velocity vectors and contours in Fig. 4.16 for the BFS geometry centerplane at $z/h = 0$ and in Fig. 4.17 for the BFS geometry plane at $z/h = 0.5$ correspond to the made remarks in past sections and to the qualitative flow behavior illustrated in Fig. 4.1. However, it is interesting to note that the expected BFS flow behavior is not observed in the geometry centerplane but in the plane at $z/h = 0.5$. In the heating plate, $\theta$ shows a very similar behavior, independently of the plane.

Recalling that the heat flux vector is perpendicular to its respective isotherms, the heat flux path in the heated plate can be traced. For forced convection, it becomes clear that heat is mainly removed from the heated plate at $7.5 \lesssim x/h \lesssim 12.5$ because heat flux vectors point towards this region, which at the same time corresponds to the region around the reattachment point $x_R$, see Fig. 4.15. For mixed convection two main heat removal regions are identified, one at $0 \lesssim x/h \lesssim 1$ and a second at $7.5 \lesssim x/h \lesssim 12.5$. However, in this case, the maximum heat removal region does not coincide with the observed $x_R$ in Fig. 4.15. This may be explained by on how $x_R$ has been defined, i.e. the zero-crossing point of $c_f$ which at the same time corresponds to a point of zero *streamwise* component velocity. In forced convection, heat is mainly removed by the eddy roll-up phenomenon which constantly transports or "throws" cold fluid from the bulk flow towards the heated plate. In the mixed convection case, it seems that the clockwise rotating recirculation region (*II* in Fig. 4.1) is not fully detached from the heated wall. This is observed in Fig. 4.17. As a consequence, the clockwise rotating eddy transports cold fluid from the bulk and *passes* it to the growing anti-clockwise recirculation region (*III* in Fig. 4.1) which on its side "throws" cold fluid onto the heated plate at $0 \lesssim x/h \lesssim 1$. On the other hand, cold fluid Kelvin-Helmholtz eddies formed along the shear layer collide onto the heated plate in the region $7.5 \lesssim x/h \lesssim 12.5$. This may explain the two $Nu$ maxima for the mixed convection case in Fig. 4.12.

### The role of secondary flow of the second kind

Observing the magnitude of the color scales for $s$ in Figs. 4.18 and 4.19 the effect of secondary flow of the second kind becomes clear. The magnitude of this flow reaches high values of 20% of the inlet bulk flow velocity $U_b$, contrary to the usual values for fully developed turbulent duct flow reported in the literature of $1-2\%$,

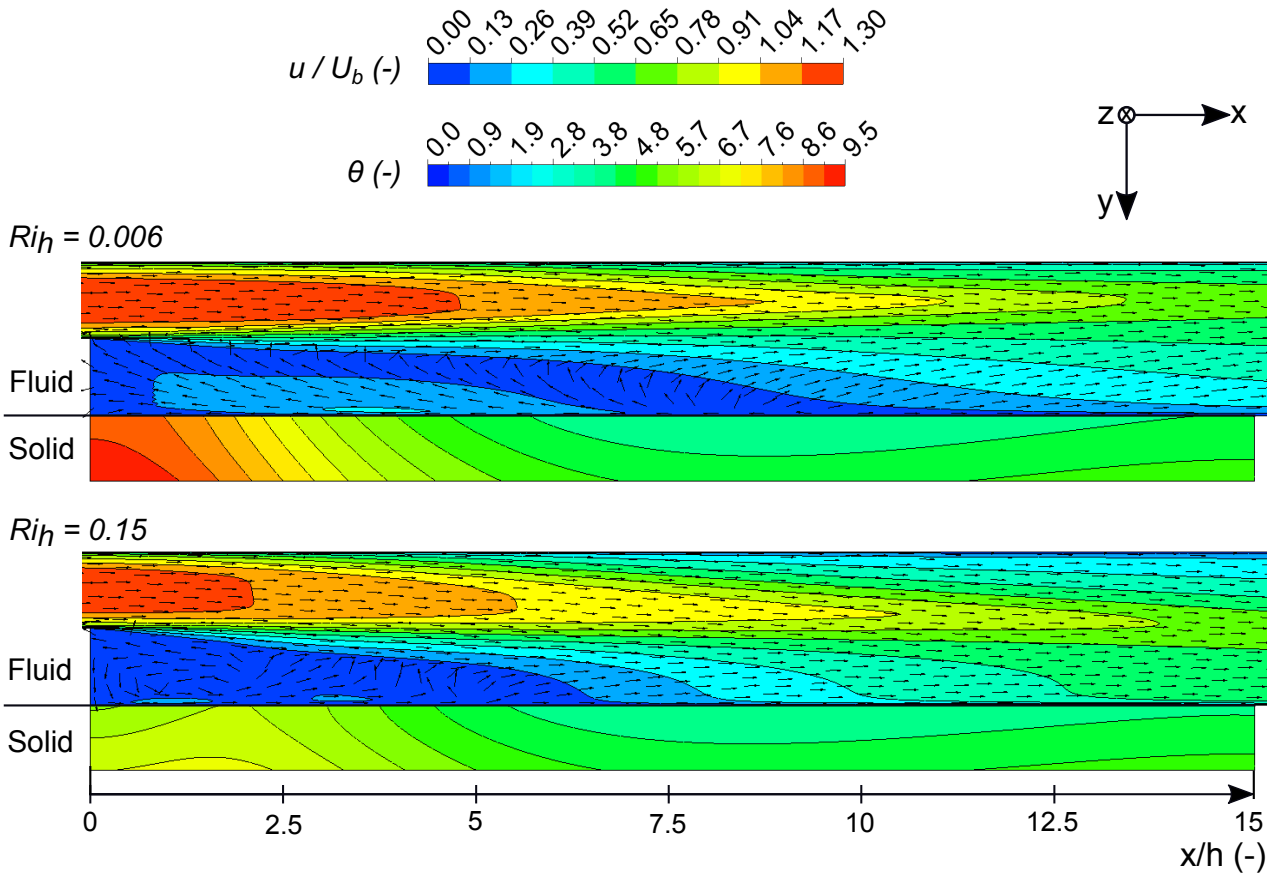


Figure 4.16: Contour plots and velocity vectors for the streamwise velocity component $u$ in the fluid domain (liquid metal) and contour plots for $\theta$ in the solid domain (heated plate) in the BFS geometry centerplane ($z/h = 0$) for $Ri_h = 0.006$ and $Ri_h = 0.15$.

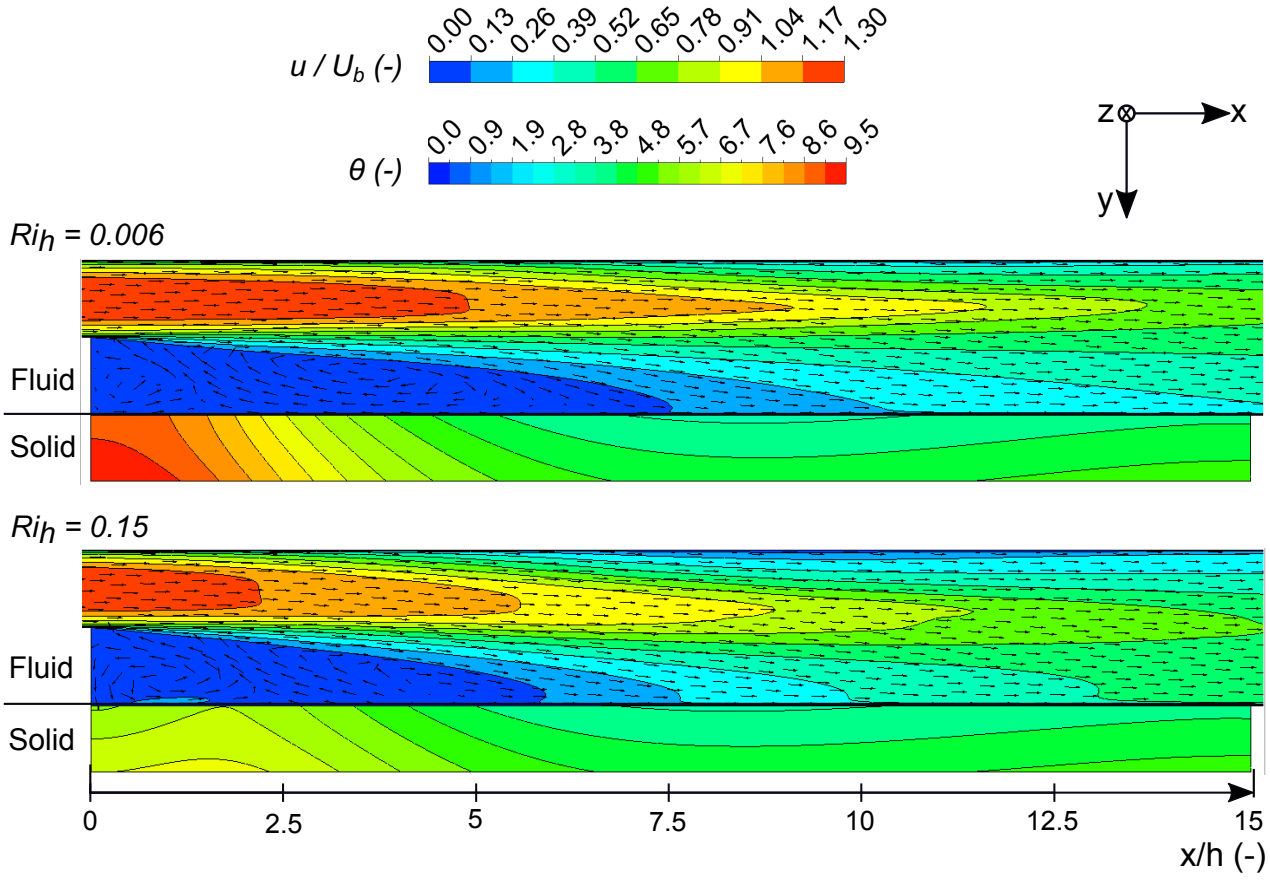


Figure 4.17: Contour plots and velocity vectors for the streamwise velocity component $u$ in the fluid domain (liquid metal) and contour plots for $\theta$ in the solid domain (heated plate) in the plane at $z/h = 0.5$ for $Ri_h = 0.006$ and $Ri_h = 0.15$.

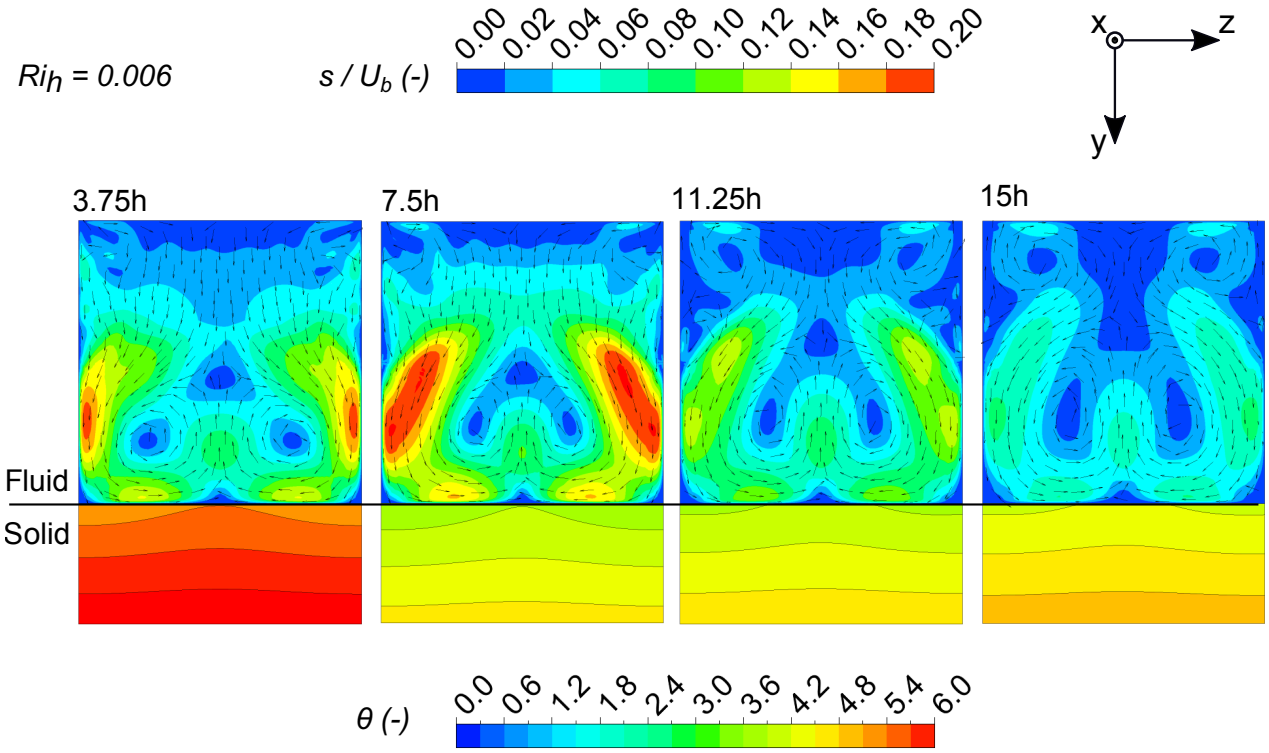


Figure 4.18: Contour plots and velocity vectors for the resultant spanwise velocity components $v$ and $w$ in the fluid domain (liquid metal) and contour plots for $\theta$ in the solid domain (heated plate) at different $x$ positions for $Ri_h = 0.006$.

see Bradshaw (1987). Secondary flow of the second kind seems to affect even the streamwise velocity component behavior, see Fig. 4.16 and 4.17. Furthermore, this turbulence induced flow explains why the high heat flux values observed in Fig. 4.13 are located at the heated plate sides. Cold fluid is transported from the bulk flow to the heated plate by eddies due to secondary flow of the second kind in addition to the streamwise the roll-up eddy. The higher heat removal towards the heated plate side is also concluded by following the heat flux path in the heated plate, as done in the previous section. Finally, the higher values for the magnitude of secondary flow of the second kin for forced convection compared to mixed convection are explained by the known stabilizing effect of convex streamline curvature on turbulence, see Pope (2000).

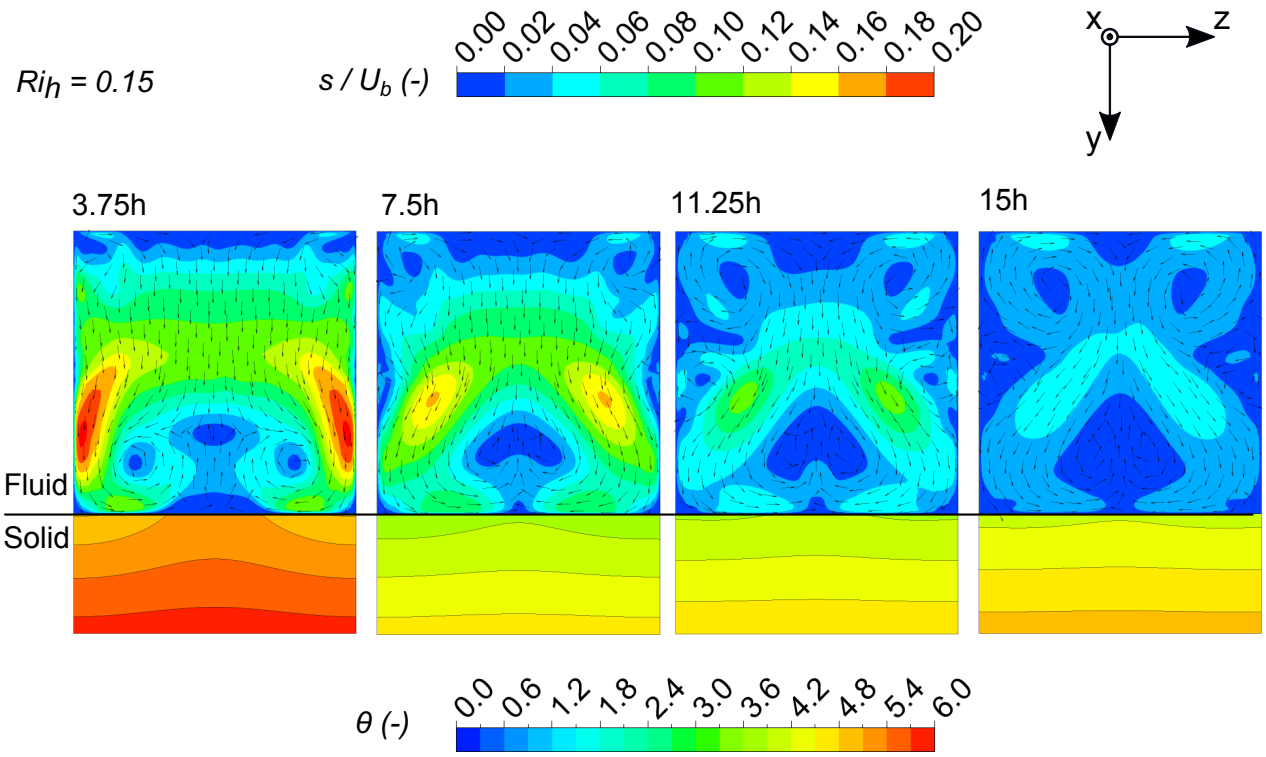


Figure 4.19: Contour plots and velocity vectors for the resultant spanwise velocity components $v$ and $w$ in the fluid domain (liquid metal) and contour plots for $\theta$ in the solid domain (heated plate) at different $x$ positions for $Ri_h = 0.15$.

# 5

# Summary

In the frame of this dissertation work, a vertical confined backward facing step (BFS) flow experiment has been designed and conducted for a low Prandtl number ($Pr$) fluid, namely, the eutectic alloy gallium-indium-tin ($GaInSn$). The experiment covers the forced convection regime with Richardson numbers $Ri_h = 0.006$, $Ri_h = 0.04$ for three Reynolds numbers $Re_h \approx 10000$, $Re_h \approx 20000$, $Re_h \approx 30000$ and the mixed convection regime with $Ri_h = 0.15$ for $Re_h \approx 10000$. For each parameter set, local velocity profiles have been measured at six positions along the test section, as well as the local Nusselt number $Nu$ distribution in the heated plate very near to the fluid-solid interface. The flow local velocity has been measured with in-house designed and developed permanent magnet probes (PMP) for which an ad hoc calibration methodology has been elaborated and implemented. The main uncertainty contributors for the velocity measurements relate to wetting issues during the calibration of the probes and to the limited samples of the repeatability study. Hence, the extended uncertainty for these measurements has been evaluated calculating the effective degrees of freedom and using the $t$-Student distribution for each data point. Numerical simulations of the Reynolds Averaged Navier-Stokes (RANS) equations have been performed to further analyze the involved conjugate heat transfer problem more and additional flow phenomena (secondary flow of the second kind) more in detail.

For the the forced convection cases ($Ri_h = 0.006$, $Ri_h = 0.04$), all measured velocity profiles are independent of the Reynolds number ($10000 \lesssim Re_h \lesssim 30000$) within experimental uncertainty and $Nu$ increases with increasing $Re_h$. Prior to the experiment, the onset of mixed convection has been estimated of order $Ri_h = O\left(10^{-2}\right)$. From the measured velocity profiles, the onset of the mixed convection

regime is measured to be of order $Ri_h = O\left(10^{-1}\right)$. A second estimate based on dimensional analysis of a simplified version of the Navier-Stokes equations matches the experimental observation in an order of magnitude sense. The onset from forced to mixed convection is not observed from the measured local $Nu$ distribution. An asymmetry of the local measured $Nu$ distribution is observed with respect to the heated plane streamwise center-plane. Although the asymmetry is hardly distinguishable from experimental uncertainty, an influence of the positioning of the sensing thermocouples on the heated plate temperature distribution cannot be excluded.

As shown from the performed numerical calculations, the heated plate local $Nu$ shows a great sensitivity on the assumed wall thermal boundary condition, i.e. on the heated plate Biot number $Bi$. The correct heated plate thermal boundary condition for this experiment is a mixed-type thermal boundary condition because $Bi \sim O\left(10^{-1}\right)$. This has an impact on the physical interpretation to be given to $Nu$ as usually defined in the context of BFS flows and its capability as an indicator to measure the BFS flow mean reattachment point $x_R$ and hence on the onset of mixed convection. Different as for BFS cases with a constant heat flux heated plate boundary condition ($Bi \gg 1$), there is no obvious relationship between $Nu$ and the mean reattachment point $x_R$ for this particular experiment. This explains why the onset to from forced to mixed convection is not observed from the measured $Nu$. Thus, conjugate heat transfer calculations are mandatory for the proper reproduction of the experiment thermal boundary condition.

Along the heated plate centerline, the numerical simulation results show one region of high heat removal for forced convection and two regions for mixed convection. A possible explanation for the single maxima for the forced convection case is the eddy roll-up phenomena. For the mixed convection case, the roll-up phenomena seems to interact with the detaching recirculation bubble due to increasing buoyancy forces. The overall heated plate heat flux maxima are located at the heated plate sides and not along its centerline, as initially expected. This can be explained with the important effect secondary flow of the second kind has on the heat transfer characteristics.

# 6

# Outlook

In this thesis only the results for the local mean velocities and Nusselt numbers are quantitatively conclusive. During the facility commissioning, unexpected technical complications regarding the suppression of external electromagnetic interference to the PMP signal arose that had to be addressed before beginning with the experiments, see in the appendix D.3. This, at the time expense of further needed optimizations to be implemented to the facility and the PMP signal postprocessing routine to measure fluctuating quantities.

Further open optimization and improvement activities to be done in the future are:

- Increase the pressure drop along the flow conditioning section to improve the inlet velocity boundary condition: the facility pump proved to reach a much higher pressure head than originally expected. The installed screens in the settling chamber can be replaced by screens with a lower mesh porosity to increase the pressure drop, hence correcting more effectively the profile tilt, as seen in Fig. 3.14. This probably due to the influence of the $90^\circ$ bend of the flow conditioning section of the facility, see Fig. 3.1. Since the flow conditioning section has been designed using a modular concept, the replacement of the screens can be realized without too much of an effort.

- Optimize the inlet thermal boundary condition: the available cooling system is underpowered and hence does not matched to the facility heat input. As a consequence, the cooling system does not work continuously, i.e. the inlet temperature stability fluctuates within $0.5^\circ C$ (peak-to-peak) in a period of $10 - 15\,min$. Since the present temperature gradients for the highest heat input are in the same order of magnitude as the inlet temperature fluctuation,

the measured mean temperature profiles $\langle T \rangle$ are distorted. If the root-mean-square value of the temperature signal $\left\langle T'^2 \right\rangle$is to be measured, a highly stable inlet temperature boundary condition is needed, as well. This can be achieve by matching both heated and cooling power by either acquiring a new cooling system that is matched to the present heat input or by increasing the heated plate heat input to the present cooling system. This is not an trivial task, since to heat a relatively small heated plate with the needed heated power is not straightforward.

– Increase the heated plate input power: complementing the last point, an increment of the heated plate power would not only help to stabilize the thermal inlet boundary condition, but also to achieve higher Richardson numbers $Ri_h$ at higher Reynolds numbers $Re_h$. This would enable the validation of the calculated onset of mixed convection at $Ri_h = O\left(10^{-1}\right)$ from scale analysis. Furthermore, this would improve the energy balance monitoring of the facility by increasing the temperature difference between the facility heat exchanger inlet and outlet above their respective experimental uncertainty.

– Extend the probe measurement equation to fluctuating quantities, i.e. velocity variance $\left\langle u'^2 \right\rangle$ and turbulent heat flux $\left\langle u' T' \right\rangle$). This task can be separted into two subtasks:

  i. A phase-shift model must be included to the probe measurement equation (Eq. 3.4) to properly correct the fluctuating signal components: to calculate fluctuating quantities from the probe measured signal $V_{SS}$, $V_{SS}$ must be first temperature corrected (see Eq. 3.4). This requires the velocity-proportional component of $V_{SS}$ to be measured *synchronously* and *in phase* with the temperature signal. Kapulla (2000) developed a phase-shift model and a calibration routine to account for this.

  ii. Re-wire the permanent magnet probe cables to be able to measure synchronously both the liquid metal velocity-proportional and the temperature signals: in its current state, the temperature and velocity signals of all permanent magnet probes are measured over separate measurement chains (see Fig. 3.9). This is not a problem for the measurement of mean quantities. However, for the measurement of $\left\langle u'^2 \right\rangle$ and/or of $\left\langle u' T' \right\rangle$, both signals must be neccessarily measured synchronously. This can be achieved for the current measurement chain only by re-wiring the ther-

mocouple connectors. This can be only done for one probe, since the measurement chain for the velocity signals (LTT24 measurement system) has a limited amount of input channels.

- The mentioned modifications in the previous point would also enable the analysis of the BFS flow by means of wavelet analysis, i.e. the time-dependent spectral analysis of the flow. It may be interesting to study whether the onset of mixed convection can be characterized by an energy shift in the turbulent spectrum. For an introduction to wavelet analysis and the general detection of turbulent coherent structures see Farge (1992), Farge *et al.* (1996) and Addison (2017).

- To calculate the local distribution of the specific heat flux $\dot{q}$ along the heated plate as proposed by Woodfield *et al.* (2006). This is likely to be the reason for the discrepancy between the measured local Nusselt number $Nu$ and the observed behavior for this variable in DNS simualtions from the literature (Niemann & Fröhlich (2016b)).

- Further design recommendations for BFS test sections for *GaInSn* experiments are made in the appendix D.2.

- Perform a systematic experimental study on wetting capabilities of *GaInSn* on different surfaces (metals and plastics) cleaned with different hydrocarbons (heptane, iso-propanol, etc.).

- Extend the sophisticated analysis made by Kapulla (2000) with Green's functions for measurement equation derivation for a spherical magnetic dipole with the results presented by Caciagli *et al.* (2018) for a cylindrical magnet.

# Bibliography

ADDISON, P.S. 2017. *The Illustrated Wavelet Transform Handbook: Introductory Theory and Applications in Science, Engineering, Medicine and Finance*. 2nd edn. Boca Raton: CRC press. ISBN: 9781315372556.

BAILLY, C., & COMTE-BELLOT, G. 2015. *Turbulence*. 1st edn. Heidelberg New York Dordrecht London: Springer International Publishing Switzerland. ISBN: 9783319161594.

BARLOW, J.B., RAE, W.H., & POPE, A. 1999. *Low speed wind tunnel testing*. 3rd edn. New York: Wiley. ISBN: 0-471-55774-9.

BATCHELOR, G.K. 1967. *An Introduction to Fluid Dynamics*. 1st edn. Cambridge: Cambridge University Press. ISBN: 9780521663960.

BEJAN, A. 2013. *Convection Heat Transfer*. 4th edn. Hoboken (NJ): John Wiley & Sons. ISBN: 9780470900376.

BELL, JAMES H, & MEHTA, RABINDRA D. 1988. *Contraction Design for Small Low-Speed Wind Tunnels*. Tech. rept. NASA-CR-177488. Ames Research Center, NASA.

BELL, J.H, & MEHTA, R.D. 1989. *Design and Calibration of the Mixing Layer and Wind Tunnel*. Tech. rept. NAS 1.26:185472. Ames Research Center, NASA.

BENTLEY, ROBIN E. 1998. *Handbook of Temperature Measurement*. Vol. Vol. 3: The theory and practice of thermoelectric thermometry. Singapore: Springer Science & Business Media. ISBN: 9814021113.

BLEVINS, R.D. 1984. *Applied Fluid Dynamics Handbook*. Malabar (FL): Krieger Publishing Company. ISBN: 9780442212964.

BRADSHAW, P. 1971. *An Introduction to Turbulence and its Measurement*. 1st edn. Oxford: Pergamon Press. ISBN: 9780080166216.

BRADSHAW, P. 1987. Turbulent Secondary Flows. *Annual Review of Fluid Mechanics*, **19**(1), 53–74. doi: https://doi.org/10.1146/annurev.fl.19.010187.000413.

BRADSHAW, P., & PANKHURST, R.C. 1964. The Design of Low-Speed Wind Tunnels. *Progress in Aerospace Sciences*, **5**, 1–69. doi: https://doi.org/10.1016/0376-0421(64)90003-X.

BRADSHAW, P., & WONG, F.Y.F. 1972. The Reattachment and Relaxation of a Turbulent Shear Layer. *Journal of Fluid Mechanics*, **52**(1), 113–135. doi: https://doi.org/10.1017/S002211207200299X.

BUCHENAU, D. 2012. *Entwicklung von Kontaktlosen und Zeitlich Hochauflösenden Strömungs- und Durchflusssensoren für Flüssigmetallströmungen*. Ph.D. thesis, Karlsruhe Institute of Technology, Department of Mechanical Engineering, Karlsruhe.

BUCKINGHAM, S. 2018. *Prandtl Number Effects in Abruptly Separated Flows: LES and Experiments on an Unconfined Backward Facing Step Flow*. Ph.D. thesis, Université Catholique de Louvain, Louvain.

CACIAGLI, A., BAARS, R.J., PHILIPSE, A.P., & KUIPERS, B..W.M. 2018. Exact Expression for the Magnetic Field of a Finite Cylinder with Arbitrary Uniform Magnetization. *Journal of Magnetism and Magnetic Materials*, **456**, 423–432. doi: https://doi.org/10.1016/j.jmmm.2018.02.003.

CADWALLADER, L.C. 2003. Gallium Safety in the Laboratory. *In: Energy Facility Contractors Group (EFCOG) Safety Analysis Working Group (SAWG) 2003 Annual Meeting, Salt Lake City, UT (US), 21–27.06.2003*. OSTI Identifier: 811932.

CATTAFESTA, L., BAHR, C., & MATHEW, J. 2010. *Encyclopedia of Aerospace Engineering*. Wiley Online Library. ISBN: 9780470686652. Chap. Fundamentals of Wind-Tunnel Design.

CEBECI, T., & BRADSHAW, P. 1984. *Physical and Computational Aspects of Convective Heat Transfer*. New York: Springer Verlag. ISBN: 9780387968216.

CHEN, L., ASAI, K., NONOMURA, T., XI, G., & LIU, T. 2018. A review of Backward-Facing Step Flow Mechanisms, Heat Transfer and Control. *Thermal Science and Engineering Progress*, **6**, 194–216. doi: https://doi.org/10.1016/j.tsep.2018.04.004.

CHOVET, C., LIPPERT, M., FOUCAUT, J.M., & KEIRSBULCK, L. 2017. Dynamical aspects of a backward-facing step flow at large Reynolds numbers. *Experiments in Fluids*, **58**(11), 1–15. doi: https://doi.org/10.1007/s00348-017-2444-5.

COCHRAN, D.L, & KLINE, S.J. 1958. *The Use of Short Flat Vanes for Producing Efficient Wide-Angle Two-Dimensional Subsonic Diffusers*. Tech. rept. NACA-TN-4309. National Advisory Committee for Aeronautics. NACA Technical Notes.

COLLAR, A.R. 1936. *Some Experiments with Cascades of Aerofoils*. Tech. rept. Air Ministry, Aeronautical Research Committee, Reports and Memoranda: 1768. N.P.L.

CRAMER, A., VARSHNEY, K., GUNDRUM, T., & GERBETH, G. 2006. Experimental Study on the Sensitivity and Accuracy of Electric Potential Local Flow Measurements. *Flow Measurement and Instrumentation*, **17**(1), 1–11.

DA VIA, R., & MANSERVISI, S. 2019. Numerical Simulation of Forced and Mixed Convection Turbulent Liquid Sodium Flow Over a Vertical Backward Facing Step with a Four Parameter Turbulence Model. *International Journal of Heat and Mass Transfer*, **135**, 591–603. doi: https://doi.org/10.1016/j.ijheatmasstransfer.2019.01.129.

DAVIDSON, P.A. 2015. *Turbulence : An Introduction for Scientists and Engineers*. 2nd edn. Oxford: Oxford University Press. ISBN: 9780198722595.

DAVIDSON, P.A. 2017. *An Introduction to Magnetohydrodynamics*. 2nd edn. Cambridge: Cambridge University Press. ISBN: 9781316613023.

DE BREDERODE, V.A.S.L., & BRADSHAW, P. 1972. *Three-dimensional Flow in Nominally Two-dimensional Separation Bubbles: Flow Behind a Rearward-Facing Step I.* Tech. rept. I.C. Aero Report, 72-19. Imperial College of Science and Technology.

DE LOS RIOS RAMOS, N. DIEZ, HERING, W., WEISENBURGER, A., STÜBER, M., ONEA, A., LUX, M., ULRICH, S., & STIEGLITZ, R. 2017. Design and construction of the ATEFA facility for experimental investigations of AMTEC test modules. *Page 012014 of: IOP Conference Series: Materials Science and Engineering*, vol. 228. IOP Publishing.

DE SANTIS, A., & SHAMS, A. 2018. Application of an Algebraic Turbulent Heat Flux Model to a Backward Facing Step flow at low Prandtl number. *Annals of Nuclear Energy*, **117**, 32–44. doi: https://doi.org/10.1016/j.anucene.2018.03.016.

DUPONCHEEL, M., BRICTEUX, L., MANCONI, M., WINCKELMANS, G., & BARTOSIEWICZ, Y. 2014. Assessment of RANS and improved near-wall modeling for forced convection at low Prandtl numbers based on LES up to $Re_\tau = 2000$. *International Journal of Heat and Mass Transfer*, **75**, 470–482. doi: https://doi.org/10.1016/j.ijheatmasstransfer.2014.03.080.

EAKER, COLLIN B, & DICKEY, MICHAEL D. 2016. Liquid Metal Actuation by Electrical Control of Interfacial Tension. *Applied Physics Reviews*, **3**(3), 031103. doi: https://doi.org/10.1063/1.4959898.

EMMENDÖRFER, FRANZISKA. 2015. *Bestimmung des Wärmeübergangs in einer Glattrohrmessstrecke bei Durchströmung mit Flüssigmetall*. Bachelor Thesis. Karlsruhe Institute of Technology, Department of Chemical and Process Engineering, Karlsruhe.

FARELL, C., & YOUSSEF, S. 1996. Experiments on Turbulence Management Using Screens and Honeycombs. *Journal of Fluids Engineering*, **118**(1), 26–32. doi: https://doi.org/10.1115/1.2817505.

FARGE, M. 1992. Wavelet Transforms and their Applications to Turbulence. *Annual Review of Fluid Mechanics*, **24**(1), 395–458. doi: https://doi.org/10.1146/annurev.fl.24.010192.002143.

FARGE, M., KEVLAHAN, N., PERRIER, V., & GOIRAND, E. 1996. Wavelets and Turbulence. *Proceedings of the IEEE*, **84**(4), 639–669. doi: https://doi.org/10.1109/5.488705.

FEIL, O.G. 1964. Vane Systems for Very-Wide-Angle Subsonic Diffusers. *Journal of Basic Engineering*, **86**(4), 759–764. doi: https://doi.org/10.1115/1.3655946.

FENTON, A.W. 1980. How do Thermocouples Work. *Nuclear Energy*, **19**(1), 61–63. ISSN 0140-4067.

FERZIGER, J.H., & PERIC, M. 2008. *Numerische Strömungsmechanik*. Berlin Heidelberg: Springer-Verlag. ISBN: 9783540682288.

FEYNMAN, R.P., LEIGHTON, R.B., & SANDS, M. 2010. *The Feynman Lectures on Physics*. New millennium edn. Vol. 2. New York: Basic Books. Originally published 1963-1965, IBAN: 9780465024940.

GEDDIS, P., WU, L., MCDONALD, A., CHEN, S., & CLEMENTS, B. 2020. Effect of Static Liquid Galinstan on Common Metals and Non-Metals at Temperatures up to 200°C. *Canadian Journal of Chemistry*, **98**(12), 787–798. doi: https://doi.org/10.1139/cjc-2020-0227.

GEORGE, W.K. 1990. Governing equations, experiments, and the experimentalist. *Experimental Thermal and Fluid Science*, **3**(6), 557–566. doi: https://doi.org/10.1016/0894-1777(90)90071-E.

GEORGE, W.K. 2009. *An Introduction to Natural Convection Flows*. Open source. Available online at http://www.turbulence-online.com/ - last accessed on 25.01.2019.

GEORGE, W.K. 2013. *Lectures in Turbulence for the 21st Century*. Open source. Available online at http://www.turbulence-online.com/ - last accessed on 25.01.2019.

GRAY, D.D, & GIORGINI, A. 1976. The Validity of the Boussinesq Approximation for Liquids and Gases. *International Journal of Heat and Mass Transfer*, **19**(5), 545–551. doi: https://doi.org/10.1016/0017-9310(76)90168-X.

GROTH, J., & JOHANSSON, A.V. 1988. Turbulence Reduction by Screens. *Journal of Fluid Mechanics*, **197**, 139–155. doi: https://doi.org/10.1017/S0022112088003209.

GRÖTZBACH, G. 2013. Challenges in low-Prandtl Number Heat Transfer Simulation and Modelling. *Nuclear Engineering and Design*, **264**, 41 – 55. doi: https://doi.org/10.1016/j.nucengdes.2012.09.039.

HANCOCK, P.E., & JOHNSON, A.E. 1997. Close Spacing of Settling Chamber Screens. *The Aeronautical Journal*, **101**(1004), 179–183. doi: https://doi.org/10.1017/S0001924000066525.

HANJALIC, K., & LAUNDER, B. 2011. *Modelling Turbulence in Engineering and the Environment: Second-Moment Routes to Closure*. Cambridge: Cambridge University Press. IBAN: 9780521845755.

HEINZEL, A., HERING, W., KONYS, J., MAROCCO, L., LITFIN, K., MÜLLER, G., PACIO, J., SCHROER, C., STIEGLITZ, R., STOPPEL, L., WEISENBURGER, A., & WETZEL, T. 2017. Liquid Metals as Efficient High-Temperature Heat-Transport Fluids. *Energy Technology*, **5**(7), 1026–1036. doi: https://doi.org/10.1002/ente.201600721.

IDELCHIK, I.E. 2007. *Handbook of Hydraulic Resistance*. 4th edn. New York: Begell House. ISBN: 9781567002515.

INCROPERA, F.P., DEWITT, D.P., BERGMAN, T.L., & LAVINE, A.S. 2017. *Principles of Heat and Mass Transfer*. 8th international edition edn. Singapore: Wiley. ISBN: 9781119382911.

JCGM. 100:2008, 2008. *Guide to the Expression of Uncertainty in Measurement. Joint Committee for Guides in Metrology. Paris: Bureau International des Poids et Mesures.*

JISCHA, M. 1982. *Konvektiver Impuls-, Wärme-und Stoffaustausch*. Wiesbaden: Vieweg+Teubner Verlag. ISBN: 3528081449.

JOHANSSON, A. 1992. A Low Speed Wind-Tunnel with Extreme Flow Quality - Design and Tests. *Pages 1603–1611 of: ICAS Proceedings, 18th Congress, Beijing, China*. IBAN: 1563470462.

JOHL, G., PASSMORE, M., & RENDER, P. 2007. Design and Performance of Thin, Circular Arc, Wind-tunnel Turning Vanes. *The Aeronautical Journal*, **111**(1116), 115–118. doi: https://doi.org/10.1017/S0001924000001810.

KADER, B.A. 1981. Temperature and Concentration Profiles in Fully Turbulent Boundary Layers. *International Journal of Heat and Mass Transfer*, **24**(9), 1541–1544. doi: https://doi.org/10.1016/0017-9310(81)90220-9.

KAKAC, S. (ed). 1987. *Handbook of Single-Phase Convective Heat Transfer*. 1st edn. New York: Wiley. ISBN: 0471817023.

KAPULLA, R. 2000. *Experimentelle Untersuchung von thermisch stratifizierten und unstratifizierten Mischungsschichten in Natrium und Wasser*. Ph.D. thesis, ETH Zürich, Department of Mechanical and Process Engineering, ZÃŒrich. doi: https://doi.org/10.3929/ethz-a-003883663.

KAPULLA, R., SIGG, B., HORANYI, S., & HUDINA, M. 2000. Local Velocity Measurements in a Thermally-Stratified Sodium Mixing Layer Using a Permanent-Magnet Probe. *Experimental Thermal and Fluid Science*, **20**(3-4), 115–136. doi: https://doi.org/10.1016/S0894-1777

KASAGI, N., KURODA, K., & HIRATA, M. 1989. Numerical Investigation of Near-Wall Turbulent Heat Transfer Taking Into Account the Unsteady Heat Conduction in the Solid Wall. *Journal of Heat Transfer*, **111**(2), 385–392. doi: https://doi.org/10.1115/1.3250689.

KASAP, S.O. 2017. *Principles of Electronic Materials and Devices*. 4th edn. New York: McGraw-Hill. ISBN: 9780078028182.

KAYS, W.M., CRAWFORD, M.E., & WEIGAND, B. 2007. *Convective heat and mass transfer*. 4th edn. Boston: McGraw-Hill. ISBN: 0071238298.

KENJERES, S., GUNARJO, S.B., & HANJALIC, K. 2005. Contribution to Elliptic Relaxation Modelling of Turbulent Natural and Mixed Convection. *International Journal of Heat and Fluid Flow*, **26**(4), 569–586. https://doi.org/10.1016/j.ijheatfluidflow.2005.03.007.

KLINE, S.J. 1969. *Film notes for Flow Visualization*. National committee for fluid mechanics films. Massachusetts (MA): MIT Press. URL: http://web.mit.edu/hml/ncfmf/01ELDFM.pdf - last accessed on 25.01.2019.

KNEBEL, J.U., & KREBS, L. 1993. *Kalibrierung einer Miniatur-Permanentmagnet-Potentialsonde zur Geschwindigkeits- und Temperaturmessung in Natrium*. Tech. rept. KfK 5215. Kernforschungszentrum Karlsruhe, Karlsruhe. doi: https://doi.org/10.5445/IR/270034481.

KNEBEL, J.U., KREBS, L., MÜLLER, U., & AXCELL, B.P. 1998. Experimental Investigation of a Confined Heated Sodium Jet in a Co-Flow. *Journal of Fluid Mechanics*, **368**, 51–79. doi: https://doi.org/10.1017/S0022112098001463.

KUNDU, P.K., COHEN, I.M., & DOWLING, D.R. 2016. *Fluid mechanics*. 6th edn. Amsterdam: Elsevier, Academic Press. ISBN: 9780124059351.

KURIAN, T., & FRANSSON, J.H.M. 2009. Grid-generated Turbulence Revisited. *Fluid Dynamics Research*, **41**(2), 021403. doi: http://dx.doi.org/10.1088/0169-5983/41/2/021403.

LAI, W.M., RUBIN, D.H., & KREMPL, E. 2009. *Introduction to Continuum Mechanics*. 4th edn. Oxford: Butterworth-Heinemann. ISBN: 9780750658603.

LANDAU, L.D., & LIFSHITZ, E.M. 1987. *Fluid Mechanics*. Vol. 6. New York: Pergamon. ISBN: 0080339328.

LAWS, E.M. 1990. Flow conditioning - A new development. *Flow Measurement and Instrumentation*, **1**(3), 165–170. doi: https://doi.org/10.1016/0955-5986(90)90006-S.

LAWS, E.M., & LIVESEY, J.L. 1978. Flow Through Screens. *Annual review of fluid mechanics*, **10**(1), 247–266. doi: https://doi.org/10.1146/annurev.fl.10.010178.001335.

LE, H., MOIN, P., & KIM, J. 1997. Direct numerical simulation of turbulent flow over a backward-facing step. *Journal of fluid mechanics*, **330**, 349–374. doi: https://doi.org/10.1017/S0022112096003941.

LEMMON, E.W., BELL, I.H., HUBER, M.L., & MCLINDEN, M.O. 2022. *NIST Chemistry WebBook, NIST Standard Reference Database Number 69*. Gaithersburg MD: National Institute of Standards and Technology. DOI: https://doi.org/10.18434/T4D303, (retrieved January 15, 2022). Chap. Thermophysical Properties of Fluid Systems.

LESCHZINER, M. 2015. *Statistical Turbulence Modelling for Fluid Dynamics - Demystified. An Introductory Text For Graduate Engineering Students*. London: Imperial College Press. ISBN: 9781783266616.

LI, X., & DJILALI, N. 1995. On the Scaling of Separation Bubbles. *JSME International Journal Series B Fluids and Thermal Engineering*, **38**(4), 541–548.

LINDGREN, B., & JOHANSSON, A.V. 2002. *Design and Evaluation of a Low-Speed Wind-Tunnel with Expanding Corners*. Tech. rept. TRITA-MEK2002:14. KTH, Dept. of Mechanics.

LINDGREN, B., ÖSTERLUND, J., & JOHANSSON, A.V. 1998. Measurement and Calculation of Guide Vane Performance in Expanding Bends for Wind-tunnels. *Experiments in Fluids*, **24**(3), 265–272. doi: https://doi.org/10.1007/s003480050173.

LLOYD, J.R., & SPARROW, E.M. 1970. Combined Forced and Free Convection Flow on Vertical Surfaces. *International Journal of Heat and Mass Transfer*, **13**(2), 434–438. doi: https://doi.org/10.1016/0017-9310(70)90119-5.

LOEHRKE, R.I., & NAGIB, H.M. 1972. *Experiments on Management of Free-stream Turbulence*. Tech. rept. AD0749891. Illinois Institute of Technology, Chicago.

LUMLEY, J. 1969. *Film notes for eulerian and lagrangian descriptions in fluid mechanics*. National committee for fluid mechanics films. Massachusetts (MA): MIT Press. URL: http://web.mit.edu/hml/ncfmf/01ELDFM.pdf - last accessed on 25.01.2019.

MA, X., & SCHRÖDER, A. 2017. Analysis of flapping motion of reattaching shear layer behind a two-dimensional backward-facing step. *Physics of Fluids*, **29**(11), 115104. doi: https://doi.org/10.1063/1.4996622.

MA, X., TANG, Z., & JIANG, N. 2020. Eulerian and Lagrangian analysis of coherent structures in separated shear flow by time-resolved particle image velocimetry. *Physics of Fluids*, **32**(6), 065101. doi: https://doi.org/10.1063/5.0008664.

MEHTA, R.D., & BRADSHAW, P. 1979. Design rules for small low speed wind tunnels. *The Aeronautical Journal*, **83**(827), 443–453. doi: https://doi.org/10.1017/S0001924000031985.

MERKER, G.P. 1987. *Konvektive Wärmeübertragung*. Berlin Heidelberg: Springer-Verlag. ISBN: 9783642828904.

MIKHAIL, M.N. 1979. Optimum Design of Wind Tunnel Contractions. *AIAA journal*, **17**(5), 471–477. doi: https://doi.org/10.2514/3.61157.

MOFFAT, R.J. 1988. Describing the uncertainties in experimental results. *Experimental Thermal and Fluid Science*, **1**(1), 3–17. doi: https://doi.org/10.1016/0894-1777(88)90043-X.

MOFFAT, R.J. 1998. What's new in convective heat transfer? *International Journal of Heat and Fluid Flow*, **19**(2), 90–101.

MONIN, A.S., & YAGLOM, A.M. 1971. *Statistical Fluid Mechanics*. 1st edn. Vol. 1. Mineola: Dover. ISBN: 9780486458830.

MONIN, A.S., & YAGLOM, A.M. 1975. *Statistical Fluid Mechanics*. 1st edn. Vol. 2. Mineola: Dover. ISBN: 9780486458915.

MORLEY, N.B., BURRIS, J., CADWALLADER, L.C., & NORNBERG, M.D. 2008. GaInSn Usage in the Research Laboratory. *Review of Scientific Instruments*, **79**(5), 056107. doi: https://doi.org/10.1063/1.2930813.

NADGE, P.M., & GOVARDHAN, R.N. 2014. High Reynolds Number Flow Over a Backward-Facing Step: Structure of the Mean Separation Bubble. *Experiments in Fluids*, **55**(1), 1657. doi: https://doi.org/10.1007/s00348-013-1657-5.

NIEMANN, M. 2017. *Buoyancy Effects in Turbulent Liquid Metal Flow: a Study in Square Channels and Behind Sudden Expansions*. Ph.D. thesis, TU Dresden, Dresden. ISBN: I9783959081238.

NIEMANN, M., & FRÖHLICH, J. 2016a. Budgets of temperature fluctuations in buoyancy-affected turbulent backward-facing step flows at low Prandtl number. 11th International ERCOFTAC Symposium on Engineering Turbulence Modelling and Measurements, Palermo, Italy, 21-23 September 2016. doi: no doi.

NIEMANN, M., & FRÖHLICH, J. 2016b. Buoyancy-affected backward-facing step flow with heat transfer at low Prandtl number. *International Journal of Heat and Mass Transfer*, **101**, 1237–1250.

NIEMANN, M., & FRÖHLICH, J. 2017. Turbulence Budgets in Buoyancy-affected Vertical Backward-facing Step Flow at Low Prandtl Number. *Flow, Turbulence and Combustion*, **99**(3), 705–728. doi: https://doi.org/10.1007/s10494-017-9862-6.

NIKITIN, N.V., PIMANOV, V.O., & POPELENSKAYA, N.V. 2019. Mechanism of formation of Prandtl secondary flows of the second kind. *Russian Academy of Sciences Section Mechanics*, **64**(2), 61–65. doi: https://doi.org/10.1134/S1028335819020034.

ODER, J., A.SHAMS, CIZELJ, L., & TISELJ, I. 2019. Direct Numerical Simulation of Low-Prandtl Fluid Flow Over a Confined Backward Facing Step. *International Journal of Heat and Mass Transfer*, **142**, 118436. doi: https://doi.org/10.1016/j.ijheatmasstransfer.2019.118436.

OECD/NEA. 2015. *Handbook on Lead-bismuth Eutectic Alloy and Lead Properties, Materials Compatibility, Thermal-hydraulics and Technologies*. Tech. rept. NEA No. 7268. Paris: OECD.

PACIO, J., MAROCCO, L., & WETZEL, T. 2015. Review of Data and Correlations for Turbulent Forced Convective Heat Transfer of Liquid Metals in Pipes. *Heat and Mass Transfer*, **51**(2), 153–164. doi: https://doi.org/10.1007/s00231-014-1392-3.

PINELLI, A., UHLMANN, M., SEKIMOTO, A., & KAWAHARA, G. 2010. Reynolds number dependence of mean flow structure in square duct turbulence. *Journal of Fluid Mechanics*, **644**, 107–122.

PLEVACHUK, Y., , SKLYARCHUK, V., ECKERT, S., GERBETH, G., & NOVAKOVIC, R. 2014. Thermophysical Properties of the Liquid Ga–In–Sn Eutectic Alloy. *Journal of Chemical & Engineering Data*, **59**(3), 757–763. doi: 10.1021/je400882q.

PONT-VÍLCHEZ, A., TRIAS, F.X., GOROBETS, A., & OLIVA, A. 2019. Direct numerical simulation of backward-facing step flow at and expansion ratio 2. *Journal of Fluid Mechanics*, **863**, 341–363. doi: https://doi.org/10.1017/jfm.2018.1000.

POPE, S.B. 2000. *Turbulent Flows*. 1st edn. Cambridge: Cambridge University Press. ISBN: 9780521598866.

PRANDTL, L., OSWATITSCH, K., & WIEGHARDT, K. 1969. *Führer durch die Strömungslehre*. 7te überarbeitete auflage edn. Braunschweig: Vieweg. ISBN: not available. PPN: 011042001.

PURCELL, E.M., & MORIN, D.J. 2013. *Electricity and Magnetism*. 3rd edn. Cambridge: Cambridge University Press. IBAN: 9781107014022.

ROACH, P.E. 1987. The Generation of Nearly Isotropic Turbulence by Means of Grids. *International Journal of Heat and Fluid Flow*, **8**(2), 82–92. doi: https://doi.org/10.1016/0142-727X(87)90001-4.

ROELOFS, F., & SHAMS, A. 2019. CFD-Introduction. *Chap. 6, pages 213 – 218 of:* ROELOFS, FERRY (ed), *Thermal Hydraulics Aspects of Liquid Metal Cooled Nuclear Reactors*. Duxford: Woodhead Publishing. ISBN: 9780081019801.

ROELOFS, F., , SHAMS, A., OTIC, I., BÖTTCHER, M., DUPONCHEEL, M., BARTOSIEWICZ, Y., LAKEHAL, D., E.BAGLIETTO, LARDEAU, S., & CHENG, X. 2015. Status and Perspective of Turbulence Heat Transfer Modelling for the Industrial Application of Liquid Metal Flows. *Nuclear Engineering and Design*, **290**, 99–106. doi: https://doi.org/10.1016/j.nucengdes.2014.11.006.

SCHAUB, T., WÜSTLING, S., KONRAD, J., & TASLER, M. 2021. Design and calibration of permanent magnet probes for the local measurement of velocity and temperature in a liquid metal backward facing step flow. *Experiments in Fluids*, **62(210)**. doi: https://doi.org/10.1007/s00348-021-03293-6.

SCHAUB, T., ARBEITER, F., HERING, W., & STIEGLITZ, R. 2022. Forced and mixed convection experiments in a confined vertical backward facing step at low- Prandtl number. *Experiments in Fluids*, **63(19)**. doi: https://doi.org/10.1007/s00348-021-03363-9.

SCHLICHTING, H., & GERSTEN, K. 2017. *Boundary-Layer Theory*. 9th edn. Berlin, Heidelberg: Springer. ISBN: 9783662529195.

SCHUMM, T., FROHNAPFEL, B., & MAROCCO, L. 2018. Investigation of a Turbulent Convective Buoyant Flow of Sodium Over a Backward-facing Step. *Heat and Mass Transfer*, **54**(8), 2533–2543. doi: https://doi.org/10.1007/s00231-017-2102-8.

SHAMS, A., SANTIS, A. DE, KOLOSZAR, L.K., ORTIZ, A. VILLA, & NARAYANAN, C. 2019. Status and Perspectives of Turbulent Heat Transfer Modelling in Low-Prandtl Number Fluids. *Nuclear Engineering and Design*, **353**, 110220. doi: https://doi.org/10.1016/j.nucengdes.2019.110220.

SOBOLEV, V. 2011. *Database of Thermophysical Properties of Liquid Metal Coolants for GEN-IV*. Tech. rept. BLG–1069. Belgian Nuclear Research Center SCK-CEN. ISSN: 13792407.

STAR, S., STABILE, G., ROZZA, G., & DEGROOTE, J. 2021. A POD-Galerkin Reduced Order Model of a Turbulent Convective Buoyant Flow of Sodium Over

a Backward-facing Step. *Applied Mathematical Modelling*, **89**, 486–503. doi: https://doi.org/10.1016/j.apm.2020.07.029.

STEINER, C. 2019. *Skalenaufgelöste Simulation eines Backward Facing Step Experiments*. Master thesis, Karlsruhe Institute of Technology, Department of Chemical and Process Engineering, Karlsruhe.

STEPHAN, P., KABELAC, S., KIND, M., MEWES, D., SCHABER, K., & WETZEL, T. (eds). 2019. *VDI-Wärmeatlas*. 12 edn. Berlin, Heidelberg: Springer Vieweg. ISBN: 978-3-662-52990-4, doi: https://doi.org/10.1007/978-3-662-52989-8.

STRAUB, S., FOROOGHI, P., MAROCCO, L., WETZEL, T., VINUESA, R., SCHLATTER, P., & FROHNAPFEL, B. 2019. The influence of thermal boundary conditions on turbulent forced convection pipe flow at two Prandtl numbers. *International Journal of Heat and Mass Transfer*, **144**, 118601.

TAN-ATICHAT, J., NAGIB, H.M., & LOEHRKE, R.I. 1982. Interaction of Free-stream Turbulence with Screens and Grids: a Balance Between Turbulence Scales. *Journal of Fluid Mechanics*, **114**, 501–528. doi: https://doi.org/10.1017/S0022112082000275.

TENNEKES, H., & LUMLEY, J.L. 1972. *A First Course in Turbulence*. Massachussetts: MIT press. ISBN: 9780262200196.

TIHON, J., PENKAVOVA, V., & PANTZALI, M. 2010. The effect of Inlet Pulsations on the Backward-facing Step Flow. *European Journal of Mechanics - B/Fluids*, **29**(3), 224–235. doi: https://doi.org/10.1016/j.euromechflu.2010.02.001.

TRIMBORN, F. 2018. *Wärmeflussmodellierung turbulenter Kanalströmungen bei niedrigen Prandtl-Zahlen*. Ph.D. thesis, Karlsruher Institut für Technologie, Department of Mechanical Engineering, Karlsruhe. doi: 10.5445/IR/1000078371.

TROPEA, C., ALEXANDER, L.Y., & FOSS, J.F. (eds). 2007. *Springer Handbook of Experimental Fluid Mechanics*. Berlin, Heidelberg: Springer. ISBN: 9783540302995.

VINUESA, R., SCHLATTER, P., & NAGIB, H.M. 2018. Secondary Flow in Turbulent Ducts with Increasing Aspect Ratio. *Physical Review Fluids*, **3**(5), 054606. doi: https://doi.org/10.1103/PhysRevFluids.3.054606.

VON WEISSENFLUH, T.H. 1984. *Turbulenter Wärmetransport in flüssigem Natrium*. Ph.D. thesis, ETH Zürich.

VON WEISSENFLUH, T.H. 1985. Probes for Local Velocity and Temperature Measurements in Liquid Metal Flow. *International Journal of Heat and Mass Transfer*, **28**(8), 1563–1574. doi: https://doi.org/10.1016/0017-9310(85)90258-3.

VON WEISSENFLUH, T.H., & SIGG, B. 1987. Experience with Permanent Magnet Probes for the Measurement of Local Velocities in Liquid Metals. *Pages 61–81 of: Progress in Astronautics and Aeronautics, Technical Papers from the Proceedings of the Fifth Beer-Sheva International Seminar on Magnetohydrodynamic Flows and Turbulence, Ben-GurionUniversity of the Negev, Beer-Sheva, Israel, 2-6.03.1987*, vol. 111.

WANG, C., ZHAO, P., LEI, M., LU, K., GE, Z., LIU, J., LI, Y., & PEI, G. 2020. DNS of Instantaneous Behavior in Turbulent Forced and Mixed Convection of Liquid Metal Past a Backward-Facing Step. *Flow, Turbulence and Combustion*, **107**, 125–147. doi: https://doi.org/10.1007/s10494-020-00214-1.

WOODFIELD, P.L., MONDE, M., & MITSUTAKE, Y. 2006. Improved Analytical Solution for Inverse Heat Conduction Problems on Thermally Thick and Semi-infinite Solids. *International Journal of Heat and Mass Transfer*, **49**(17), 2864–2876. doi: https://doi.org/10.1016/j.ijheatmasstransfer.2006.01.050.

ZHAO, P., WANG, C., GE, Z., ZHU, J., LIU, J., & YE, M. 2018a. DNS of Turbulent Mixed Convection Over a Vertical Backward-facing Step for Lead-bismuth Eutectic. *International Journal of Heat and Mass Transfer*, **127**, 1215–1229. doi: https://doi.org/10.1016/j.ijheatmasstransfer.2018.08.116.

ZHAO, P., GE, Z., ZHU, J., LIU, J., & YE, M. 2018b. Quasi-direct Numerical Simulation of Forced Convection over a Backward-facing Step: Effect of Prandtl Number. *Nuclear Engineering and Design*, **335**, 374–388. doi: https://doi.org/10.1016/j.nucengdes.2018.05.012.

ZIEREP, J. 1991. *Ähnlichkeitsgesetze und Modellregeln der Strömungslehre*. 1st edn. Berlin Heidelberg: Springer Verlag. ISBN: 978-3-662-21597-5.

# Appendix A

# Assessment of the non-OBERBECK-BOUSSINESQ approximation

When studying convective flows, one must answer the question whether the Oberbeck-Boussinesq or the non-Oberbeck-Boussinesq approxmation are valid for the case of study. It may be recalled that the difference between both set of equations rely on the assumption of constant physical properties for the fluid within a given temperature range. This can be done in a systematic and quantitative way with the method proposed by Gray & Giorgini (1976), who applied their method to water and air. Niemann (2017) shows the same analysis for liquid sodium. Here, a similar analysis is presented for the *GaInSn* case.

The difference compared to the original version by Gray & Giorgini (1976) relies on that here the assessment whether the thermo-physical fluid propierties are considered as constant or temperature dependent is done prior to substituting the linearized version of the physical properties into the equations. This accounts for possible errors in assuming a linear dependency of fluid physical properties before making any statement on the simplification of the equations. This is important because, as shown in Gray & Giorgini (1976), the calculated maximum temperature range is one order of magnitude smaller than the one for this experiment. As a consequence, for water it may be valid to assume a linear dependency around a reference point, while for this experiment with *GaInSn*, it may not. A further difference of this analysis compared to the original one is that here the dimensionless version of the governing equations is derived in a the first step, which may be more

intuitive for the non-expert reader.

The proposed method is the following:

i. Non-dimensional variables are defined and substituted into the governing equations. Non-dimensional groups can now be identified and defined.

ii. The dependence of the physical properties are expressed as a function of two intensive (in the thermodynamic sense) properties. Here, temperature and pressure are used.

iii. Temperature and pressure dependent empirical physical property correlations are looked up in the literature.

iv. The fluid property correlations are evaluated within the temperature and pressure range of the experiment. A threshold of 10% is arbitrarily defined to be an acceptable variability for the fluid properties within the chosen range. If the fluid properties vary below the 10% threshold for the given temperature and pressure range, the respective fluid property may be regarded as a constant for the analysis. If not, the fluid property must be considered as temperature and/or pressure dependent for the analysis.

v. The empirical correlations for temperature and pressure dependent physical properties are linearized with a Taylor expansion around a reference point. Assuming a linear temperature and/or pressure dependency, a maximum temperature range for which properties can be considered as constants can be calculated by means of the sensitivity.

vi. All dimensionless numbers and physical property sensitivities are calculated. The governing equations are then simplified.

## A.1 Fluid property dependent equations for the experiment

For the sake of simplicity, all fluid physical properties and related non-dimensional groups are expressed as a column vector $\vec{b} = b_i = [\rho, \mu, \nu, \lambda, c_p, a, Pr]^T$, where $Pr$ is the Prandtl number defined as $Pr = \nu/a$. The intensive properties used for this case are temperature and pressure. However, since liquid metal experiments (and applications) are usually designed for pressures around atmospheric pressure, little

to no information could be found in the literature regarding the pressure dependence of $b_i$. Hence, the pressure dependence for this experiment are neglected, i.e. $b_i = b_i(T)$ only.

The chosen empirical correlations from the literature for the physical properties are:

$$\rho(T) = 0.7584 \cdot T + 6637.9 \ [\mathrm{kg/m^3}], \tag{A.1}$$

$$\mu(T) = 0.4352 \cdot e^{\frac{3904}{8.3144 \cdot T}}) \ [mPa \cdot s], \tag{A.2}$$

$$\lambda(T) = 0.0486 \cdot T + 10.574 \ [W/m \cdot K], \tag{A.3}$$

$$c_p(T) = 0.007 \cdot T^2 - 0.7771 \cdot T + 569.39 \ [J/kg \cdot K], \tag{A.4}$$

where Eqs. (A.1) and (A.3) are taken from Emmendörfer (2015) and Eq. (A.2) has been taken from Plevachuk *et al.* (2014). Eq. (A.4) has been derived using the experimental data given by Emmendörfer (2015), however fitting a quadratic polynomial instead as a linear function, as done originally. The given relative errors for the empirical correlations in Eqs. (A.1)-(A.4) are 0.37% , 0.05% , 5% , 3%, respectively.

Further fluid properties can be defined as follows,

$$\nu(T) \equiv \frac{\mu(T)}{\rho(T)} \ [\mathrm{m^2/s}], \tag{A.5}$$

$$a(T) \equiv \frac{\frac{k(T)}{c_p(T)}}{\rho(T)} = \frac{\lambda(T)}{\rho(T) \cdot c_p(T)} \ [\mathrm{m^2/s}], \tag{A.6}$$

where $\nu$ is the kinematic viscosity or momentum diffusivity, $\alpha_m$ is the molecular thermal diffusivity or *temperature conductivity*[1].

Besides, the ratio between between the momentum- and the thermal diffusivity can be defined as as a function of temperature as

$$Pr(T) \equiv \frac{\nu(T)}{a(T)} \ [-], \tag{A.7}$$

where $Pr$ stands for the Prandtl number.

[1] This definition is mainly found in the German literature.

The fluid properties are plotted and shown in Fig. A.1, where a 10% threshold around the reference value is marked as the zone in light red. The dashed vertical line indicates the maximum expected characteristic $\Delta T_{c,max}$ in the experiment (at full heated plate power $\dot{q}_{max}$), which is calculated using Eq. (2.12) as $\Delta T_{c,max}\left(\dot{q}_{max}, l_c, k_{ref}\right) = 33.57\ [^\circ C]$, with $l_c = 0.04\,[m]$ (defined by the experiment), $\dot{q}_{max} = 20833\,[\mathrm{W/m^2}]$ and $k_{ref}$ calculated from Eq. (A.3) at the reference temperature $T_{ref} = 20\,[^\circ C]$.

It can be observed that the dynamic viscosity $\mu$ together with the kinematic viscosity $\nu$ are the only physical properties that escape the 10% threshold, i.e. these properties need to be considered as temperature, and hence, spatially dependent. In other words, cannot be taken out of the spatial derivatives in Eq. (2.7). The PRANDTL number shows a strong temperature dependency as well, which is important to consider when assessing results from CFD simulations.

The next step is to linearize (Taylor expansion) Eqs. (A.1)-(A.7) around the reference temperature $T_{ref}$, which for this experiment is chosen to be $T_{ref} = 20\ [^\circ C]$. Truncating the Taylor expansion after the first order term, one gets as a general form:

$$b_i(T) = b_{i,ref} + \left.\frac{\partial b_i}{\partial T}\right|_{ref}\left(T - T_{ref}\right) = b_{i,ref}\left(1 + \varepsilon_2\right), \tag{A.8}$$

where $b_i(T) = \left[\rho(T), \mu(T), \nu(T), \lambda(T), c_p(T), a(T), Pr(T)\right]^T$ and where $\varepsilon_i(\Delta T) = \left[\frac{1}{b_{ref}} \left.\frac{\partial b_i}{\partial T}\right|_{ref} \Delta T\right]^T$ with the same indices as for $b_i$. When calculating $\nu(T)$, $a(T)$ and $Pr(T)$ from temperature dependent functions, the derivative rules must be used (chain rule, etc.).

The resulting linear functions and the relative linearization error $e_{lin}$ is plotted against temperature in Fig. A.2 and Fig. A.3, respectively. The 10% threshold is kept for the linearized equations. The error in assuming a linear approximation around $T_{ref}$ is within a 5% threshold (marked region in light red), as shown in Fig. A.3. As a result, a linearized expression for the physical properties be suitable for calculating the maximum temperature range $\Delta T_{a_i,max}$ for which each fluid property may be taken as a constant, considering the 10% threshold as a criterion, see Gray & Giorgini (1976).

These results are shown in Table A.1. It can be concluded that expressing Eqs. (2.15)-(2.17) in terms of a variable, yet linear function of $\mu$ against temperature may induce an relative error of less than 5%. The equations now read as

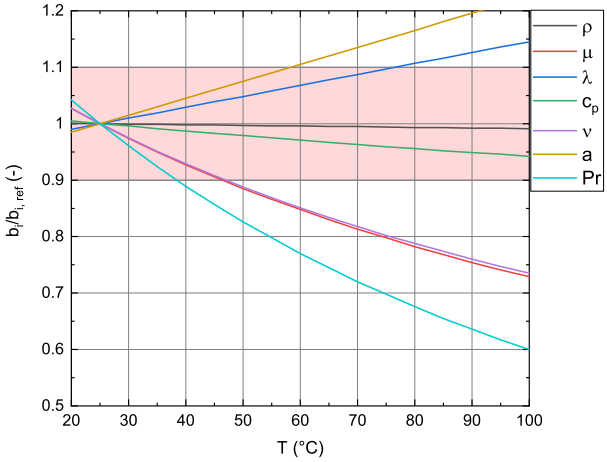


Figure A.1: Relative change of the thermo-physical properties of *GaInSn* (Eqs. (A.1) to (A.7)) as a function of temperature.

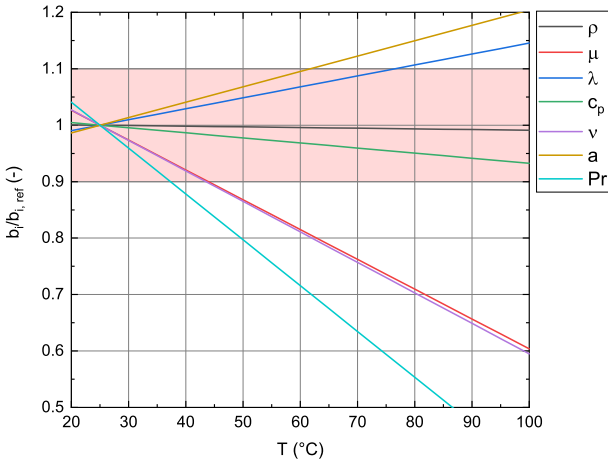


Figure A.2: Relative change of the *linearized* thermo-physical properties of *GaInSn* as a function of temperature.

$$\frac{\partial u_i^*}{dx_i^*} \approx 0, \tag{A.9}$$

$$\rho^* \frac{Du_i^*}{Dt^*} \approx Ri\,\theta\hat{x} - \frac{\partial p^*}{\partial x_i^*} + \frac{1}{Re}\frac{\partial}{\partial x_j^*}\mu^*\left(\frac{\partial u_i^*}{\partial x_j^*} + \frac{\partial u_j^*}{\partial x_i^*}\right), \tag{A.10}$$

$$\rho^* c_p^* \frac{D\theta}{Dt^*} = \frac{1}{Re\,Pr} k^* \frac{\partial^2 \theta}{\partial x_i^* \partial x_i} + Ec\,K_\rho\,\beta^*\theta\frac{Dp^*}{Dt^*} + \frac{Ec}{Re}\mu^*\Phi^*, \tag{A.11}$$

where $\mu^*$ may be taken as a non-linear expression (Eq. (A.2)), or as its linearized version as $\mu^* = \mu^*_{lin}(\Delta T) \equiv \frac{\mu_{ref}(1+\varepsilon_2(\Delta T))}{\mu_{ref}}$.

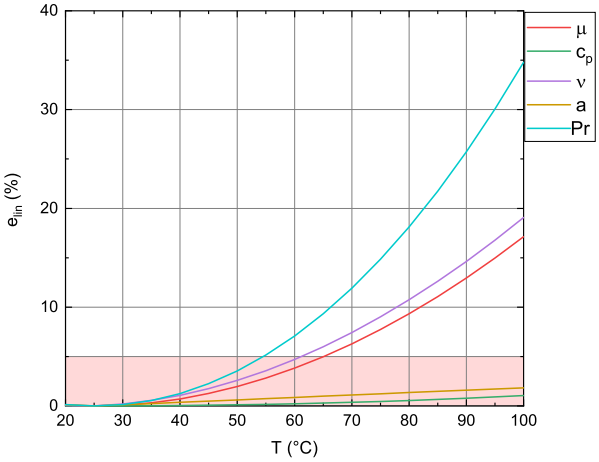


Figure A.3: Relative error of the linearization procedure of the thermo-physical properties plotted over temperature.

Table A.1: Maximum temperature range for constant physical property assumption (four significant figures)

| $a_i$ | $\rho$ | $\mu$ | $\lambda$ | $c_p$ | $\nu$ | $a$ | $Pr$ |
|---|---|---|---|---|---|---|---|
| $\Delta T_{b_i,max} = \frac{10\%}{\varepsilon_i}\ [°C]$ | 846.9 | 18.30 | 51.07 | 109.6 | 17.91 | 36.33 | 12.00 |

## A.2 Neglecting the pressure work and dissipation rate terms

Eq. (A.11) can be further simplified by assessing the influence of the pressure work and the dissipation terms. For this, characteristic scales for length, velocity and temperature difference must be defined, which may be of global or local character. Here, the characteristic scales are defined globally, i.e. $l_c$ is defined as the step height, $U_c$ as the bulk inlet velocity and $\Delta T_c$ as in Eq. (2.12), as shown in Table A.2. Furthermore, in Table A.2 the characteristic scales are given for the minimum and maximum operational range of the DITEFA 2 facility[2]. The calculated dimensionless numbers are shown in Table A.2, where the *worst case scenario* is taken, i.e. highest $U_c$, lowest $\Delta T_c$. One can observe that both $Ec\,K_p$ and $\frac{Ec}{Re}$ terms are very small, i.e. they can safely be neglected in Eq. (A.11) with respect to the other terms. This also holds when defining the characteristic scales locally. In fact, both neglected terms only play a role in flows with characteristics way out of the scope

[2]For the calculation of $\Delta T_c$, $\dot{q}$ has been taken between $1042 - 20833\ [\mathrm{W/m^2}]$

Table A.2: Global characteristic scales and physical properties at reference temperature (four significant figures). For$U_c$ and $\Delta T_c$ the range with the experimental maximum and minimum values is given.

| | $l_c$ | $U_c$ | $\Delta T_c$ | $\rho_{ref}$ | $\mu_{ref}$ | $c_{p,ref}$ | $\nu_{ref}$ |
|---|---|---|---|---|---|---|---|
| Unit | $[mm]$ | $[\mathrm{m/s}]$ | $[^\circ C]$ | $[\mathrm{kg/m^3}]$ | $[Pa \cdot s]$ | $[\mathrm{J/kg{\cdot}K}]$ | $[\mathrm{m^2/s}]$ |
| Value | 40.00 | $0.03125 - 0.4688$ | $1.679 - 33.57$ | 6416 | $2.115 \cdot 10^{-3}$ | 401.2 | 3.366 |

Table A.3: Calculated REYNOLDS, ECKERT and thermal expansion numbers with values given in Table A.2 (four significant figures)

| | $Ec_{ref} \cdot K_{p,ref}$ | $\frac{Ec}{Re}$ |
|---|---|---|
| Unit | $[-]$ | $[-]$ |
| Value | $6.475 \cdot 10^{-8}$ | $5.857 \cdot 10^{-9}$ |

of this thesis work (supersonic flows, for example).

# *APPENDIX A. ASSESSMENT OF THE NON-*OBERBECK-BOUSSINESQ *APPROXIMATION*

# Appendix B

# Numerical solution of turbulent flows

For the interested reader, the general *problem of turbulence* and its solution strategies is reviewed and intuitively explained in a thorough yet concise manner in Farge *et al.* (1996). For a detailed introduction, discussion and deeper analysis on the solution strategies of the problem of turbulence, the reader is forwarded to - in alphabetical order - Bradshaw (1971), Davidson (2015), George (2013), Landau & Lifshitz (1987), Monin & Yaglom (1971), Monin & Yaglom (1975), Pope (2000), Tennekes & Lumley (1972) and Tropea *et al.* (2007). For fluid mechanics background, the reader is referred to Batchelor (1967), Kundu *et al.* (2016). For continuum mechanics background, the reader is referred to Lai *et al.* (2009).

## B.1 The Reynolds averaged equations and the turbulence closure problem

One strategy to extract information out of the equations for fluid motion is to introduce the so-called REYNOLDS *decomposition*, into the continuity, Navier-Stokes and energy equations. The Reynolds decomposition reads to

$$\phi = \langle \phi \rangle + \phi', \tag{B.1}$$

where $\phi$ is a instantaneous random flow variable ($\phi = (u_i, p, T, \Delta T, \rho, ...)$, $\langle \phi \rangle$ the ensemble average[1] of $\phi$ and $\phi'$ the fluctuation of $\phi$ around the ensemble average, i.e. $\phi' \equiv \phi - \phi'$.

Substituting the Reynolds decomposition for every variable into the continu-

[1] Not to be confused with time and/or space averages!

ity, momentum (taking the Boussinesq approximation into account) and energy equations, time-averaging the full set of equations, rearranging and simplifying one gets the so-called Reynolds Averaged Navier-Stokes () equations for turbulent flows which read[2]

$$\frac{\partial \langle u_i \rangle}{dx_i} \approx 0, \tag{B.2}$$

$$\rho_{ref} \frac{D \langle u_i \rangle}{Dt} \approx \left(\rho_{ref} \beta_{ref} \langle \Delta T \rangle\right) g\hat{x} - \frac{\partial \langle p_{mod} \rangle}{\partial x_i} + \frac{\partial}{\partial x_j} \left( \langle \tau_{ji} \rangle - \rho_{ref} \langle u_i' u_j' \rangle \right), \tag{B.3}$$

$$\frac{D \langle \Delta T \rangle}{Dt} = \frac{\partial}{\partial x_i} \left( \frac{k}{\rho_{ref} c_p} \frac{\partial \Delta T}{\partial x_i} - \langle u_i' \Delta T' \rangle \right), \tag{B.4}$$

where the time averaged energy equation can also be written in terms of temperature $T$ as such:

$$\frac{D \langle T \rangle}{Dt} = \frac{\partial}{\partial x_i} \left( \frac{k}{\rho_{ref} c_p} \frac{\partial T}{\partial x_i} - \langle u_i' T' \rangle \right). \tag{B.5}$$

Equations (B.3) and (B.5) are transport equations for the ensemble averaged quantities. They are very similar compared to their instantaneous counterpart but for the terms $\left\langle u_i' u_j' \right\rangle$ and $\langle u_i' T' \rangle$ which are called *Reynolds stress*[3] and *turbulent heat flux*, respectively. These terms contain all the information relative to turbulence and turbulent convective heat transfer.

A closer look into Eqs. (B.2)-(B.5) shows that this set of equations is not closed. The Reynolds stress and turbulent heat flux terms are extra terms that include nine[4] further variables to be calculated. In the literature this is referred as the *turbulence closure problem.* The strategies on how to close this system of equations is presented in the next section.

[2]Originally, these equations have been deduced by Reynolds by means of time averages. In later years, these equations have been demonstrated to be more general by allowing their definition in terms of ensemble averages (Monin & Yaglom (1971), p. intro)

[3]This term is actually *not* a physical stress. It only has the units of stress. Since the term enhances momentum transfer, it *may* be considered mathematically as a stress.

[4]Six for the Reynolds stresses, three for the turbulent heat flux

# B.2 Turbulence and convective heat transfer RANS calculation approaches

## B.2.1 Approaches for turbulent flow calculations

In nearly every thermal-hydraulic technical application, turbulent flows are encountered. In order to calculate and predict convective turbulent flows, the continuity, the Navier-Stokes and the energy equation must be solved numerically. For this, three main approaches exist. A rigorous introduction into general turbulence calculation, see Pope (2000).

First, one could take the *exact* set of equations (e.g. Eqs. (2.19)-(2.21)) and solve them numerically in both time *and* space for a long period of time and all flow structures. This approach is called direct numerical simulation (DNS). Unfortunately, this is currently impossible for engineering relevant flows due to limited computational power. The second approach takes the same set of equations as for DNS, but filters them *spatially* and then solves them accordingly in time. The biggest flow structures are hence solved numerically exactly in space, while the filtered smaller structures are modeled. The approach is called large eddy simulation (LES) and is used in the climate research and for rather simple engineering flows of interest. Thanks to increasing computational power this approach is gaining popularity in more complex engineering applications as well. Finally, the third approach, which is by far the most used in practical engineering applications, solves equations (B.2)-(B.4) or (B.5). But, as mentioned before, here one has to deal with the turbulence closure problem for which different approaches exist. In the following lines the transport equations for both $\left\langle u_i' u_j' \right\rangle$ and $\langle u_i' T' \rangle$ are presented. From these, more simple approaches for closing the equations are only introduced and mentioned in a conceptual basis.

## B.2.2 Reynolds stress and turbulent heat flux equations

**Transport equations for $\left\langle u_i' u_j' \right\rangle$** The transport equations for the Reynolds stress including along the body forces only the buoyancy term, read to

$$\underbrace{\frac{D\left\langle u_i'u_j'\right\rangle}{Dt}}_{C_{ij}} = \underbrace{\left(\left\langle u_i'u_j'\right\rangle\frac{\partial\left\langle u_j'\right\rangle}{\partial x_k}+\left\langle u_j'u_k'\right\rangle\frac{\partial\left\langle u_i'\right\rangle}{\partial x_k}\right)}_{P_{ij}}+\underbrace{\left(g_i\beta\left\langle u_j'T'\right\rangle+g_j\beta\left\langle u_i'T'\right\rangle\right)}_{G_{ij}}-\underbrace{\left\langle\frac{p'}{\rho}\left(\frac{\partial u_i'}{\partial x_j}+\frac{\partial u_j'}{\partial x_i}\right)\right\rangle}_{\Phi_{ij}}$$

$$+\underbrace{\frac{\partial}{\partial x_k}\left\langle\frac{p'}{\rho}\left(u_i\delta_{jk}+u_j\delta_{ik}\right)\right\rangle}_{D_{ij}^p}+\underbrace{\frac{\partial}{\partial x_k}\left\langle\nu\frac{\partial\left\langle u_i'u_j'\right\rangle}{\partial x_k}\right\rangle}_{D_{ij}^\nu}+\underbrace{\frac{\partial}{\partial x_k}\left\langle u_i'u_j'u_k'\right\rangle}_{D_{ij}^t}-\underbrace{2\nu\left\langle\frac{\partial u_i'}{\partial x_k}\frac{\partial u_j'}{\partial x_k}\right\rangle}_{\varepsilon_{ij}}, \tag{B.6}$$

where $C_{ij}$ is the *convective term*, $P_{ij}$ is the turbulence production term due to straining, $G_{ij}$ an extra turbulence production term due to buoyancy-induced forces due to the turbulent heat flux, $\Phi_{ij}$ the pressure-strain term, $D_{ij}^p$ the pressure diffusion term, $D_{ij}^\nu$ the viscous diffusion term, $D_{ij}^t$ the turbulent transport term and $\varepsilon_{ij}$ the dissipation rate term. A deeper analysis of each term, their physical interpretation and, where necessary, their respective modeling can be found in George (2013), Hanjalic & Launder (2011), Leschziner (2015) and Pope (2000).

This approach takes automatically into consideration the intrinsic directional scale dependency of turbulent flows, contrary to more simple models called *eddy viscosity* models. Eddy viscosity models condense very important characteristics of turbulence into one constant (the *eddy viscosity* $\nu_t$) and fitting modeling constants to ad hoc data, making them case sensitive.

The main advantage of this modeling ansatz is that both production terms can be calculated *exactly*, i.e. there is no need of modeling for these terms. This is very important for the calculation for a BFS (Leschziner (2015), p. 230). Furthermore, this advantage is of particular relevance in buoyancy influenced flows. The pressure-strain, the pressure-diffusion, the turbulent transport and the dissipation-rate terms must be modeled.

An alternative approach is to make assumptions and simplifications to Eq. (B.6) regarding the convective $C_{ij}$ and divergence terms ($D_{ij}^{(...)}$). As a result the so-called *algebraic Reynolds stress models* can be derived. These can be expressed in either an explicit or an implicit formulation. Implicit models show in fact no major advantages with respect to the made simplifications for deriving these models. However, in order to take advantage of the more complete - yet simplified - implicit for-

mulation for the Reynolds stresses, explicit models can be developed. Algebraic workarounds are applied to them and explicit formulations can be stated. These explicit models can be simplified one step further to obtain so-called *baseline* explicit algebraic models which are found in common commercial CFD codes. Another route to take into consideration the directional scale dependency of turbulent flows is to take some aspects the starting point for the derivation of explicit algebraic models to derive Eq. (B.6) so-called *non-linear eddy viscosity models.* However, as mentioned by Leschziner (2015), the limiting line between explicit algebraic models and non-linear eddy viscosity models is *fuzzy*, which sometimes leads to confusion.

Another route in order to close eqs. (B.3) is to introduce the concept of an *eddy viscosity* $\nu_t$ for calculating the Reynolds stresses in an analogous way as the calculation of viscous stress tensor. That is, to assume a linear dependency of the Reynolds stress tensor to the local fluid strain (expressed in terms of the velocity gradient tensor) multiplied by a constant factor $\nu_t$ (in analogy to the molecular kinematic viscosity $\nu$). This analogy is called the BOUSSINESQ analogy[5]. When this multiplying factor $\nu_t$ is a constant for all flow directions, the factor is called an *isotropic*[6]. The eddy viscosity $\nu_t$ may be calculated in different ways: 0-equation models[7], 1-equation models, 2-equation models (typically used). The above mentioned *non-linear eddy viscosity models* may be thought as the anisotropic version of these kind of models, i.e. different values for $\nu_t$ are calculated for all flow directions.

For more details on the topic of Reynolds stress closure, see Leschziner (2015), Pope (2000) and Hanjalic & Launder (2011).

### B.2.3 Transport equation for $\langle u_i' T' \rangle$

As can be seen in both eqs. (B.5) and (B.6), the turbulent heat flux term plays a very important role in the proper determination of the velocity field. The transport equation for the turbulent heat flux taking into consideration buoyancy body forces read to

[5]Not to be confused to the Boussinesq approximation for buoyant flows

[6]These kind of models are sometimes called *isotropic models*. This may lead the inexperienced reader to think that these models cannot reproduce flow anisotropy, which is wrong since it can be perfectly reproduced due to the functional dependency to the velocity gradient tensor. It is *only* the eddy viscosity which is assumed to be isotropic in these models.

[7]Unfortunately also sometimes called *algebraic* - leading to even more confusion.

$$\underbrace{\frac{D\left\langle u_i' T' \right\rangle}{Dt}}_{C_{iT'}} = \underbrace{\left( \left\langle u_j' T' \right\rangle \frac{\partial \left\langle u_i' \right\rangle}{\partial x_j} + \left\langle u_i' u_j' \right\rangle \frac{\partial \left\langle T \right\rangle}{\partial x_j} \right)}_{P_{iT'}} \underbrace{- \beta g_i \left\langle T'^2 \right\rangle}_{G_{iT'}} + \underbrace{\left\langle \frac{p'}{\rho} \frac{\partial T'}{\partial x_i} \right\rangle}_{\Pi_{iT'}}$$

$$\underbrace{- \frac{\partial}{\partial x_j} \left( \left\langle u_i' u_j' T' \right\rangle + \frac{\left\langle p' T' \right\rangle}{\rho} \delta_{ij} + \alpha \left\langle u_i \frac{\partial T'}{\partial x_j} \right\rangle + \nu \left\langle T' \frac{\partial u_i'}{\partial x_j} \right\rangle \right)}_{D_{iT'}} \underbrace{- (\nu + \alpha) \left\langle \frac{\partial T'}{\partial x_j} \frac{\partial u_i'}{\partial x_j} \right\rangle}_{\varepsilon_{iT'}}, \tag{B.7}$$

where $C_{iT'}$is the convection term, $P_{iT'}$is the production term due to strain and temperature gradients, $G_{iT'}$ the production term due to buoyancy forces[8], $\Pi_{iT'}$ the pressure-temperature interaction or pressure scrambling, $D_{iT'}$ divergence or diffusion terms and $\varepsilon_{iT'}$ the dissipation term.

Although the structure and the naming of each term in Eq. (B.7) may be similar than those in eqs. (B.6), a physical interpretation by direct analogy can't be stated for every term (Leschziner (2015), p. 81 f). For a detailed discussion on the physical interpretation of each term and the modeling possibilities, the reader is forwarded to Hanjalic & Launder (2011)and Leschziner (2015). Analogous as for the Reynolds stress transport modeling ansatz, implicit algebraic models can also be derived for $\left\langle u_i' T' \right\rangle$ by making some simplifications to Eq. (B.7). Further simplifications to implicit algebraic turbulent heat flux models can still be made in order to obtain so-called *general gradient diffusion hypothesis* models. The latter may be also understood as *anisotropic* gradient diffusion hypothesis models, since

Analogous to isotropic eddy viscosity models for the Reynolds stress tensor, so-called *simple gradient diffusion hypothesis* models can be stated as well for the turbulent heat flux. Several model types exist. On one hand, some consider a rather direct relationship between the eddy viscosity $\nu_t$ and an *eddy diffusivity* $a_t$ by means of the so-called *turbulent Prandtl number* defined as $Pr_t \equiv \nu_t / a_t$. The turbulent Prandtl number $Pr_t$ may be fixed as a constant or expressed as a correlation dependent on geometrical and flow variables, see Grötzbach (2013). On the other hand, other models within this group are so-called $2+2$ or 4-equation models, which calculate $a_t$ not by means of simple correlations for $Pr_t$, but by means of transport equations of physically motivated variables[9]. The way $a_t$ is calculated

[8] A transport equation for the temperature fluctuation variance $\left\langle T'^2 \right\rangle$ is needed.

[9] Caution: some authors in the literature call isotropic eddy diffusivity models "explicit algebraic turbulent heat flux models", leading - again - to confusion

may vary from model to model, but the bottom line is the same: a single eddy diffusivity $a_t$ is calculated as a multiplying factor for all components of the temperature gradient $\nabla T$, hence isotropic. The turbulent heat flux is then calculated as a linear relationship between $\nabla T$ and the constant pre-multiplying factor $a_t$ (hence the name "single gradient diffusivity model").

As pointed out by Grötzbach (2013) (and references therein), the proper calculation of the turbulent heat flux is of particular importance in liquid metal convective flows, since these are - in general - heavily anisotropic flows (in the sense of scale directional dependency of the Reynolds stresses and the turbulent heat flux vector). By inspection, one can observe that each component of the turbulent heat flux vector is dependent on the other components, as well of every single Reynolds stress. This means that, in order to properly calculate $\langle u_i' T' \rangle$, a detailed and correct description of the Reynolds stress field is required. This can only be achieved with a full transport equation modeling ansatz for $\left\langle u_i' u_j' \right\rangle$ as Eqs. (B.6).

For more details on turbulent heat flux modeling, see Leschziner (2015), Hanjalic & Launder (2011) and Trimborn (2018).

## B.3 Peculiarities for the liquid metal case

The Prandtl number can be interpreted as proportional to the thickness-ratio between the viscous and the thermal boundary layers.When modeling convective turbulent flows for the case of fluid with $Pr \sim 1$, some assumptions can be made to Eqs. (B.6) and (B.7). Based on the *scale similarity* between the viscous (or velocity) and thermal (or temperature) boundary layers, one can roughly say that the thermal boundary layer can be calculated *from* the velocity boundary layer. The reason why this may work for fluids with $Pr \sim 1$ is depicted in Fig. 1.1. Observing the velocity contours and comparing these with the temperature contours for $Pr \sim 1$, a similar turbulence structure can be identified. This means that it will not be such of an error to assume that that the temperature field *could* be obtained from the velocity field by means of a constant turbulent Prandtl number $Pr_t$. This assumption is called the Reynolds analogy and is the cornerstone of modern convective heat transfer CFD in commercial and open-source codes alike. With the eddy diffusivity gradient hypothesis models can be derived. However, for the liquid metal case, i.e. $Pr \ll 1$, the velocity field can be hardly related to the temperature field, since by dimensional analysis (Bejan (2013); Jischa (1982))

$$\frac{\delta}{\delta_T} \sim Pr^{1/2} < 1\,, Pr \ll 1, \tag{B.8}$$

where $\delta$ is the viscous (or velocity) boundary layer thickness and $\delta_T$ is the thermal (or temperature) boundary layer thickness.

In other words, the smaller the Prandtl number, the worst the Reynolds analogy for calculating $\langle u_i' T' \rangle$, because the thermal boundary layer gets thicker relative to the velocity boundary layer (see Fig. B.1). One alternative is to take a variable $Pr_t$ dependent on geometrical and flow parameters. However, still too much physics is condensed into only one constant, besides of the fact that this approach is highly empiric, which means that it must be still fitted to ad hoc experimental data with the consequence of a high degree of case sensitivity. The optimum is to calculate $\langle u_i' T' \rangle$ from transport equations, as shown in the previous section. The drawback of the $\langle u_i' T' \rangle$-transport equation approach, and the main reason why it's not implemented everywhere, is that in Eq. (B.7) some terms must be modeled as well. Modeling requires the definition of modeling constants, for which experiments (real or numerical) are needed.

In fact, a full transport equation approach for $\langle u_i' T' \rangle$ may not be even necessary for all cases. However, this statement is very case sensitive to the fluid $Pr$ number and the flow $Ri$ number. For forced convection cases, Davidson (2015) (p. 162) mentions it is possible to relate the dimensionless thickness in wall normal coordinate $y^+$ of the viscous sub-layer for $\delta$ with its respective counterpart for $\delta_T$ as $y^+ \sim 5/Pr$, i.e. the extension of the region of $\delta_T$ where the influence of $\langle u_i' T' \rangle$ could be neglected. Kader (1981) proposes a similar relationship, but uses a factor of 2 instead of 5. However, taking into consideration a laminar boundary layer scale analysis (Bejan (2013), p. 179), this author proposes a relationship of the kind

$$y^+ \sim 5/\sqrt{Pr}, \tag{B.9}$$

which seems more plausible for the thickness of the conductive sub-layer for the specific case of a heated wall bounded channel flow in forced convection regime. Qualitatively, Eq. (B.9) fits the data of Duponcheel *et al.* (2014) for forced convection wall bounded channel flow for low $Pr$ cases in a better way. Eq. (B.9) may be used as a first order of magnitude estimate for the thickness of the conductive sub-layer for liquid metal wall bounded flows in forced convection.

For a physical introduction into liquid metal convective flows and the issues regarding modeling, see Grötzbach (2013). For an introductory review on mod-

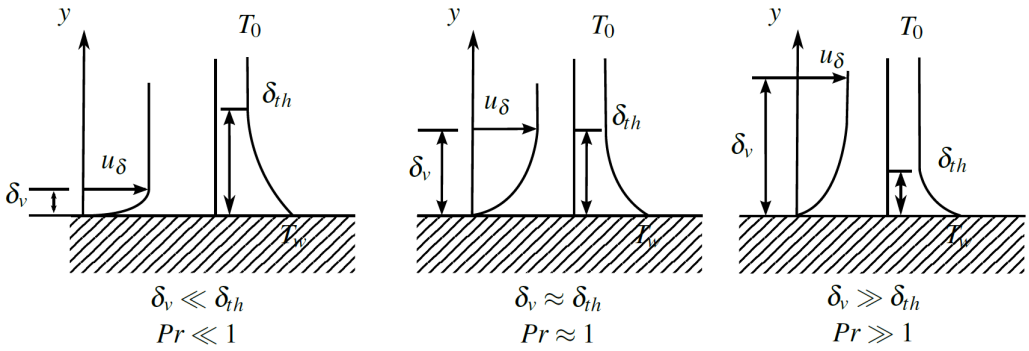


Figure B.1: Qualitative order of magnitude representation of boundary layer thickness for velocity and temperature. Figure taken from OECD/NEA (2015).

eling approaches for the liquid metal case can be found in Shams *et al.* (2019) and Roelofs & Shams (2019). For a very detailed and thorough review on the approaches for modeling the turbulent heat flux for both low ($Pr \ll 1$) and moderate ($Pr \sim 1$) Prandtl numbers, see Trimborn (2018).

# Appendix C

# Statistical analysis of measured signals

## C.1 Case for a continuous random variable

If turbulent, fluid motion becomes chaotic and random (in the sense of Pope (2000), p. 34 and George (2013), p. 309). Hence, it may be intuitive to analyze turbulent flows - either in experiments or in simulations - by means of statistical methods. Let $\phi$ be a continuous random variable as defined before for the Reynolds decomposition. The *true time average* for a stationary random ergodic process is defined as (George (2013)),

$$\langle \phi \rangle \overset{ergodic}{=} \mu_\phi \equiv \lim_{T\to\infty} \frac{1}{T} \int_0^T \phi\,(t)\,dt, \tag{C.1}$$

where $T$ is the total integration time, the principle of ergodicity is used for the equality between the ensemble average $\langle \phi \rangle$ and the true time average $\mu_\phi$ for the random variable $\phi$.

In practice it is not feasible to perform an infinitely long experiment. The true time average $\mu_\phi$ is hence *estimated* as

$$\hat{\mu}_\phi \equiv \frac{1}{T} \int_0^T \phi\,(t)\,dt, \tag{C.2}$$

where from now on the concept of *estimator* of a random variable is denoted by *hat* $\hat{(...)}$.

It is important to note that $\hat{\mu}_\phi$ is a random variable as well, since its value depends on $T$ and on *which* time slot the estimator for the time average is taken. If

$\left\langle \hat{\mu}_\phi \right\rangle \to \mu_\phi$ when $T \to \infty$, then $\hat{\mu}_\phi$ is said to be an *unbiased estimator* of $\mu_\phi$ (George (2013)). The more measurements taken, the better the estimation of $\mu_\phi$ by $\hat{\mu}_\phi$. But the value of $\hat{\mu}_\phi$ *fluctuates* around $\mu_\phi$ as $N$ becomes larger. In order to quantify the error made when not taking an infinite number of measurements, one studies the *convergence* of the estimator $\hat{\mu}_\phi$. For this, the *variability* $\varepsilon^2$ *of the estimator* $\hat{\mu}_\phi$ is defined as

$$\varepsilon^2_{\hat{\mu}_\phi} \equiv \frac{\sigma^2_{\hat{\mu}_\phi}}{\mu^2_\phi}, \tag{C.3}$$

where $\sigma^2_{\hat{\mu}_\phi} \equiv \left\langle \left(\hat{\mu}_\phi - \mu_\phi\right)^2 \right\rangle$ is the *true* variance of the *estimator* $\hat{\mu}_\phi$.

It can be shown that the variability $\varepsilon^2_{\hat{\mu}_\phi}$ of the estimator $\hat{\mu}_\phi$ can be calculated as

$$\varepsilon_{\hat{\mu}_\phi} = \sqrt{\frac{2t_{int}}{t_s}} \frac{\sigma_\phi}{\mu_\phi}, \tag{C.4}$$

where $\sigma^2_\phi \equiv \left\langle \phi'^2 \right\rangle$ is the variance of the random variable $\phi$ and $t_{int}$ is the *integral time scale* for this random process defined as

$$t_{int} \equiv \lim_{T\to\infty} \int_0^T \rho\left(\tilde{\tau}\right) d\tilde{\tau}, \tag{C.5}$$

where $\tilde{\tau}$ is the temporal integration variable and $\rho\left(\tau\right)$[1] is defined as the *autocorrelation coefficient* as

$$\rho\left(\tau\right) \equiv \frac{\left\langle \phi'\left(t\right) \phi'\left(t+\tau\right) \right\rangle}{\left\langle \phi'^2 \right\rangle} = \frac{C\left(\tau\right)}{C\left(0\right)}, \tag{C.6}$$

where $\phi'$ is the fluctuation of $\phi$ around its true mean $\mu_\phi$, $\tau$ is a time lag and the numerator of Eq. (C.6) is defined as the *autocorrelation function* or *two times-one point correlation function* $C\left(\tau\right)$, which quantifies the *memory* of the random process in time.

$T_{int}$ may be also *estimated* from appropriate velocity and length scales as $T_{int} = {}^{U_c}/_{l_c}$. In Eq. (C.4) the *true* variance $\sigma^2_\phi$ of the random variable $\phi$ can be *estimated* with

$$\hat{\sigma}^2_\phi = \frac{1}{T} \int_0^T \left(\phi\left(t\right) - \mu_\phi\right)^2 dt, \tag{C.7}$$

and $\mu_\phi$ can be estimated with Eq. (C.2).

[1] Note that $\rho \neq \rho$!

## C.2 Discrete random variable

In experiments, measurements are taken as discrete measurement points, thus Eq. (C.2) needs to be rewritten as

$$\hat{\mu}_\phi \approx \frac{1}{N\Delta t}\sum_{i=1}^{N}\phi_i\Delta t = \frac{1}{N}\sum_{i=1}^{N}\phi_i, \tag{C.8}$$

where the total integration time $T$ is divided into $N$ smaller time steps $\Delta t$, which have to be taken *long enough* (to be defined later) to guarantee statistical independence between each *realization* of $\phi_i$.

Analogous as for the continuous case, for a discrete random variable, the variability of an estimator around the true mean of a $\phi_i$ can be obtained (George (2013)). It reads,

$$\varepsilon_{\hat{\mu}_{\phi_i}} = \frac{1}{\sqrt{N}}\frac{\sigma_\phi}{\mu_\phi} = \frac{1}{\sqrt{N}}Tu, \tag{C.9}$$

where $N$ is the total number of *statistically independent* samples of $\phi_i$ and $Tu$ is the *true* relative fluctuation intensity of the random variable $\phi$. In the turbulence literature, $Tu$ is referred as the turbulence intensity, when $\phi$ is considered to be a velocity component.

### Comments

By inspection of Eqs. (C.4) and (C.9) the following observation is made: $\sqrt{\frac{2T_{int}}{T}}$ in Eq. (C.4) corresponds to $\frac{1}{\sqrt{N}}$ in Eq. (C.9). Rearranging, we obtain $\frac{T}{N} = 2T_{int}$. That is, in order to divide the full measurement time $T$ into $N$ statistically independent samples, these must have a time lag between them of - at least - $2T_{int}$. This means that one will not get a faster convergence for the estimator of the mean by measuring samples closer in time than two times the integral length scale of the turbulent flow. The more statistically independent samples are measured in a stationary random process, the better $\hat{\mu}_{\phi_i}$ estimates $\hat{\mu}_\phi$; hence $\mu_\phi$ or equally $\langle\phi\rangle$. A good example on how to use this technique in practice for a BFS can be found in Tropea *et al.* (2007).

In this context, the concept of "measuring long enough" can be quantitatively stated. A stationary random process is considered to be *long enough*, if $T \gg 2T_{int}$. As a rule of thumb, experience shows that for averaged quantities an integration time of at least $T \sim 100T_{int} \gg 2T_{int}$ is required, see George (2013) .

**Higher moments estimation**

For the sake of completeness, the procedure presented above can be generalized for higher moments of order $n$ (the variance would be $n = 2$) as follows

$$\varepsilon_{\langle \phi'^n \rangle} = \sqrt{\frac{2T_{int}}{T}} \frac{\langle \phi'^{2n} \rangle - \langle \phi'^n \rangle}{\langle \phi'^n \rangle} \tag{C.10}$$

or alternatively with the use of the more efficient *jackknife algorithm*, see Tropea *et al.* (2007).

Assuming a Gaussian distribution of velocity fluctuations, simplifications to Eq. (C.10) are possible (George (2013), p. 314 f). However, it must be recognized, that turbulent flows are *not* Gaussian processes. Only in very idealized cases they may be approximated by a Gaussian process in order to ease analysis. However, due to the absence of alternatives, turbulence is *assumed* to be a Gaussian process allowing to approximate calculations when designing an experiment.

# Appendix D

# Used design guidelines and future design recommendations

The objective of this section is to help research teams to reproduce the experiment.

## D.1 Used design guidelines for the flow conditioning section

The design of the components has been based on the following literature:

- General wind tunnel or water channel design rules: Mehta & Bradshaw (1979), Johansson (1992), Barlow *et al.* (1999), Bradshaw & Pankhurst (1964), Lindgren & Johansson (2002) and Cattafesta *et al.* (2010).
- perforated plates: Laws (1990).
- Wide angle diffusers with vanes: Feil (1964), Idelchik (2007), Blevins (1984), Cochran & Kline (1958), Kline (1969).
- Wide angle diffusers with screens: Mehta & Bradshaw (1979).
- 90° bends with vanes: Idelchik (2007), Mehta & Bradshaw (1979), Lindgren *et al.* (1998), Johl *et al.* (2007), Collar (1936).
- Settling chamber: Loehrke & Nagib (1972), Farell & Youssef (1996), Tan-Atichat *et al.* (1982), Laws & Livesey (1978), Groth & Johansson (1988), Hancock & Johnson (1997), Roach (1987) and Kurian & Fransson (2009).
- Contraction: Bell & Mehta (1989), Bell & Mehta (1988) and Mikhail (1979).

Figure D.1: Photographs of the test section inlet. On the left before welding, on the right after welding. The PEEK inner channel was not compromised during the welding activities per se. However, during the test section transport, one PEEK wall was damaged, as seen in hte right photograph.

## D.2 Recommendations for the design of future backward facing step test sections and its heated plate

**Test section**

The manufacturing of the double-wall backward facing step test section *has been not* an easy task. The original idea has been to separate the leak-tightness channel functionality from the pressure-containment channel functionality (Fig. (3.3)). The PEEK inner channel would be glued to guarantee leak-tightness, while the external stainless steel channel would support the channel pressure.

Although on paper this may work fine, in practice, it did not work:

i. To glue PEEK is not a straightforward task.

ii. The original two-wall concept would only work if both channels had mechanical contact *at every point all over* their extension, which for a $2\,(m)$ test section is almost impossible with regular workshop manufacturing techniques.

After four months of arduous work, failed attempts and try-and-error trials to get the test section leak-free, it has been decided to carefully weld the stainless steel channel without compromising the PEEK inner channel (right photograph in Fig. D.2).

Should a second test section be designed or should an external research team decide to manufacture a BFS test section for a *GaInSn* experiment, here are a few

design recommendations:

- Do not follow the original two-wall concept.
- Either manufacture a full PEEK channel with thick walls and mount the walls following a nut-logic (as in Fig. 3.3) and then either join the walls by welding the PEEK or - as I would do it - include a rubber seal for leak-tightness and secure the joint between the walls with several screws (every few centimeters).

**Heated plates**

The used heated plate concept is not optimal, as well as the apparent excessive use of thermocouples. Future designs should consider less thermocouples, which should be guided in a symmetric way (from two sides). Furthermore, at least two thermocouple stages along the heated plate thickness should be mounted for measuring the heat flux.

## D.3 Suppression of external electromagnetic interference in the probe signal

This problem has been solved, first, by selecting short and premium quality shielded and twisted cables for the probe. Second, by closing existing interruptions in the cable shielding network as shown in Fig. D.2. This may seem to create ground loops at first, but this is not the case. Instead, it completes a closed Faraday cage along the signal path. Third, by grounding all cables to and from the pump variable frequency drive on both sides and by lowering the pump variable frequency drive switching frequency to its minimum. And fourth, by choking common-mode interference currents by means of WÜRTH ELEKTRONIK clamp-on ferrites for low frequencies. The probe cables have been coiled around and then passed through ferrites. All cables connected to the variable frequency drive have been passed through ferrites. Further noise rejection strategies for a similar probe can be found in Cramer *et al.* (2006).

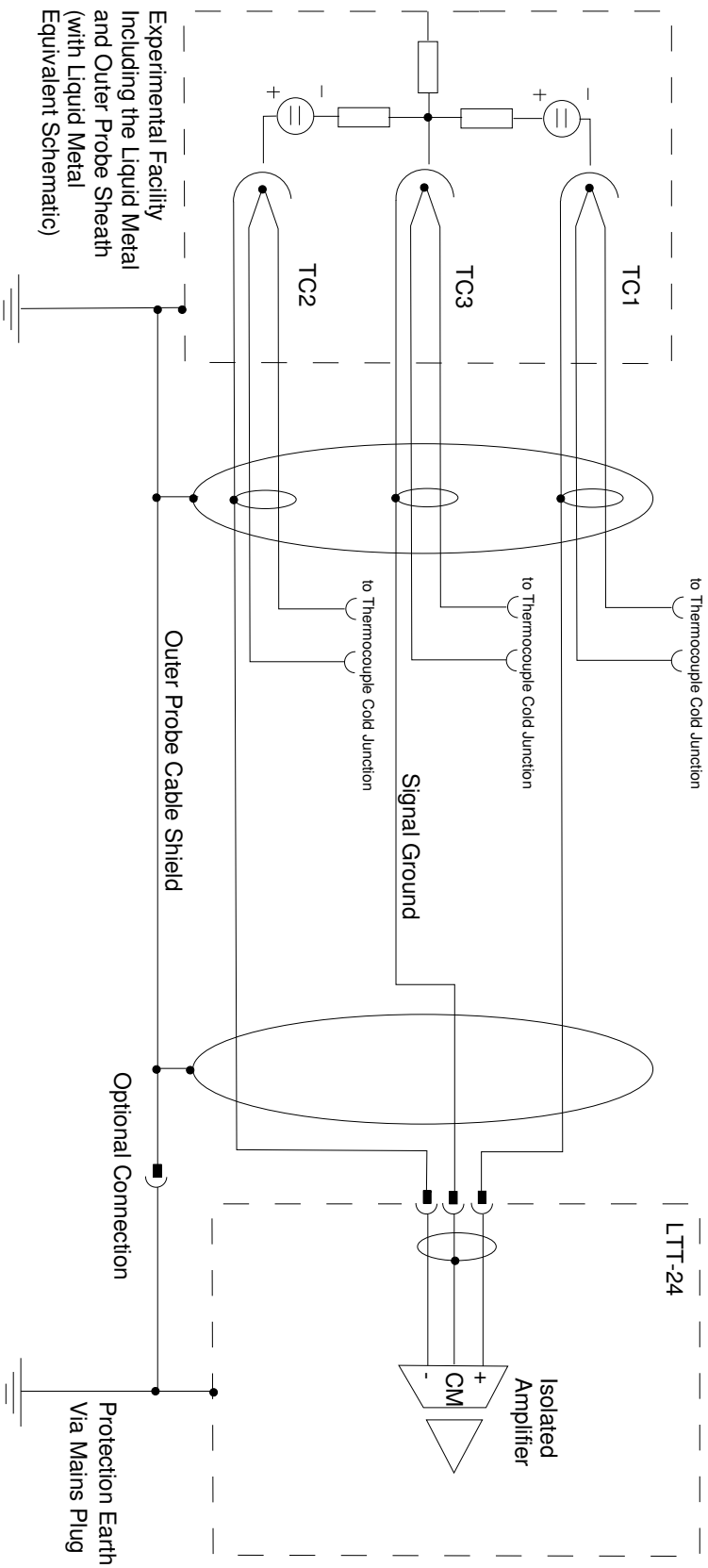


Figure D.2: Electric equivalent circuit diagram of the probe wiring and grounding.

# Appendix E

# Uncertainty analysis of the experimental results

The uncertainty analysis for this experiment has been already published in Schaub *et al.* (2022) and Schaub *et al.* (2022). Here, it is repeated for the sake of completeness.

## E.1 Probe calibration

The full uncertainty analysis for the probe sensitivity is presented next making use of the recommended procedure according to the Guide to the Expression of Uncertainty in Measurement by the Joint Committee for Guides in Metrology (JCGM), see JCGM (100:2008).

The uncertainty contributors for the probe sensitivity $K$ are:

i. The flow meter relative accuracy $u_{rel,\dot{V}}$.

ii. The accuracy of the area measurement of the inlet section measures $s_A$.

iii. The relative statistical uncertainty $u_{rel,V_{SS}}$ due to the limited integration time for the determination of $V_{SS}$.

iv. The uncertainty $u_r$ associated with the repeatability of the experiments.

It is assumed that the repeatability uncertainty contributor contains the uncertainty contribution of the measurement system thermal drift and the offset drift. Furthermore, all wetting issues due to the existing uncertainty of transferring the measured $K$ at position $P1$ to the other positions.

For the sake of simplicity, a type *B* evaluation for the standard uncertainties of each contributors is made. In a first instance, the definition for the measurement equation for $K$ for an error propagation analysis may seem trivial. But it is actually a tricky question. A worst case scenario is chosen based on the probe measurement equation (Eq. (3.4)) and assuming an isothermal flow. The estimated measurement equation reads,

$$\bar{K} = \frac{\Delta V_{SS}}{\Delta \dot{V}} A, \tag{E.1}$$

where $\bar{K}$ is the mean probe sensitivity calculating using a least square linear fit over the whole data cloud for each probe; $\Delta V_{SS}$ is the maximum estimated range for $V_{SS}$; $\Delta \dot{V}$ the maximum estimated range for the flow rate $\dot{V}$and $A$ denotes the inlet cross section area. These values for each probe are tabulated in Table E.1.

This worst case scenario handles the accuracy of the flow meter as a constant value over the whole range of the respective quantities. The flow meter accuracy is then multiplied by the range to obtain the respective standard uncertainty. This is a rough estimation for the uncertainty of these contributors, of course. However, as will be shown, these contributors are almost negligible compared to the repeatability standard uncertainty, mainly due to the wetting issues of the probe.

The combined standard uncertainty $u_{\bar{K}}$ for $\bar{K}$ reads to

$$u_{\bar{K}} = \sqrt{\left(\frac{\partial \bar{K}}{\partial \Delta \dot{V}} u_{\Delta \dot{V}}\right)^2 + \left(\frac{\partial \bar{K}}{\partial A} u_A\right)^2 + \left(\frac{\partial \bar{K}}{\partial \Delta V_{SS}} u_{\Delta V_{SS}}\right)^2 + u_r^2}, \tag{E.2}$$

where $u_i$ are the standard uncertainties of each contributor which are multiplied by their respective sensitivity $\partial \bar{K}/\partial i$. All components are assumed uncorrelated.

For the estimation of the repeatability standard uncertainty $u_r$ a type *B* evaluation has been made as well. The measured sensitivities are shown in Table E.1, where $K_{min}$ is the smallest measured sensitivity for that probe, $K_{max}$ the largest and $\sigma$ is the standard uncertainty for $K$, with $2u_r = (K_{max} - K_{min})/\sqrt{3}$ under the assumption of a rectangular distribution of $K$ between $K_{max}$ and $K_{min}$.

As can be observed in Table E.1 and as expected, the uncertainty due to repeatability between runs is the main uncertainty contributor. The repeatability issues are most likely to be related with wetting issues of the liquid metal. It needs to be noted that the repeatability uncertainty contributor has been calculated using a conservative approach.

The individual standard uncertainties, the combined and the extended standard

Table E.1: Reference values to be substituted into the error propagation analysis for the different uncertainty contributors

| | Unit | Probe 1 | Probe 2 | Probe 3 | Probe 4 | Probe 5 | Probe 6 |
|---|---|---|---|---|---|---|---|
| $\bar{K}$ | $\mu V/m/s$ | 52.41 | 50.85 | 41.95 | 23.18 | 43.97 | 54.82 |
| $\Delta V$ | $m^3/s$ | | | 0.0009 | | | |
| $A$ | $m^2$ | | | $0.08 \cdot 0.040 = 0.0032$ | | | |
| $\Delta V_{SS}$ | $\mu V$ | 14.74 | 14.30 | 11.80 | 6.52 | 12.37 | 15.42 |

uncertainty are presented in Table E.1.

## E.2 Velocity profiles

The measured signal velocity is given by

$$V_{SS} = Ku_{vol} + S_e \Delta T + V_0, \tag{E.3}$$

where all variables have already been introduced in Eq. (3.4).

Rearranging and averaging in time, one obtains the measurement equation for the mean velocity,

$$f = \bar{u} = \frac{\bar{V}_{SS} - \bar{V}_0 - S_e \Delta T}{K}. \tag{E.4}$$

The combined standard uncertainty $u_{\bar{u}}$ for $\bar{u}$ is given by

$$u_{\bar{K}} = \sqrt{\left(\frac{\partial f}{\partial \bar{V}_{SS}} s_{\bar{V}_{SS}}\right)^2 + \left(\frac{\partial f}{\partial \bar{V}_0} s_{\bar{V}_0}\right)^2 + \left(\frac{\partial f}{\partial S_e} s_{S_e}\right)^2 + \left(\frac{\partial f}{\partial \Delta T} s_{\Delta T}\right)^2 + \left(\frac{\partial f}{\partial K} s_K\right)^2 + s_r^2}, \tag{E.5}$$

where $\partial f/\partial x_i$ are the sensitivities of each uncertainty contributor, $u_i$ the standard uncertainties of each uncertainty contributor, where $u_R$ represents the standard uncertainty of the repeatability study.

**Determination of $u_{\bar{V}_{SS}}$**

$u_{\bar{V}_{SS}}$ is the statistical uncertainty due to the limiited sampling time of $\bar{V}_{SS}$. Tropea *et al.* (2007) describe the methodology on how to calculate this uncertainty. Since $\bar{V}_{SS}$ is the measured signal proportional to the volume averaged velocity around the

Table E.2: Standard uncertainties for the variables for each PMP. All distributions are assumed rectangular. All calculation steps have been made with all digits – the results are shown with only two significant digits

| | | Unit | Probe 1 | Probe 2 | Probe 3 | Probe 4 | Probe 5 | Probe 6 |
|---|---|---|---|---|---|---|---|---|
| $u_{\Delta\dot{V}}$ | Accuracy | % | 0.42 | | | | | |
| | | $m^3/s$ | $3.78 \cdot 10^{-6}$ | | | | | |
| | Distribution factor | – | $1/\sqrt{3}$ | | | | | |
| | $u_{\Delta\dot{V}}$ | $m^3/s$ | 1.09 | | | | | |
| $u_A$ | Tolerance | *mm* | 0.1 (for one dimension) | | | | | |
| | Distribution factor | – | $1/\sqrt{3}$ | | | | | |
| | $u_{1D}$ (for one dimension) | *m* | $57.74 \cdot 10^{-6}$ | | | | | |
| | $u_A$ | $m^2$ | $5.16 \cdot 10^{-6}$ | | | | | |
| $u_{\Delta V_{SS}}$ | Precision | % | 0.34 | | | | | |
| | | *nV* | 47.17 | 45.77 | 37.75 | 20.86 | 39.57 | 49.33 |
| | Distribution factor | – | $1/\sqrt{3}$ | | | | | |
| | $u_{\Delta V_{SS}}$ | *nV* | 13.62 | 13.21 | 10.90 | 6.21 | 11.42 | 14.24 |

Table E.3: Type B standard uncertainty estimation for the repeatability of the calibration for the PMP.

| | $K_{min}\,\mu V/m/s$ | $K_{max}\,\mu V/m/s$ | $u_r\,\mu V/m/s$ |
|---|---|---|---|
| $P1$ - All Runs | 50.82 | 53.79 | 0.85 |
| $P2$ - All Runs | 49.87 | 51.86 | 0.57 |
| $P3$ - All Runs | 36.50 | 47.63 | 3.21 |
| $P3$ - $3^{rd}$ Run only | 46.09 | 47.63 | 0.44 |
| $P4$ - All Runs | 17.00 | 31.71 | 4.25 |
| $P5$ - All Runs | 40.83 | 45.84 | 1.45 |
| $P5$ - $3^{rd}$ Run only | 45.84 | 45.72 | 0.04 |
| $P6$ - All Runs | 51.09 | 58.00 | 1.99 |
| $P6$ - $3^{rd}$ Run only | 57.24 | 58.00 | 0.22 |

Table E.4: Standard uncertainties $u_i$, combined uncertainty $u_{\bar{K}}$ and extended uncertainty $2u_{\bar{K}}$ (95.4% confidence interval).

| | Unit | Probe 1 | Probe 2 | Probe 3 | Probe 4 | Probe 5 | Probe 6 |
|---|---|---|---|---|---|---|---|
| $u_{\Delta V}$ | $\mu V/m/s$ | 0.064 | 0.062 | 0.051 | 0.028 | 0.053 | 0.066 |
| $u_A$ | $\mu V/m/s$ | 0.085 | 0.082 | 0.068 | 0.037 | 0.071 | 0.088 |
| $u_{\Delta V_{SS}}$ | $\mu V/m/s$ | 0.051 | 0.050 | 0.041 | 0.023 | 0.043 | 0.054 |
| $u_r = s_r$ | $\mu V/m/s$ | 0.85 | 0.57 | 3.21 | 4.25 | 1.45 | 1.99 |
| $u_{\bar{K}}$ | $\mu V/m/s$ | 0.86 | 0.58 | 3.21 | 4.25 | 1.45 | 1.99 |
| $2u_{\bar{K}}$ | $\mu V/m/s$ | 1.72 | 1.16 | 6.42 | 8.50 | 2.91 | 3.99 |

probe tip, the integral time scale $t_{int}$ and the turbulence intensity $Tu$ of the flow at each point should be measured. The calculation of $Tu$ from the measured signal is straightforward. However, the measurement of $t_{int}$ on each measured point is not practically possible. In the absence of other practical alternative, $t_{int}$ has been calculated from an estimation for the integral length scale $l_{int}$ assuming the Taylor hypothesis of frozen turbulence taking the local measured velocity as the characteristic velocity. For probes $P1$ and $P2$ an approximate value for the integral length scale is calculated. Bailly & Comte-Bellot (2015) indicate that for a fully developed turbulent channel flow between two plates the integral length scale $l_{int}$ can be estimated as 0.6 times the half channel width. For the rest of the probes, $l_{int}$ has been estimated taking the step height. The statistical uncertainty $\varepsilon$ of each point is then calculated as

$$\varepsilon = \sqrt{\frac{2t_{int}}{t_s}} Tu, \tag{E.6}$$

where the sampling time $t_s$ for each point has been $t_s = 105\ (s)$. This uncertainty contributor is included into Eq. (E.5) as a type $A$ evaluation.

**Determination of $u_{\bar{V}_0}$**

Before every measurement campaign, the LTT24 system (and all other instrumentation) are warmed up for at least $12h$. Before every measurement, the LTT24 system is offset corrected. Nevertheless, the zero level of each probe is not totally stable over time, particularly considering that each measurement campaign (one parameter set) lasted approximately $10h$. A representative worst-case-scenario value for the fluctuation of all probes during the whole measurement campaign is estimated as $u_{V_0} = 60nV$. This uncertainty contributor is included into Eq. (E.5) as a type B evaluation assuming a rectangular distribution.

**Determination of $u_{S_e}$**

The effective Seebeck coefficient is determined from the Seebeck coefficients of stainless steel (thermocouple sheaths) and *GaInSn*. In the absence of any other alternative, $S_{SS}$ is assumed as exact. Its value is obtained from Bentley (1998). The value for $S_{GaInSn}$ and $s_{S_{GaInSn}}$ are taken from Plevachuk *et al.* (2014). The value for $s_{S_e}$ is then estimated as $s_{S_e} = s_{S_{GaInSn}}$.

**Determination of $u_{\Delta T}$**

$s_{\Delta T}$ is determined in the same manner as $s_{\bar{V}_{SS}}$. The big question to be anshave beend is what the correct integral time scale for this quantity is. The key is to recognize that it is not each temperature $T_1$ and $T_2$ that is important here, but their difference. And a temperature difference between these two points is given only by flow structures smaller than the probe tip. Hence, the integral length scale the worst-case value of $l_{int} = d_{tip}$ is taken.

**Determination of $u_K$**

This calculation has been shown in detail in the uncertainty analysis for the calibration of the probe, see Table E.1.

**Determination of $u_r$**

As mentioned before, the measurement of one parameter set, i.e. the measurement of all velocity profiles plus the Nusselt number distribution along the heated plate, took about $10h$. According to the GUM, a repeatability study should have at least 30 samples. This would take a minimum of 6 weeks to accomplish, which due to time constraints of the project, has been not possible. Hence, only 3 samples have been measured. This uncertainty contributor has been included into Eq. (E.1) as a type *A* evaluation by taking into consideration the effective number of degrees of freedom.

**Calculation of the extended uncertainty for $u_{\bar{u}}$**

From Eq. (E.1) one can calculate the extended uncertainty $u_{e,\bar{u}}$ for $u_{\bar{u}}$ . Usually, one would take the coverage factor $k = 2$, i.e. $u_{e,\bar{u}} = 2u_{\bar{u}}$ for a 95.45% confidence interval. However, due to the limited samples for $s_r$ this cannot be made. Instead, the $t$-Student distribution must be used to obtain the coverage factor $k$. The effective number of degrees of freedom is calculated for every point with the WELCH-SATTERTHWAITE formula. For almost every measurement point, the calculated coverage factor is higher than 2.

**Main uncertainty contributors**

The influence of each uncertainty contributor is the same for all measurement points and correspond to $s_{\bar{V}_{SS}}$, $s_{\bar{V}_0}$, $s_K$ and $s_r$. Depending on the local conditions, the in-

fluence of each contributor varies. The uncertainty contributors for $\bar{V}_{SS}$ and the repeatability can be improved by just taking longer measurements sampling times per point and by performing an exhaustive repeatability study. It must be noted that if longer measurements per point are desired, the spatial resolution of the profiles must be decreased to keep the daily measurement campaign extension within the lab opening hours. The contributor for $\bar{V}_0$ cannot be avoided. This is intrinsic to the measurement system and this author is not aware of any commercially available measurement system with better performance than the LTT24. The contributor for $K$ can be improved by calibrating the probes in-situ. This is however limited by the geometry of the test section.

## E.3 Local Nusselt number along the heated plates

The measurement equation reads

$$f = Nu = \frac{\alpha l_c}{\lambda_{ref}} = \frac{\dot{q} l_c}{\lambda_{ref} \Delta T} \tag{E.7}$$

where $\Delta T = T_w - T_{bulk}$.

The standard uncertainty $u_{Nu}$ for $Nu$ is given by

$$u_{Nu} = \sqrt{\left(\frac{\partial f}{\partial \dot{q}} u_{\dot{q}}\right)^2 + \left(\frac{\partial f}{\partial l_c} u_{l_c}\right)^2 + \left(\frac{\partial f}{\partial \lambda_{ref}} u_{\lambda_{ref}}\right)^2 + \left(\frac{\partial f}{\partial \Delta T} u_{\Delta T}\right)^2} \tag{E.8}$$

where $\partial f / \partial x_i$ are the sensitivities of each uncertainty contributor and $u_i$ the standard uncertainties of each uncertainty contributor.

In this case, no repeatability study has been made due to time constraints. Nevertheless, looking at the results for Nu, one can infer that the repeatability of the data is good.

#### Determination of $s_{\dot{q}}$

The values for $\dot{q}$ are calculated as $\dot{q} = \dot{Q}/A$, where $\dot{Q}$ is the power input and $A$ is the heated plate surface area. $\dot{Q}$ is calculated reading the power source display values for the DC-voltage $V_{DC}$ and the DC-current $I_{DC}$ as $\dot{Q} = V_{DC} I_{DC}$. After the measurement campaign, the display values have been offset corrected by comparing the display values to actual measured values with a calibrated multimeter.

The standard uncertainty $s_{\dot{q}}$ is taken from the power source data sheet and included into Eq. (E.8) as a type *B* evaluation.

**Determination of $s_{l_c}$**

The uncertainty of the characteristic length, i.e. the step height, is the manufacturing tolerance of $0.1\,(mm)$ and included into Eq. (E.8) as a type *B* evaluation.

**Determination of $s_{\lambda_{ref}}$**

The value for $\lambda_{ref}$ as well that of $s_{\lambda_{ref}}$ have been taken from Plevachuk *et al.* (2014) and are included as a type *B* evaluation.

**Determination of $s_{\Delta T}$**

This contributor has been determined in the same way as $s_{\bar{V}_{SS}}$ for the velocity profiles. The integral time scale has been calculated from an estimated integral length scale equal to the heated plate length, i.e.$l_{int} = 15h$. This contributor has been included into Eq. (E.8) as a type *A* evaluation.

**Calculation of the extended uncertainty for $u_{Nu}$**

In this case, since enough samples could be measured for each contributor obtained from a type *A* evaluation, a coverage factor $k = 2$ has been used for a 95.45% confidence interval.

# Appendix F

# Impact of the findings of this study for technical and future research applications

- Turbine flow meters are not recommended for liquids with a high surface tension, since the turbine rotor gets not sufficiently lubricated by the fluid to work properly.

- For heat transfer applications, a proper wetting between the surface to be cooled and the fluid are mandatory. The (accidentally) re-discovered electro-wetting procedure for wetting a liquid metal to a metallic surface may be applied to check the wetting quality between a cooling liquid metal and the heat source. The same principle applies to thermal-to-electric converters. For the AMTEC-cell (de los Rios Ramos *et al.* (2017)), very high sodium temperatures are required to guarantee an optimum wetting between the liquid sodium and the beta-BASE ceramic. The ceramic-to-sodium wetting may be optimized by applying a voltage between both, i.e. by electro-wetting the ceramic.

- The electromagnetic interference reduction strategy developed for the permanent magnet probe measurement chain can be of course applied to any low-noise measurement task. The combined use of clamp-on ferrites and Faraday cages proved to particular effective regarding this issue. This means that the use of digital variable frequency drives in an experiment does not necessarily mean that low-noise measurements are not possible.

- When choosing an electrical insulator for the probe tip material, complex temperature corrections and calibrations are not necessary.

- The theoretical estimations for the probe sensitivity showed good agreement with the measurements.

- The measured probe sensitivity showed – as expected – a linear behavior for the given range.

- Due to the high surface tension of *GaInSn*, wetting issues of the probe tip must be taken into consideration during the process of the instrumentation development, their use and the uncertainty analysis.

- Mechanical wetting, i.e. rubbing *GaInSn* to the probe tip to guarantee hydrodynamic wetting, does not guarantee by itself a good performance of the probe. A good electric connection between the liquid metal and the probe electrodes must be guaranteed for the probes to work properly, as well.

- A hydrodynamic wetting condition does not imply immediately a sufficiently good electric connection between the liquid metal and the probe electrodes. At the same time, a good electrical connection between the probe electrodes does not imply directly a good hydrodynamic wetting.

- The experimental facility pumping system should be designed in such a way, that it does not emit too much electromagnetic disturbances. If possible, digital variable frequency drives should be avoided. However, with a careful electromagnetic interference strategy, these influences can be suppressed up to a minimum.

- In situ calibrations for the probes are preferred. This has been not possible for the present test section, due to its geometrical characteristics.

- The calibration of the probe in an external calibration facility should be associated with similar uncertainty as for the proposed calibration strategy.

- Assuming a proper wetting procedure of the probe after a few hours of running time of the facility, the probe sensitivity reaches a nearly constant value. As expected, the main uncertainty contributor for the measured probe sensitivities is related to the wetting issues.

– As shown in the analysis of the experimental data, only by simple scale analysis, accurate theoretical predictions are possible for very complex flow phenomena - at least in an order of magnitude sense. Quoting Prof. Adrian Bejan in Bejan (2013): "*[...] scale analysis is recommended as the premier method for obtaining the most information per unit of intellectual effort*".

– Conjugate heat transfer calculations are mandatory for the accurate prediction of heat transfer phenomena, particularly when the heat source Biot number $Bi$ is in the order of unity.

# *APPENDIX F. IMPACT OF THE FINDINGS OF THIS STUDY FOR TECHNICAL AND FUTURE RESEARCH APPLICATIONS*

# Appendix G

# Miscellaneous

The next lines contain a few comments and literature tips and helpful quotation on some important concepts in physics and engineering:

**On pressure...**

Recalling Eq. (2.4)

$$\rho \frac{Du_i}{Dt} = \rho f_i - \frac{\partial p_{mech}}{\partial x_i} + \frac{\partial}{\partial x_j} \mu \left( \frac{\partial u_i}{\partial x_j} + \frac{\partial u_j}{\partial x_i} \right), \tag{G.1}$$

a comment on the concept of *pressure* must be made.

The mechanical pressure $p_{mech}$ as defined above is different in concept (but similar in value) from the thermodynamic pressure $p_{thermo}$ as defined by the equation of state. A fluid in motion is - strictly speaking - not in thermodynamic equilibrium. Only in the case of a fluid at rest, i.e. when the fluid particles are in thermodynamic equilibrium, one *may* have $p_{mech} = p_{thermo} = p_{static}$, where $p_{static}$ is the local static pressure. For moving fluids, due to the effects of viscosity, the normal components of the stress tensor cannot be regarded as isotropic. Since this complicates analysis, it is usual to *define* a isotropic pressure for moving fluids, the mechanical pressure $p_{mech}$, as done above, i.e. thinking of the stress tensor $\sigma_{ji}$ as a sum of an isotropic and anisotropic part. For the kind of flows to be analyzed here - where velocity, pressure and temperature gradients are relatively small - it can be assumed that $p_{mech} \approx p_{thermo}$. For more details and a deeper discussion on this topic, see Batchelor (1967).

**One comment about turbulence and the equations of motion**

It is known that turbulence *is contained* in the Navier-Stokes equations in the convective term. After some vector algebra, it is possible to decompose the convective term into two components that show in a more intuitive way the non-linear and rotational character of this term, as shown in Feynman *et al.* (2010).

The starting point are the equations of motion for a fluid expressed in vector notation and neglecting the effects of viscosity and body forces (which for these means are irrelevant)

$$\frac{\partial \vec{u}}{\partial t} + (\vec{u} \cdot \nabla)\,\vec{u} = -\frac{\nabla p}{\rho}, \tag{G.2}$$

where $\vec{u}$ is the velocity vector, $\nabla$ is the gradient operator, $p$ is the mechanical pressure and $\rho$ is the fluid density.

Using the definition of vorticity $\Omega$ as $\Omega = \nabla \times \vec{u}$ and the vector algebra identity for the convective term in Eq. (G.2) one obtains

$$(\vec{u} \cdot \nabla)\,\vec{u} = (\nabla \times \vec{u}) \times \vec{u} + \frac{1}{2}\nabla(\vec{u} \cdot \vec{u}), \tag{G.3}$$

and after some algebra the following equation

$$\frac{\partial \vec{u}}{\partial t} + \Omega \times \vec{u} + \frac{1}{2}\nabla(\vec{u} \cdot \vec{u}) = -\frac{\nabla p}{\rho} \tag{G.4}$$

from which it becomes more intuitive - although it does not demonstrate - what physical phenomena is contained in the convective term.

**On natural convection dimensionless numbers...**

As pointed out by Bejan (2013), the *Gr*, *Ra* and *Bo* numbers, as such, have no physical meaning at all. However, they do have a geometrical meaning when pohave beend to the one-forth. For $Pr \ll 1$, $Bo^{1/4}$gives - in the order of magnitude sense - a hint of the ratio between the heated vertical wall and the thermal boundary layer thickness, while $Gr^{1/4}$gives a hint of the ratio between the heated vertical wall height and the wall shear layer thickness. This is also shown in Kays *et al.* (2007) and Schlichting & Gersten (2017).

However, other authors (Jischa (1982) and Incropera *et al.* (2017)) give to *Gr* a physical meaning based in the concept of force ratios (buoyancy forces over viscous forces). This may be considered as rather artificial since the Grashof number

does not appear in the equations of motion as to interpret it in this manner. It is the quotient between the Grashof number and the square of the Reynolds number that actually plays a role regarding the ratio of forces. Furthermore, Cebeci & Bradshaw (1984) obtain with dimensional analysis the characteristic velocity for a natural convection flow and then *use* this velocity to *form* a conceptually equivalent Reynolds number but for natural convection cases. The result of this procedure is the Grashof number. This is also supported by Schlichting & Gersten (2017). So I think that the Grashof number is sometimes associated as a force ratio just because the concept of inertia-to-viscous-force-ratio (characteristic of the Reynolds number) has been transferred to the natural convection case.

**On magnetic fields...**

Magnetic fields don't physically *exist* per se. The magnetic field is actually as pseudo-vector (Davidson (2017)) , i.e. its *existence* depends on the inertial reference of frame, similarly as does the centrifugal force. A magnetic field is physically best explained as a relativistic corollary to Coulombs law. See, Purcell & Morin (2013), Feynman *et al.* (2010).

**On Faraday's law**

Faraday's law is often associated with time-varying magnetic fields. This must not be always the case. As written by Davidson (2017): "*Faraday's law tells us about the EMF* (electromotive force) *which is generated in a* (electrical) *conductor as a result of (i) a time-dependent magnetic field or (ii) the motion of a conductor within a magnetic field*". This duality is explained by Feynman (Feynman *et al.* (2010)): *"[...] that the EMF in a circuit is equal to the rate of change of the magnetic flux through the circuit applies whether the flux changes because the field changes or because the circuit moves (or both). The two possibilities - "circuit moves" or "field changes" - are not distinguished in the statement of the rule*".

**On Lorentz forces**

Lorentz forces generally refer to the force experienced by a charged particle which is moving or being displaced within an externally imposed magnetic field. It doesn't matter what the cause of the motion is, i.e. whether the motion of the particle is due to an electric field (a voltage - induced or imposed) or due to the (mechanical) displacement of the conductor (e.g. a copper wire).

**On thermo-electricity - Seebeck, Peltier, Thompson and Johnson effects**

There are basically four thermo-electric effects that may affect the measurement task with PMP, namely, the Seebeck-, the Peltier-, the Thompson- and the Johnson-effects. These effects are to be distinguished from each other and are best explained conceptually in Fenton (1980) and more in detail in Kasap (2017).

**Helpful quotations**

> An experimentalist performs experiments to sort theories [...] His objective is to find which equations and which boundary and initial conditions his solution corresponds to [...] Contrary to popular belief, an experimentalist must understand and be conversant with theory [...] We must first and foremost be *fluid mechanicists*, and in doing so, we will find ourselves becoming *experimentalists*.
>
> WILLIAM K. GEORGE, GEORGE (1990)
>
> The art of engineering lies not in solving the equations but in picking the "right" equations and installing the "right" values so the result of our mathematics answers the question we had in mind at the beginning.
>
> ROBERT J. MOFFAT, MOFFAT (1988)
>
> [...] measurement is primarily a treatment of errors: obtaining the reading is easy.
>
> ROBIN BENTLEY, BENTLEY (1998)